Structure and dynamics of two-dimensional colloidal hard spheres

Alice L. Thorneywork

Christ Church
University of Oxford

Supervisor: Dr Roel P. A. Dullens

A thesis submitted for the degree of
Doctor of Philosophy

Hilary Term 2015

Abstract

The structural and dynamic behaviour of quasi-two-dimensional monodisperse and bidisperse colloidal hard spheres are studied by optical microscopy. Firstly, a full characterisation of the equilibrium structure is presented through a consideration of structural correlation functions and number fluctuations. Comparison to fundamental measure theory and Monte Carlo simulations confirms both the behaviour of the system as a model for hard disks and the equation of state. The differing structural behaviour of binary systems at different size ratios is also discussed in relation to the nonadditivity. Next, the short- and long-time self-diffusion of particles is considered. Results for the long-time diffusion coefficient are again compared to Monte Carlo simulations, which demonstrates that at long times the dynamic behaviour is effectively not affected by hydrodynamic interactions. Additionally, simple theoretical expressions for the area fraction dependence of the short- and long-time diffusion coefficients are discussed. The self-dynamic properties of particles are probed further using the self-intermediate scattering function and the self-van Hove correlation function. In particular, the extent to which these quantities may be described by the Gaussian approximation is considered in relation to the relevant hydrodynamic limits for colloidal systems. A scaling relation to describe the crossover between these limits at short and long times is also developed. The consideration of dynamic behaviour is then extended to collective phenomena and, in particular, to the process of interdiffusion. Here, the thermodynamic and kinetic drives for this process are explored for binary systems at two different size ratios. The differing interdiffusive effects seen in the two systems are considered in light of the predictions of the Darken equation. Finally, the melting of quasi-two-dimensional colloidal hard spheres is studied by considering a monolayer of particles in sedimentation-diffusion equilibrium. Density profiles and the equation of state are used to characterise the system. These quantities display a discontinuity, indicating a coexistence gap and hence an interface. This interface is located and analysed using capillary wave theory, from which both the size of the coexistence gap and the anisotropic stiffness of the interface are determined.

Declaration

This thesis is submitted for the degree of Doctor of Philosophy in Physical and Theoretical Chemistry at the University of Oxford. No part of this thesis has been accepted or is currently being submitted for any degree, diploma, certificate or other qualification in this University or elsewhere. This thesis is wholly my own work, except where indicated.

Contents

Chapter 1

Introduction

No physical object satisfies the mathematical definition of 'two-dimensional', yet phenomena associated with two dimensions are frequently encountered and of widespread significance. These phenomena arise in a number of scenarios. Firstly, three-dimensional objects possess and interact via two-dimensional surfaces, often with characteristics that are more complex than expected by simply projecting their bulk properties to lower dimensionality. Indeed, two-dimensional (2D) and three-dimensional (3D) studies of materials are complimentary, and both perspectives are required to fully characterise a material. Interfaces are also effectively two-dimensional and understanding their properties is relevant to an enormous variety of systems, particularly in biology, where membranes define the boundaries of cells and govern many of their processes [1]. Furthermore, following the discovery of graphene and its remarkable properties [2] there is a growing interest in materials that are almost 2D, existing as monolayers with a thickness of one atom [3].

Many other systems exist which can be described as '2D' with respect to certain, but not all, of their properties. Adsorbed surface layers are structurally 2D and substantially alter the chemical and physical properties of materials, including their catalytic ability and crystal growth [4, 5]. Importantly, however, while these systems can be used to study 2D phenomena, they are highly dependent upon the nature of the surface to which they are adsorbed. A more independent 2D system can be formed from a single layer of a smectic phase of a liquid crystal, which can be used to study complex structural and dynamic phenomena [6, 7], in some cases with relevance to biological systems [8,9]. A range of microfluidic devices also act as 2D systems

and these have a variety of important applications, for example in medicine [10], as well as a role in the study of more fundamental phenomena, such as those related to microscopic fluid dynamics [11, 12].

In geometrical terms, visualising a two-dimensional system is simpler than visualising a 3D system, however, this simplicity does not necessarily extend to the physics that governs its behaviour. In fact, the reduced dimensionality of 2D systems can lead to phenomena which are not seen in 3D, such as the absence of long-range positional order in 2D crystals [13] or the non-existence of the diffusion coefficient [14]. One of the most widely studied examples of the effect of dimensionality is that of the melting of 2D crystals, which proceeds via a hexatic phase [15–17] unlike in 3D. Striking differences in behaviour can already be observed for relatively modest confinement, for example by disrupting the bulk behaviour with the addition of a single wall. This has been seen in phenomena related to heterogeneous nucleation [18, 19], layering phenomena [20] and capillary effects [21–23]. Determining whether these phenomena seen in theory and simulation exist in experimentally realisable 2D systems is thus of enormous interest. It is therefore highly desirable to develop effective experimental model systems in which these phenomena can be directly probed.

1.1 Colloidal model systems

One possible source of these model systems are colloidal suspensions. These are composed of particles with a length in at least one dimension between 10 nm and 10 μm, dispersed in a continuous phase. The limits on lengthscale are approximate, and arise from the requirement that the colloidal particles are large relative to the particles of the dispersing medium, but small enough to exhibit Brownian motion – the irregular movement of solute particles resulting from random collisions with molecules of the solvent. The suitability of colloids as models for atomic and molecular systems follows directly from a number of their intrinsic properties. Firstly, the similarity of Brownian motion to the thermal motion in atomic and molecular systems leads to analogous phase behaviour [24, 25]. Secondly, the size of colloidal particles allows for their study over experimentally convenient timescales (s) and lengthscales (μm) and as such, in real space and real time. Furthermore, colloidal system are also highly tuneable. Colloidal particles with a wide array of shapes [26–30] can be synthesized from a diverse range of materials [31–34] and

the surface chemistry modified, or solvent varied, to create systems that exhibit a variety of interparticle interactions [35–39]. They may also be directly manipulated, by means of optical tweezers [40, 41], magnetic fields [42, 43], or the imposition of shear [44, 45]. This inherent versatility means that many physical phenomena can be studied using colloids, including self-assembly [46], active matter [47, 48] and phase transitions [24, 49–51]. Here, the ability to study the systems directly by optical microscopy allows for detailed structural and dynamic information to be obtained, and hence the mechanisms of these phenomena to be probed at a single particle level.

Colloidal model systems have been widely used to consider 2D phenomena, with a range of methods of confinement including thin cells [52–57], optical tweezers [58], or simply gravity [59–67] employed to realise a colloidal monolayer. Here, however, the colloidal systems themselves are more accurately described as *quasi*-two-dimensional. This distinction is due to the fact that while the motion of the colloidal particles is confined to a single plane, the momentum transport through the solvent can evolve in three spatial directions. This has a substantial effect on the particle dynamics due to the complex, solvent-mediated, hydrodynamic interactions between particles and this subtlety can in fact lead to surprising differences in the dynamic behaviour of systems all described as quasi-2D, but confined by different methods [54, 57, 62, 65, 68, 69].

1.2 Hard core systems

While colloids are used to study increasingly complex phenomena, they have long been recognised as one of the best experimental realisations of the simplest many body interacting system, that of particles interacting via a hard core potential [24]. For hard spheres with diameter σ and at separation r, the pair potential, $v(r)$, has the form

$$v(r) = \begin{cases} \infty & \text{for } r < \sigma \\ 0 & \text{for } r \geq \sigma, \end{cases} \tag{1.1}$$

which physically implies that particles cannot overlap or interpenetrate. This pair potential is of relevance to many systems, due to the dominance of the interaction potential by a strong repulsion at short distances, which for molecular and atomic systems arises from the overlap of electron shells.

The absence of an attractive component of the interaction potential means that the behaviour of hard core systems is dominated by entropy, with their phase behaviour governed only by the packing fraction. Many interesting phenomena are associated with the latter, particularly with respect to their entropy-driven phase transitions [70]. Specific details associated with the transitions depend upon the shape of the particles involved, with some examples the isotropic-nematic transition in hard rods discovered by Onsager [71], and the fluid-solid transition for hard spheres first determined by simulation [72–74]. While there is an obvious appeal in studying such simple systems from the point of view of fundamental properties, understanding the behaviour of hard core systems is also important due to their use as reference systems, where additional features of the interaction potential may be added as a perturbation [75].

While the behaviour of hard spheres in 3D and hard disks in 2D has been widely studied by theory and simulation, (see for example [76–82]), there are still many outstanding questions related to these systems. These include determining the relationship between the structural and dynamic properties of dense fluids [66,80,83,84], understanding the underlying mechanisms that lead to the glass transition [77,85–87] and verifying a scenario by which the melting of crystals in 2D occurs [88,89]. The inherent simplicity of their interaction potential makes hard core systems a valuable tool to achieve a fundamental understanding of these complex many body phenomena. For liquids in particular, it is well known that the hard core repulsion governs the observed structure [90–93], and a hard core system thus provides valuable insight without additional complicating factors. This is an especially relevant result, as it is the dense but disordered nature of liquids that makes their theoretical description so challenging. Early experimental work considering the structure of liquids in 3D utilised macroscopic systems of ball bearings to consider hard sphere packing arrangements [94], which has more recently been extended to studying vibrated granular matter [95–97]. For thermalised hard spheres, however, colloidal systems are the most widely used model system [98], though the properties of two-dimensional hard spheres have been much less well explored experimentally than their 3D equivalents. Phenomena specific to experimental 2D hard disk fluids are therefore still a matter of much debate.

1.3 Scope of the thesis

In this thesis, the structural and dynamic behaviour of quasi-two-dimensional colloidal hard spheres is investigated. The colloidal particles are confined to a monolayer by gravity and their behaviour is studied by optical microscopy over a wide range of compositions and area fractions. From this, fundamental relations from liquid state theory may be tested and the phase behaviour of the system probed. In the following chapters, the colloidal model system is first characterised with respect to structural and dynamic properties in order to determine the extent to which the particles behave as model hard disks. This system is then used to study more complex phenomena including the link between structure and self-diffusion, the behaviour of the intermediate scattering function as measured by microscopy, interdiffusion in binary fluids and melting in two dimensions.

Firstly, in Chapter 2 the statistical mechanical background used to describe properties of colloidal fluids and the experimental methods used to study them are presented. The grand canonical ensemble and number fluctuations are described, and the structural and dynamic correlation functions used to characterise the behaviour of the system are discussed. Then, the experimental details of the colloidal model system, optical microscopy set-up and image processing are presented.

In Chapter 3, a full characterisation of the equilibrium structure of the monodisperse and bidisperse colloidal fluids is presented, using the radial distribution function, static structure factor and an analysis of number fluctuations. Results are compared to those from fundamental measure theory and a Monte Carlo simulation of hard disks in order to test the extent to which the experimental system behaves as a hard disk fluid. Also the equation of state for the monodisperse system is confirmed. The contrasting structure of binary systems at different size ratios is considered in terms of the nonadditivity.

A characterisation of the dynamic behaviour of the monodisperse and binary quasi-two-dimensional colloidal systems is performed in Chapter 4. Here, the central focus is the determination of the short- and long-time self-diffusion coefficients as a function of the total area fraction, and the relation of these quantities to the structure of the system. Again, the monodisperse system is compared to a Monte Carlo simulation of hard disks, which is now used to clarify

the extent to which hydrodynamic and direct interactions impact upon the behaviour of particles at short and long times. In light of this, the applicability of simple theoretical expressions for the dependence of the short- and long-time self-diffusion coefficients upon the total area fraction in terms of the structure is discussed.

Following on from the study of the dynamic behaviour via the mean squared displacement, the behaviour of the self-intermediate scattering function and self-van Hove correlation function is considered in Chapter 5. In particular, the validity of the Gaussian approximation is probed in detail over a range of length and timescales. Deviations from Gaussian behaviour are discussed with respect to the hydrodynamic limits for colloidal systems and are quantified using the non-Gaussian parameter. Additionally, a scaling relation is developed to study the crossover between the diffusive regimes at short and long times.

Next, in Chapter 6, the study of dynamic properties is extended to collective phenomena and, more specifically, the process of interdiffusion in binary colloidal fluids. The thermodynamic and kinetic factors driving the process are considered separately, with the former determined from the concentration-concentration static structure factor and the latter from mean squared displacements of the centre of mass of a subset of particles. The extent to which interdiffusion can be described by the Darken equation i.e. by a linear combination of self-diffusion coefficients, is discussed in relation to the differing behaviour for systems at different compositions and size ratios.

Finally, in Chapter 7, the melting of quasi-two-dimensional colloidal hard spheres is studied by considering a monolayer of particles in sedimentation-diffusion equilibrium. The system is characterised by calculation of the density profile and the equation of state. The presence of a discontinuity in these functions indicates a coexistence gap and hence an interface. This interface is subsequently located by considering the bond-orientational order parameter. Fluctuations of the interface are analysed using capillary wave theory, with the resulting height-height correlations functions used to quantify both the size of the coexistence gap and the anisotropic stiffness of the interface.

Chapter 2

Theoretical background and experimental methods

ABSTRACT

In this thesis, the structural and dynamic behaviour of quasi-two-dimensional colloidal hard spheres is studied. In this Chapter, the statistical mechanical background used to describe properties of colloidal fluids and the experimental methods used to study them are presented. Firstly, the grand canonical ensemble and number fluctuations are described. Next, correlation functions used to characterise the structure of the system are considered, with emphasis here upon the radial distribution function and static structure factor and the thermodynamic quantities associated with them. For the dynamic properties, the van Hove correlation function, mean squared displacement and intermediate scattering functions are discussed. Finally, the experiments performed are described, including details of the colloidal model system, optical microscopy set-up and image processing used.

2.1 Statistical mechanics of colloidal liquids

In this thesis quasi-two-dimensional monolayers of particles with fixed particle number, fixed area and at fixed temperature are considered. A full description of the state of an N-particle system in two dimensions (2D) requires the knowledge of the $2N$ spatial coordinates of the particles, $\mathbf{r}^N$, and the $2N$ components of their momenta, $\mathbf{p}^N$, which define its point in the $4N$-dimensional phase space. From these $4N$ coordinates, it is possible to determine both the behaviour at a single particle level and, through functions of these coordinates, the macroscopic thermodynamic properties of the system. For a system at equilibrium, however, it is more convenient to consider these properties in a more general way using probability density functions of positions and momenta. The key problem is thus to find accurate expressions for the probability density functions at equilibrium.

The form of these functions will depend on the type of ensemble considered. While the experimental system as a whole has both fixed particle number and fixed area, experimental images are only taken over a small section of the monolayer leading to fluctuations in the particle number. Consequently, while the system as a whole would be described via the canonical ensemble, it is more appropriate to describe the imaged part of the system through the grand canonical ensemble.

In the grand canonical ensemble in 2D, the state of the system is defined by fixed values of the chemical potential, μ, area, A, and temperature, T .The number of particles, N, is allowed to fluctuate. The normalised equilibrium probability density function is [99, 100]

$$f_0(\mathbf{r}^N, \mathbf{p}^N, N) = \frac{1}{h^{2N} N!} \frac{\exp(-\beta(H - N\mu))}{\Xi}. \tag{2.1}$$

Equation (2.1) expresses the probability distribution for the system having N particles at positions $\mathbf{r}^N$ and with momenta $\mathbf{p}^N$. In this definition, h^{2N} and $N!$ arise from normalisation so that $\sum_{N=0}^{\infty} \int\int f_0(\mathbf{r}^N, \mathbf{p}^N, N) \mathrm{d}\mathbf{r}^N \mathrm{d}\mathbf{p}^N = 1$, where h is Planck's constant, and $\beta = 1/k_\mathrm{B}T$ with k_B the Boltzmann constant. The grand partition function in 2D, Ξ, is given by

$$\Xi = \sum_{N=0}^{\infty} \frac{1}{h^{2N} N!} \int\int \exp(-\beta(H - N\mu)) \mathrm{d}\mathbf{r}^N \mathrm{d}\mathbf{p}^N. \tag{2.2}$$

where H is the Hamiltonian, which for a system with no external field is

$$H(\mathbf{r}^N, \mathbf{p}^N) = K(\mathbf{p}^N) + V(\mathbf{r}^N). \tag{2.3}$$

Here, $K(\mathbf{p}^N)$ accounts for the contribution from the kinetic energy and $V(\mathbf{r}^N)$ for the contribution from the potential energy. If the integration over momenta in Equation (2.2) is performed, the kinetic part results in a contribution of $(2\pi m k_\mathrm{B} T)^N$ with m the particle mass. The integral over the potential energy term leads to the configuration integral, Z_N, where

$$Z_N = \int \exp(-\beta V(\mathbf{r}^N)) \mathrm{d}\mathbf{r}^N. \tag{2.4}$$

If we also define an activity, $z = \exp(\beta\mu)/\Lambda^2$, with $\Lambda = \left(h^2/2\pi m k_\mathrm{B} T\right)^{\frac{1}{2}}$, then

$$\Xi = \sum_{N=0}^{\infty} \frac{\exp(N\beta\mu)}{h^{2N} N!} (2\pi m k_\mathrm{B} T)^N Z_N = \sum_{N=0}^{\infty} \frac{z^N}{N!} Z_N. \tag{2.5}$$

Links to thermodynamic quantities are then realisable via the grand potential,

$$\Omega = -k_\mathrm{B} T \ln \Xi = -PA, \tag{2.6}$$

from the relation

$$d\Omega = -SdT - PdA - Nd\mu. \tag{2.7}$$

Note that P refers to the 2D analogue of the pressure.

2.1.1 Number fluctuations

In this thesis, the imaged experimental system exhibits fluctuations in the number of particles, and this is of particular interest as the variance of this quantity, $\langle N^2 \rangle - \langle N \rangle^2$ may be directly linked to the isothermal compressibility of the system, χ_T. The probability that a system has exactly N particles, $p(N)$, may be calculated from Equation (2.1), as

$$p(N) = \int \int f_0 \mathrm{d}\mathbf{r}^N \mathrm{d}\mathbf{p}^N = \frac{1}{\Xi} \frac{z^N}{N!} Z_N. \tag{2.8}$$

From this it follows that the average number of particles, $\langle N \rangle$, is

$$\langle N \rangle = \sum_{N=0}^{\infty} N p(N) = \frac{1}{\Xi} \sum_{N=0}^{\infty} N \frac{z^N}{N!} Z_N = \frac{z}{\Xi} \left(\frac{\partial \Xi}{\partial z} \right)_{A,T}, \tag{2.9}$$

with variance

$$\begin{aligned} \left(\frac{\partial \langle N \rangle}{\partial \ln z} \right) &= z \left(\frac{\partial \langle N \rangle}{\partial z} \right) \\ &= \frac{z}{\Xi} \sum_{N=0}^{\infty} N^2 \frac{z^{N-1}}{N!} Z_N - \frac{z}{\Xi^2} \left(\frac{\partial \Xi}{\partial z} \right)_{A,T} \sum_{N=0}^{\infty} N \frac{z^N}{N!} Z_N \\ &= \langle N^2 \rangle - \langle N \rangle^2. \end{aligned} \tag{2.10}$$

Using the definition of the activity, z, this may also be expressed as a derivative in terms of the chemical potential:

$$\left(\frac{\partial \langle N \rangle}{\partial \ln z} \right) = k_{\mathrm{B}} T \left(\frac{\partial \langle N \rangle}{\partial \mu} \right). \tag{2.11}$$

While the fluctuation in particle number is a property of the grand canonical ensemble, if the system is made very large the fluctuations vanish. This is the thermodynamic limit, and is defined as $\langle N \rangle \to \infty$ and $A \to \infty$ with density, $\rho = \frac{\langle N \rangle}{A}$ held constant. In this limit, therefore, $\langle N \rangle$ can be replaced with N and standard thermodynamic relations involving the number of particles used.

The 2D isothermal compressibility, χ_T, is defined in terms of partial derivatives as

$$\chi_T = -\frac{1}{A} \left(\frac{\partial A}{\partial P} \right)_T = \frac{1}{\rho} \left(\frac{\partial \rho}{\partial P} \right)_T = \frac{1}{\rho^2} \left(\frac{\partial \rho}{\partial \mu} \right)_T. \tag{2.12}$$

Combining Equations (2.10), (2.11) and (2.12) with

$$\left(\frac{\partial \rho}{\partial \mu} \right)_T = \frac{1}{A} \left(\frac{\partial N}{\partial \mu} \right)_T, \tag{2.13}$$

leads in the thermodynamic limit to the required link between the number fluctuations and the compressibility

$$\frac{\langle N^2 \rangle - \langle N \rangle^2}{\langle N \rangle} = \rho k_B T \chi_T. \tag{2.14}$$

2.1.2 The radial distribution function

The radial distribution function, $g(r)$, describes the correlation in the positions of pairs of particles and provides the simplest characterisation of the structure of a system. It may be interpreted as being proportional to the probability of finding a particle in an infinitesimal shell at a distance r from another particle. It plays a central role in the statistical mechanics of the liquid state as it often provides a sufficiently detailed description of structural correlations, making a consideration of the full probability density functions for all particles unnecessary. This is particularly relevant if pairwise interactions are assumed. Additionally, it is of importance due to the ease with which it may be measured experimentally.

The radial distribution function can be calculated from the full probability density function (Equation (2.1)) by an integration over all momentum coordinates and over $N-2$ position coordinates [99]. For a canonical ensemble, the probability of finding two particles in the area element $\mathrm{d}\mathbf{r}^{(2)}$ regardless of the positions of the remaining particles and momenta of all particles is [99]

$$\rho_N^{(2)}(\mathbf{r}^{(2)}) = \frac{N!}{(N-2)!}\frac{1}{Z_N}\int \exp\left(-\beta V(\mathbf{r}^N)\right)\mathrm{d}\mathbf{r}^{(N-2)}. \tag{2.15}$$

This is closely related to the 2-particle distribution function, $g_N^{(2)}(r)$, which is found by dividing by the product of single particle probability densities. For homogeneous systems, this single particle probability density is equal to the number density, ρ, so that

$$g_N^{(2)}(\mathbf{r}) = \frac{\rho_N^{(2)}(\mathbf{r})}{\rho^2} = \frac{A^2}{N^2}\frac{N!}{(N-2)!}\frac{1}{Z_N}\int \exp\left(-\beta V(\mathbf{r}^N)\right)d\mathbf{r}^{(N-2)}. \tag{2.16}$$

If the system is also isotropic the resulting function is the radial distribution function, $g(r)$, which now depends only upon the distance between particles, with

$$g_N^{(2)}(\mathbf{r}) = \frac{A^2(N-1)}{NZ_N}\int \exp\left(-\beta V(\mathbf{r}^N)\right)\mathrm{d}\mathbf{r}^{(N-2)}. \tag{2.17}$$

The radial distribution function may alternatively be expressed using definitions of the particle

density in terms of delta functions, with the 1-particle density

$$\rho_N^{(1)}(\mathbf{r}) = \left\langle \sum_{i=1}^{N} \delta(\mathbf{r} - \mathbf{r_i}) \right\rangle \tag{2.18}$$

and the 2-particle density function

$$\rho_N^{(2)}(\mathbf{r'}, \mathbf{r''}) = \left\langle \sum_{i=1}^{N} \sum_{j \neq i}^{N} \delta(\mathbf{r'} - \mathbf{r_i})\, \delta(\mathbf{r''} - \mathbf{r_j}) \right\rangle. \tag{2.19}$$

As $\rho_N^{(2)}(\mathbf{r'}, \mathbf{r''})$ will only be non-zero if $\mathbf{r'} = \mathbf{r_i}$ and $\mathbf{r''} = \mathbf{r_j}$, Equation (2.19) may be rewritten in terms of a single delta function for the distance between the particles, $\mathbf{r} = \mathbf{r'} - \mathbf{r''} = \mathbf{r_i} - \mathbf{r_j}$ as

$$\rho_N^{(2)}(\mathbf{r}) = \frac{1}{A} \left\langle \sum_{i=1}^{N} \sum_{j \neq i}^{N} \delta(\mathbf{r} - (\mathbf{r_i} - \mathbf{r_j})) \right\rangle. \tag{2.20}$$

Here, a factor of $1/A$ must be included to account for the absolute position of the two particles within the system. The radial distribution function simply follows from Equation (2.16) as

$$g(r) = \frac{1}{N\rho} \left\langle \sum_{i=1}^{N} \sum_{j \neq i}^{N} \delta(\mathbf{r} - \mathbf{r}_i + \mathbf{r}_j) \right\rangle. \tag{2.21}$$

The definition of the 2-particle density function, and thus $g(r)$, can also be extended to the grand canonical ensemble. In this ensemble,

$$\rho^{(2)}(\mathbf{r}^{(2)}) = \sum_{N=2}^{\infty} p(N) \rho_N^{(2)}(\mathbf{r}^{(2)}), \tag{2.22}$$

where $p(N)$ is the probability that the system has N particles (Equation (2.8)) and $\rho_N^{(2)}(\mathbf{r}^{(2)})$ is the canonical 2-particle density function. Therefore, for a homogeneous, isotropic system

$$g(r) = \frac{\rho^{(2)}(r)}{\rho^2}. \tag{2.23}$$

As N is not fixed, the n-particle density functions in the grand canonical ensemble are normalised

such that

$$\begin{aligned}\int \rho^{(n)}(\mathbf{r}^{(n)})\mathrm{d}\mathbf{r}^{(n)} &= \int \left\{ \frac{1}{\Xi} \sum_{N\geq n}^{\infty} \frac{z^N}{(N-n)!} \int \exp(-\beta V(\mathbf{r}^N))\mathrm{d}\mathbf{r}^{(N-n)} \right\} \mathrm{d}\mathbf{r}^{(n)} \\ &= \int \left\{ \sum_{N\geq n}^{\infty} \frac{N!}{(N-n)!} p(N) \right\} \mathrm{d}\mathbf{r}^{(n)} \\ &= \left\langle \frac{N!}{(N-n)!} \right\rangle . \end{aligned} \tag{2.24}$$

Therefore, the radial distribution function may now be related to the variance of the number fluctuations within the system by forming the expression

$$\int\int \left[\rho^{(2)}(\mathbf{r}_1,\mathbf{r}_2) - \rho^{(1)}(\mathbf{r}_1)\rho^{(1)}(\mathbf{r}_2)\right] \mathrm{d}\mathbf{r}_1\mathrm{d}\mathbf{r}_2 = \langle N^2\rangle - \langle N\rangle - \langle N\rangle^2, \tag{2.25}$$

which for a homogeneous system may be rearranged as

$$\begin{aligned}\frac{\langle N^2\rangle - \langle N\rangle^2}{\langle N\rangle} &= \frac{1}{\langle N\rangle} \left\{ \langle N\rangle + \int\int \left[\rho^2 g(\mathbf{r}) - \rho^{(1)}(\mathbf{r}_1)\rho^{(1)}(\mathbf{r}_2)\right] \mathrm{d}\mathbf{r}_1\mathrm{d}\mathbf{r}_2 \right\} \\ &= \frac{1}{\langle N\rangle} \left\{ \langle N\rangle + A\int \left[\rho^2 g(r) - \rho^2\right] \mathrm{d}r \right\} \\ &= 1 + \rho \int [g(r) - 1]\mathrm{d}r. \end{aligned} \tag{2.26}$$

Following Equation (2.14) this implies

$$1 + \rho \int [g(r) - 1]dr = \rho k_B T \chi_T, \tag{2.27}$$

thus allowing the isothermal compressibility to be calculated from $g(r)$ within the grand canonical ensemble.

2.1.3 The equation of state from the radial distribution function

Another key thermodynamic property which may be calculated from $g(r)$ is the equation of state via the virial function [99], where

$$\frac{\beta P}{\rho} = 1 - \frac{\pi\beta\rho}{2} \int r^2 \frac{\mathrm{d}v(r)}{\mathrm{d}r} g(r)\mathrm{d}r. \tag{2.28}$$

with $v(r)$ the pair potential. For the particular case of hard spheres or hard disks, which are the focus of this thesis, this is difficult to solve due to the discontinuous nature of the pair potential (Equation (1.1)). As such, we require the definition of a new function,

$$y(r) = \exp(\beta v(r))g(r), \tag{2.29}$$

which transforms Equation (2.28) as

$$\begin{aligned}\frac{\beta P}{\rho} &= 1 - \frac{\pi\beta\rho}{2}\int r^2 \frac{\mathrm{d}v(r)}{\mathrm{d}r}\exp(-\beta v(r))y(r)\mathrm{d}r \\ &= 1 + \frac{\pi\rho}{2}\int r^2 \frac{\mathrm{d}(\exp(-\beta v(r)))}{\mathrm{d}r}y(r)\mathrm{d}r.\end{aligned} \tag{2.30}$$

As $v(r)$ is either ∞ for $r < \sigma$ or 0 for $r \geq \sigma$, the derivative of $\exp(-\beta v(r))$ is a delta function. Hence,

$$\begin{aligned}\frac{\beta P}{\rho} &= 1 + \frac{\pi\rho}{2}\int_0^\infty r^2\delta(r-\sigma)y(r)\mathrm{d}r \\ &= 1 + \frac{\pi\rho}{2}\sigma^2 g(\sigma) \\ &= 1 + 2\phi g(\sigma),\end{aligned} \tag{2.31}$$

with ϕ the area fraction. It can be seen from Equation (2.31) that for a hard disk system the equation of state, and so the pressure, depends only upon the contact value of the radial distribution function, i.e. the value of $g(r)$ for $r = \sigma$.

2.1.4 The static structure factor

In many experimental studies of molecular liquids [101, 102] and of colloidal fluids [103, 104] measurements are made by scattering techniques. It is, therefore, Fourier components, $\rho_{\mathbf{k}}$, of the microscopic density rather than particle positions in real space that are considered, where

$$\rho_{\mathbf{k}} = \sum_{i=1}^{N} \exp(-i\mathbf{k}\cdot\mathbf{r}_i), \tag{2.32}$$

with $\mathbf{k}$ the wavevector which is related to the real space lengthscale, L, as $2\pi/L$. The function equivalent to the radial distribution function in Fourier space is the static structure factor, $S(\mathbf{k})$,

which can be expressed in terms of $\rho_{\mathbf{k}}$ as

$$\begin{aligned} S(\mathbf{k}) &= \frac{1}{N}\left\langle \rho_{\mathbf{k}} \cdot \rho_{-\mathbf{k}} \right\rangle \\ &= \frac{1}{N}\left\langle \sum_{i=1}^{N}\sum_{j=1}^{N} \exp(-i\mathbf{k}\cdot(\mathbf{r}_i - \mathbf{r}_j)) \right\rangle . \end{aligned} \tag{2.33}$$

The relation between the microscopic densities in real and Fourier space implies that $S(\mathbf{k})$ may also be expressed in terms of $g(r)$ (Equation (2.17)). This relation may be determined as

$$\begin{aligned} S(\mathbf{k}) &= 1 + \frac{1}{N}\left\langle \sum_{i=1}^{N}\sum_{j\neq i}^{N} \exp(-i\mathbf{k}\cdot(\mathbf{r}_i - \mathbf{r}_j)) \right\rangle \\ &= 1 + \frac{1}{NZ_N}\int \exp(-i\mathbf{k}\cdot(\mathbf{r}_i - \mathbf{r}_j)) \exp(-\beta V(\mathbf{r}^N))\mathrm{d}\mathbf{r}^N \\ &= 1 + \frac{N(N-1)}{N}\int\int \exp(-i\mathbf{k}\cdot(\mathbf{r}_1 - \mathbf{r}_2))\frac{Ng(r)}{A^2(N-1)}\mathrm{d}\mathbf{r}^{(1)}\mathrm{d}\mathbf{r}^{(2)} \\ &= 1 + \rho\int \exp(-i\mathbf{k}\cdot\mathbf{r})g(r)\mathrm{d}\mathbf{r}. \end{aligned} \tag{2.34}$$

Further manipulation of the expression leads to

$$\begin{aligned} S(\mathbf{k}) &= 1 + \rho\int \exp(-i\mathbf{k}\cdot\mathbf{r})(g(r)-1)\mathrm{d}\mathbf{r} + \rho\int \exp(-i\mathbf{k}\cdot\mathbf{r})\mathrm{d}\mathbf{r} \\ &\approx 1 + \rho\int \exp(-i\mathbf{k}\cdot\mathbf{r})(g(r)-1)\mathrm{d}\mathbf{r}, \end{aligned} \tag{2.35}$$

where the second line is exact for $\mathbf{k} \neq 0$. Therefore, by comparison to Equations (2.14) and (2.27) it can be shown that

$$S(\mathbf{k}\to 0) = \rho k_{\mathrm{B}} T \chi_T = \frac{\langle N^2\rangle - \langle N\rangle^2}{\langle N\rangle}. \tag{2.36}$$

This result is important as it demonstrates that the $\mathbf{k} \to 0$ limit of the static structure factor may be approximated by a consideration of the number fluctuations.

2.1.5 Dynamics

The dynamic behaviour of single particles may be described using time-correlation functions. These are the analogues of the structural correlation functions but now with the single particle

density as a time dependent quantity

$$\rho(\mathbf{r},t) = \sum_{i=1}^{N} \delta[\mathbf{r} - \mathbf{r}_i(t)], \tag{2.37}$$

where $\mathbf{r}_i$ is the position of particle i at time t. In real space the most important time-dependent correlation function is the van Hove correlation function,

$$G(\mathbf{r},t) = \frac{1}{\rho}\left\langle \rho(\mathbf{r},t)\rho(\mathbf{r}_0,0)\right\rangle = \left\langle \frac{1}{N}\sum_{i=1}^{N}\sum_{j=1}^{N}\delta[\mathbf{r} - \mathbf{r}_j(t) + \mathbf{r}_i(0)]\right\rangle, \tag{2.38}$$

which probes correlations in the positions of particles over time. Here, the double sum may be split into terms for $i = j$ and for $i \neq j$ resulting in

$$\begin{aligned} G(\mathbf{r},t) &= \left\langle \frac{1}{N}\sum_{i=1}^{N}\delta[\mathbf{r} - \mathbf{r}_i(t) + \mathbf{r}_i(0)]\right\rangle + \left\langle \frac{1}{N}\sum_{i=1}^{N}\sum_{j\neq i}^{N}\delta[\mathbf{r} - \mathbf{r}_j(t) + \mathbf{r}_i(0)]\right\rangle \\ &= G_s(\mathbf{r},t) + G_d(\mathbf{r},t), \end{aligned} \tag{2.39}$$

where $G_s(\mathbf{r},t)$ and $G_d(\mathbf{r},t)$ are the self and distinct parts of the van Hove function. As a whole, the van Hove correlation function reflects the probability that a particle will be found at position $\mathbf{r}$ at time t given that there was a particle at position $\mathbf{r}(0)$ at $t = 0$. The two parts differ in that for the self part, the same particle is considered at both times whereas for the distinct part the positions are those of different particles. As the latter probes correlations between differing particles, for $t = 0$, $G_d(\mathbf{r}, t = 0) = \rho g(r)$.

Of particular importance is the second moment of $G_s(\mathbf{r},t)$, which is the mean squared displacement (MSD):

$$\langle \delta r^2(t)\rangle = \int r^2\, G_s(\mathbf{r},t)\mathrm{d}\mathbf{r}. \tag{2.40}$$

The MSD may also be calculated directly from particle trajectories as

$$\langle \delta r^2(t)\rangle = \frac{1}{N}\sum_{i=1}^{N}\left\langle [\mathbf{r}_i(t) - \mathbf{r}_i(0)]^2\right\rangle, \tag{2.41}$$

with $\mathbf{r}_i$ the position of particle i, N the number of particles and $\langle \dots \rangle$ the average over different time origins. The ability to average over different time origins arises from the assumption of

stationarity, i.e. that to determine the change in a property after a certain time interval, any point in the trajectory may be chosen as the time origin. If the trajectories of the particles can be described as a random walk, the mean squared displacement can be linked directly to the diffusion coefficient. In 2D, this is equal to

$$\left\langle \delta r^2(t) \right\rangle = 4Dt, \tag{2.42}$$

where D is the appropriate diffusion coefficient for the process. For a single particle moving in a three-dimensional fluid the value of this coefficient is determined from the Einstein expression,

$$D = \frac{k_{\mathrm{B}}T}{3\pi\eta\sigma}, \tag{2.43}$$

where η is the solvent viscosity and σ the particle diameter. For systems of many particles, the value of the diffusion coefficient depends upon the interparticle interactions. The result of this is that D displays a dependence on time, arising from the timescales over which differing interactions impact on the motion of a particle. For colloidal systems, two diffusion coefficients may be defined: a short-time diffusion coefficient, characterising the diffusive motion of the particle in the initial time regime where particles interact hydrodynamically but not directly, and a long-time diffusion coefficient characterising the motion at later times when the particle has interacted directly with many particles, and as such feels the configuration of the system in an averaged sense. This is in contrast to the behaviour of molecular systems, where the long-time dynamics are diffusive but the initial motion is ballistic, with $\left\langle \delta r^2(t) \right\rangle \propto t^2$.

Finally, in Fourier space the relevant correlation function is the intermediate scattering function (ISF), $F(\mathbf{k}, t)$, which is defined as

$$F(\mathbf{k}, t) = \frac{1}{N} \left\langle \rho_{\mathbf{k}}(t)\rho_{-\mathbf{k}}(0) \right\rangle . \tag{2.44}$$

This is the spatial Fourier transform of the van Hove correlation function (Equation (2.39)), and similarly can be split into the self- (or incoherent-) ISF

$$F_s(\mathbf{k}, t) = \left\langle \exp[i\mathbf{k} \cdot (\mathbf{r}_i(t) - \mathbf{r}_i(0))] \right\rangle , \tag{2.45}$$

which considers correlations in the behaviour of a particle with itself, and the coherent ISF

$$F_c(\mathbf{k},t) = \left\langle \sum_{i=1}^{N}\sum_{j\neq i}^{N} \exp[i\mathbf{k}\cdot(\mathbf{r}_j(t)-\mathbf{r}_i(0))] \right\rangle, \tag{2.46}$$

which considers the correlations between different particles. The self-intermediate scattering function and the mean squared displacement both characterise the self-motion of a tagged particle, though the MSD is in general more sensitive to the faster moving particles and the self-ISF more sensitive to slower moving particles. Consequently, the two functions provide complementary information, which is particularly useful if studying systems with heterogeneous dynamics.

2.2 Colloidal model systems

Colloidal suspensions are an experimental system for which the statistical mechanics described in the previous section is relevant. These are systems consisting of particles with at least one lengthscale in the range of 10 nm to 10 μm dispersed in a continuous medium. The size of the colloidal particles is small enough relative to the solvent molecules to result in Brownian motion, which in turn leads to a phase behaviour analogous to atomic and molecular systems [24]. This particle motion is associated with a characteristic timescale, the Brownian time, τ_B, defined as

$$\tau_\mathrm{B} = \frac{\sigma^2}{4D}, \quad \text{with} \quad D = \frac{k_\mathrm{B}T}{\xi}. \tag{2.47}$$

Here, σ is the particle diameter, D the diffusion coefficient and ξ the friction coefficient. As such, τ_B is the time taken for a particle to diffuse over its own diameter. Consequently, the typical lengthscale on the order of μm leads to a timescale on the order of seconds, which allows for the study of colloidal systems in real space and time.

The scale of colloidal particles also allows for their confinement either by gravity or other physical means. The gravitational confinement may be quantified by the gravitational height, h_g, calculated as

$$h_g = \frac{6k_\mathrm{B}T}{\pi\sigma^3 g\Delta\tilde{\rho}_{p-s}}, \tag{2.48}$$

with g the acceleration due to gravity and $\Delta\tilde{\rho}_{p-s}$ the difference in mass density between particle

and solvent. This quantity describes the distance a particle may move against gravity due to thermal energy and may be tuned through the mass density mismatch between particle and solvent or, more sensitively, by σ.

Colloidal systems are also highly tunable with respect to their interaction potential, $v(r)$. In general $v(r)$ displays two basic features; a strongly repulsive interaction at short distances combined with a longer-ranged van der Waals attraction. This potential may then be modified in a number of ways, for example by changing the refractive index mismatch between solvent and particle or by the modification of the surface of the particle. In this thesis, the particles used have been functionalised to include carboxylate surface groups, and thus will bear a negative charge in the solvent used. Consequently, the interactions between particles can be modelled as a screened Coulomb (Yukawa) potential of the form

$$\frac{v(r)}{k_B T} = \begin{cases} \infty & \text{for } r < \sigma \\ Z^2 \lambda_B \left(\frac{\exp(\kappa\sigma)}{1+\kappa\sigma} \right)^2 \frac{\exp(-\kappa r)}{r} & \text{for } r \geq \sigma. \end{cases} \tag{2.49}$$

Here, Z is the effective charge number of the spheres, κ^{-1} is the Debye length and λ_B is the Bjerrum length, which describes the thermal separation for unit charges. The form of the potential arises from the modified distribution of ions in solution which results from the surface charge of the particle. Equation (2.49) implies that to realise an experimental hard sphere model system it is necessary to ensure that κ^{-1} is very small, which is achievable by a high ionic strength of the solution.

Finally, it should also be noted that colloidal suspensions deviate from atomic systems in a number of respects. Firstly, in contrast to molecular and atomic systems, the particles of a colloidal suspension are not identical, displaying some degree of polydispersity. Secondly, the presence of the solvent leads to key differences in the dynamic behaviour. This is seen both in the fact that colloidal systems display Brownian rather than Newtonian dynamics and that colloidal particles display solvent-mediated hydrodynamic interactions in addition to the direct interactions, which are governed by the interaction potential.

2.3 Experimental methods

2.3.1 Colloidal model system

In this thesis, we consider a quasi-2D colloidal system, consisting of a monolayer of particles confined to the base of a glass sample cell. The colloidal particles are spherical, carboxylic acid functionalized melamine formaldehyde particles (Microparticles GmbH) with mass density, $\tilde{\rho} = 1510$ kg m^{-3}, refractive index of 1.68 and diameters of $\sigma = 2.79$ μm, $\sigma = 4.04$ μm and $\sigma = 6.10$ μm. The particles are highly monodisperse, with polydispersities (PD) determined from scanning electron microscopy to be 2.1% and 1.2% for the 2.79 μm and 4.04 μm particles, respectively. Important quantities related to the colloidal particles, including their Brownian times, τ_{B}, and gravitational heights, h_g, are summarised in the Table in Figure 2.1.

The particles are dispersed in a 20/80 v/v% ethanol/water mixture to form a dilute suspension, with the carboxylic acid functionalisation resulting in a negative charge on the particle surface in solution. This leads to a short range repulsion between the particles, and between the particles and the wall of the cell, which minimizes particle aggregation and suppresses the tendency of particles to stick to the wall of the sample cell. Note that the Debye length was not determined for our system as the radial distribution functions and the equation of state show that the particles effectively behave as hard spheres (see Chapter 3). The ethanol-water mixture has a density of 971 kg m^{-3} and a viscosity of 1.60×10^3 Pa s [105] and is used both to inhibit the growth of bacteria and to lower the surface tension, enabling the suspension to be easily loaded into the cell.

σ (μm)	PD (%)	τ_{B} (s)	h_g (μm)
2.79	2.1	45	0.068
4.04	1.2	151	0.023
6.10	2.0[1]	324	0.0067

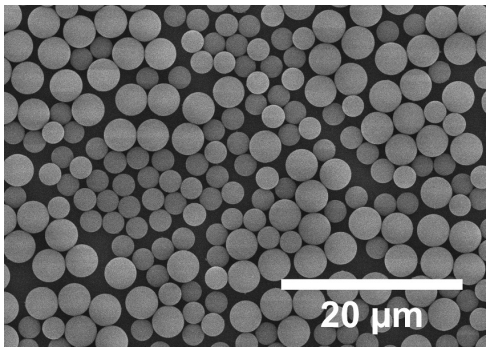

Figure 2.1: A summary of the quantities used to characterise the colloidal particles, with a scanning electron microscopy (SEM) image of a mixture containing 2.79 μm and 4.04 μm particles. [1] Value from manufacturer.

The sample cell used is a custom-made quartz glass Hellma cell with internal width of 9 mm, internal length of 20 mm and internal height of 200 μm (see Figure 2.3a inset). It is cleaned prior to use by heating for 30 minutes at approximately 50°C in a 2% solution of Hellmanex®, drying at 80°C on a hot plate, and then plasma cleaning. This removes any contaminants from the surface of the cell. Following insertion of the sample, the ports of the cell are sealed using Blu-tack to prevent contamination of the sample and evaporation. The high mass density of the melamine particles relative to the solvent results in their rapid sedimentation onto the base of the cell, with the concentration of the suspension tuned such that a single layer is formed. The gravitational height of the particles (see Figure 2.1) is an extremely small fraction of their size, resulting in negligible fluctuations out of the plane. As such, the system is structurally two-dimensional with respect to the colloidal particles but three-dimensional with respect to the fluid. The system is therefore described as quasi-two-dimensional.

The colloidal systems are studied at a range of total area fractions

$$\phi_t = \frac{N\pi\sigma^2}{4A} \tag{2.50}$$

with N the number of particles and A the area of the system. For binary systems, this is the sum of the area fraction of small and large particles, $\phi_t = \phi_l + \phi_s$. Additionally, for the binary systems there may also be variation with respect to the composition, i.e. the relative area fractions of each of the two components. This is denoted by the parameter, q, where

$$q = \frac{\phi_l}{\phi_t}, \tag{2.51}$$

which thus runs from $q = 0$ for systems of only small particles to $q = 1$ for systems of only large particles. Two different binary mixtures are considered in this thesis: one comprised of mixtures of 2.79 μm and 4.04 μm with size ratio, $\gamma = \sigma_l/\sigma_s = 1.45$ and another comprised of particles with diameters of 2.79 μm and 6.10 μm, with size ratio, $\gamma = 2.19$. These are both at relatively small size ratio, but here we shall describe the $\gamma = 1.45$ system as that at a small size ratio and the $\gamma = 2.19$ system as that at a large size ratio. Note that the centres of the large and small particles do not lie in the same plane when sedimented. To account for this an effective diameter for the large particles can be defined in the plane of the centres of the small particles. For the 2.79 μm and 4.04 μm particles the difference between real and effective diameter is very

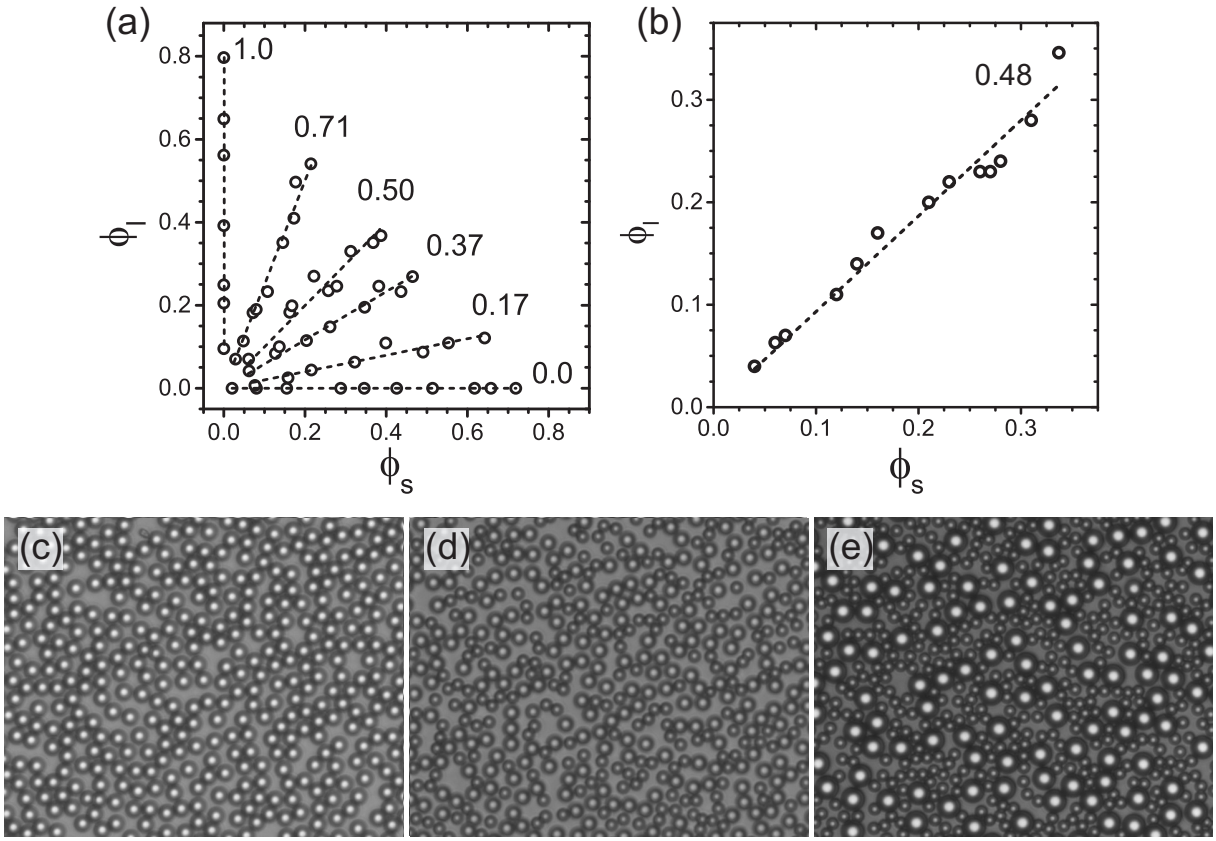

Figure 2.2: State diagrams exhibiting the range of system compositions, $q = \phi_l/\phi_t$, studied for the binary system with (a) $\gamma = 1.45$ and (b) $\gamma = 2.19$. Here the labels indicate the value of q. Note that the two monodisperse systems are represented as the lines $q = 0$ and $q = 1$ in panel (a). Typical experimental images of systems at $\phi_t \approx 0.5$ are shown for: (c) $\sigma = 4.04$ μm monodisperse system ($q = 1$); (d) binary system with $\gamma = 1.45$ and $q = 0.71$; (e) binary system with $\gamma = 2.19$ and $q = 0.48$.

small, however, for the 6.10 μm particles the larger size ratio results in a significant difference in effective particle diameter. Consequently, for the system at $\gamma = 2.19$, the area fraction is calculated using the effective diameter for the 6.10 μm particles.

The full range of systems considered are shown in the state diagrams in Figure 2.2a and b. A common value of $q \approx 0.5$ is considered for both size ratios. It is also possible, however, to compare the systems with respect to number concentration, c_i, where $c_i = N_i/N$ with N_i the number of one type of particles. The closest comparison between the large and small size ratio systems with respect to number concentrations is between the $q = 0.37$ small size ratio system and the $q = 0.48$ large size ratio system. Typical images of some of the compositions considered at a total area fraction of $\phi_t \approx 0.5$ are shown in Figure 2.2c-e.

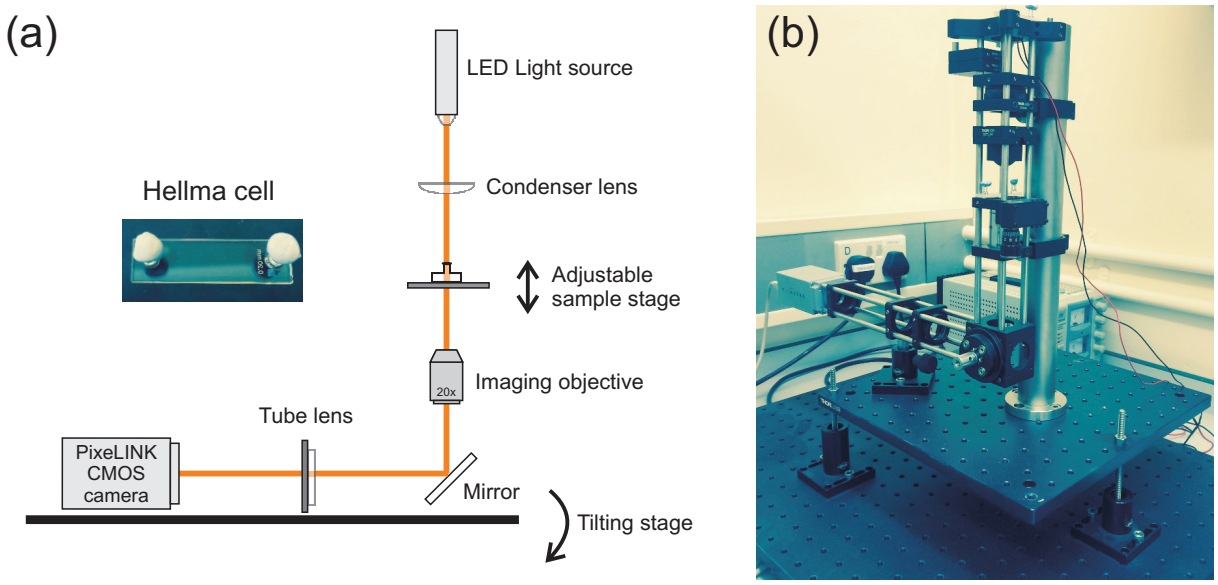

Figure 2.3: (a) A schematic of the custom-built tilting optical microscopy set-up. Inset: an image of the sample cell used. (b) The tilting microscopy set-up.

2.3.2 Video-microscopy

All of the data acquisition is performed using optical video-microscopy set-ups. Experiments described in Chapter 3 to Chapter 6 utilise an Olympus inverted bright-field microscope while those in Chapter 7 use a custom-built inverted bright field microscope instead which allows for the set-up to be tilted to a small angle. Objectives with magnification of 20× and 40× are used and images are recorded on a PixeLINK CMOS camera and saved as 8-bit 1280 × 1024 pixel images. The schematic of the tilted microscope set-up is shown in Figure 2.3a.

By tilting the microscope, gravitational heights parallel and perpendicular to the base of the sample cell are introduced, and defined as

$$h_{g\parallel} = \frac{6k_BT}{\pi\sigma^3 g \sin\alpha\Delta\tilde{\rho}_{p-s}} \quad \text{and} \quad h_{g\perp} = \frac{6k_BT}{\pi\sigma^3 g \cos\alpha\Delta\tilde{\rho}_{p-s}}, \tag{2.52}$$

with α the tilt angle (see Figure 2.4a). For small angles, the two gravitational heights can be tuned such that fluctuations perpendicular to the base of the cell are still sufficiently suppressed, but the gravitational height parallel to the base of the cell is on the order of the particle diameter. This allows for significant movement of the particles up the plane and results in a wide density gradient and interface, as shown in Figure 2.4b.

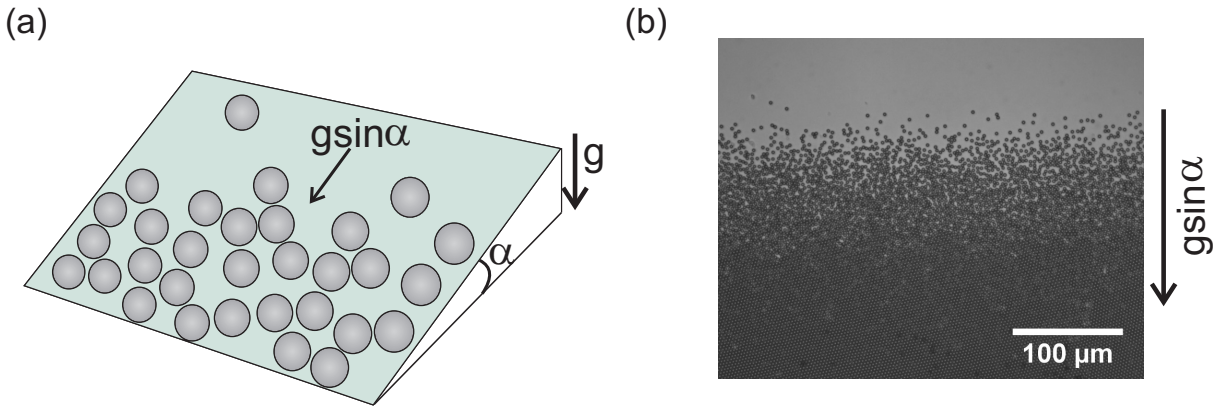

Figure 2.4: (a) A diagram to show the effect of tilting the sample by a small angle, α, and the resultant in-plane component of g. (b) An example of the experimental images acquired from tilted microscopy experiments for $\alpha = 0.56°$.

2.3.3 Image analysis

Tracking routines developed by Crocker and Grier [106] are used to acquire particle positions and trajectories from the microscopy images. The processing steps involved are illustrated in Figure 2.5. First, a bandpass filter is applied to subtract the background noise and smooth the image. This results in an image in which there are many uniform, circular, bright features, as shown in Figure 2.5b. Parameters used here are varied dependent upon the size of the particles in the system, however this does not remove all of the unwanted bright signals arising from the background and, in particular, from interstitials. Particles are then located using a further routine in which a Gaussian fit to the bright spots determines the position of their centres. In addition to the particle coordinates, the position finding routine also calculates the brightness, radius of gyration and eccentricity of features. The application of conditions on these values allows unwanted items to be eliminated and large and small particles to be distinguished (Figure 2.5c and d). As the bright particle centres following the bandpass procedure are many pixels in diameter, the error in position is very small, and is estimated from a consideration of the mean squared displacement to be 12 ± 10 nm [61]. For the determination of dynamic properties a tracking routine is used to link coordinates into trajectories by the association of a particle identity to each coordinate found. The subset of particles tracked may be controlled by specifying the starting positions of particles of interest or the minimum length of trajectory. In the work described in Chapter 7 the lower magnification makes the distinction between particles and bright interstitials more challenging. Here, the transient interstitials may be removed using a condition on track length, with particle positions subsequently determined from the tracked

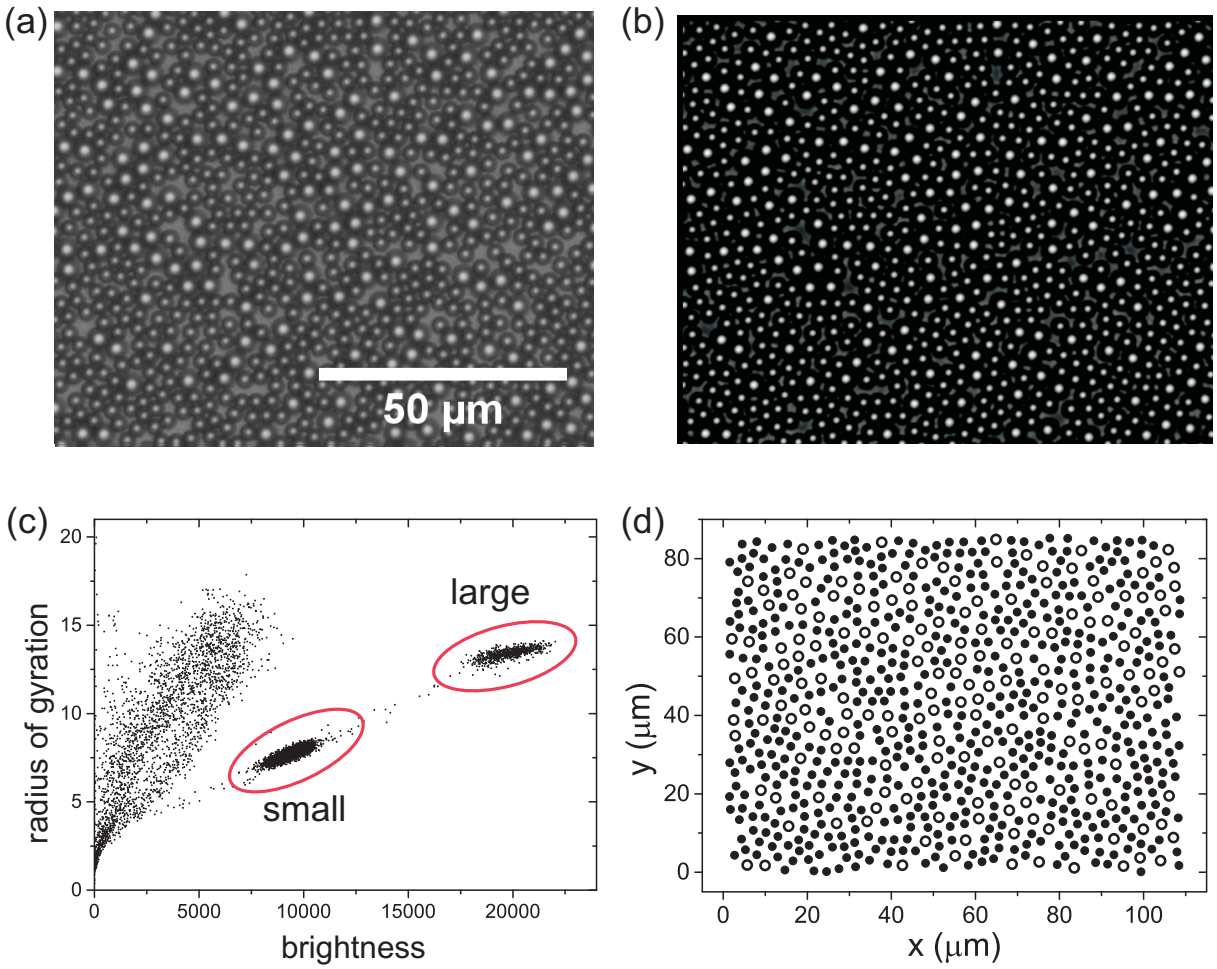

Figure 2.5: Sample images to illustrate the particle tracking procedure: (a) A raw experimental image of a binary system at $\gamma = 1.45$, $q = 0.37$ and $\phi_t = 0.63$; (b) The same image following the bandpass procedure; (c) A plot of radius of gyration versus brightness for all features initially found. Small and large particle subsets are indicated, with remaining features those of the interstitials; (d) A plot of the particle coordinates for the small and large particle subsets, plotted in filled and open symbols respectively.

data. This results in large arrays of data comprised of the x and y positions over time for each particle. These may be further analysed to determine properties of the system such as correlation functions.

Acknowledgements

Michael Juniper, Arran Curran, Thomas Skinner, Lia Verhoeff and Joshua Abbott are thanked for practical assistance.

Chapter 3

Structure and fluctuations of quasi-two-dimensional binary colloidal fluids

ABSTRACT

In this Chapter, a full characterisation of the equilibrium structure of monodisperse and bidisperse quasi-two-dimensional colloidal fluids is presented. Firstly, the radial distribution function, $g(r)$, is computed and compared to results from fundamental measure theory and Monte Carlo simulation for hard disks, demonstrating that the monodisperse and small size ratio binary systems are excellent model hard disk systems. Next, the static structure factor, $S(k)$, is computed, and an analysis of number fluctuations used to obtain the $S(k \to 0)$ limit. Further to this, an analysis of the contact value of $g(r)$ and the $k \to 0$ limit of $S(k)$ is used to confirm the equation of state. Finally, a binary system with a larger size ratio is considered, where the enhanced negative nonadditivity leads to significantly different behaviour.

3.1 Introduction

The structure of liquids is characterised by a high particle density combined with a lack of long-range order, and thus lies between that of solids and gases. This makes a theoretical description of liquids very difficult as neither descriptions based upon random order and low density relevant to gases, or of well defined long-range order applicable to crystals are appropriate. Therefore, a powerful tool in the analysis of the structure of liquids are correlation functions. Of particularly wide-ranging use are the two-point correlation functions, the radial distribution function, $g(r)$, and its Fourier transform, the static structure factor, $S(k)$.

These give an immediate indication of the degree of structural order and the softness of the interaction potential. They also provide all the information necessary for the calculation of many important thermodynamic quantities, including the equation of state [99]. Furthermore, dynamic quantities, such as the diffusion coefficient and the intermediate scattering function, are often directly linked to structural measures [66,107,108]. As such, the accurate determination of these functions is of great importance and significant effort has been devoted to this problem, in particular for hard sphere and hard disk systems both theoretically [109–113] and in computer simulations [72, 73, 114–116].

Experimental determination of both $g(r)$ and $S(k)$ for colloidal suspensions in three dimensions (3D) was achieved first in scattering experiments [103], and later directly by confocal microscopy [117–119]. Here, the choice of which function to calculate directly from experiment is determined by the experimental method utilised. In the case of scattering experiments, only $S(k)$ is directly accessible, whereas for microscopy, the natural choice is the real space function $g(r)$, though it is possible to calculate both quantities directly from particle coordinates [120].

For the consideration of two-dimensional (2D) systems, simple scattering experiments equivalent to those used for 3D systems are difficult. While it is possible to perform more complex scattering experiments such as evanescent wave dynamic light scattering, these have only been used to consider dynamic properties [69, 121]. This implies that for quasi-two-dimensional systems, real space measurements from microscopy dominate and the structure is primarily characterised using $g(r)$. The radial distribution function has been measured for a variety of quasi-2D colloidal systems and compared to computer simulations and theories [53, 58, 120, 122–127].

The structure of quasi-2D binary systems, consisting of two sizes of particle, has also become a subject of increasing interest due to the widespread use of these systems as model glass-formers [67, 128–130]. This is more challenging both for experiment and theory, due to the need to account for correlations between like and unlike particles, and for the ensuing introduction of complex packing effects.

In this Chapter an extensive structural characterisation of the monodisperse and bidisperse quasi-2D colloidal systems used in this thesis is presented. A comparison of the radial distribution functions to both fundamental measure theory and a Monte Carlo simulation for hard disks is used to demonstrate that the system is an excellent model hard disk system. The difficulties in the calculation of structural correlation functions for quantitative use are discussed, and in particular the accurate determination of the contact value of the radial distribution function that directly leads to the equation of state. Static structure factors and their linear combinations for the same experimental systems are also calculated directly from particle positions and presented with the relevant fluctuation analysis necessary to calculate the $k \to 0$ limit of these functions. Finally, the differing behaviour of systems with a larger size ratio is discussed in relation to the nonadditivity within the system.

3.2 Experimental methods and data analysis

3.2.1 Colloidal model system

The quasi-2D colloidal system used is described in Section 2.3.1. Here, the structural behaviour of monodisperse systems of particles with diameter $\sigma = 2.79$ μm and $\sigma = 4.04$ μm and binary systems at size ratios $\gamma = \sigma_l/\sigma_s = 1.45$ and $\gamma = 2.19$ are considered. Images are recorded at two frames per second and particle coordinates are obtained as described in Sections 2.3.1 and 2.3.3. Correlation functions are calculated from the particle positions for at least 200 frames of data. For all systems, the total packing fraction, $\phi_t = \rho\pi\sigma^2/4$, is varied over the entire range of densities characteristic of a fluid (approximately $\phi_t = 0.02$ to 0.66). For the small size ratio system, compositions defined by $q = \phi_l/\phi_t$, with ϕ_l the area fraction of large particles, of $q = 0.17$, 0.37, 0.50 and 0.71 are considered. The large size ratio binary system is considered at only $q = 0.48$. The full range of systems studied are detailed in the state diagrams in Figure 2.2.

3.2.2 Structural correlation functions

The total and partial radial distribution functions, $g_{ij}(r)$, are computed from the particle coordinates via the expression [99]

$$c_i c_j g_{ij}(r) = \frac{1}{\rho}\left\langle \frac{1}{N}\sum_{\mu=1}^{N_i}\sum_{\nu\neq\mu}^{N_j}\delta(\mathbf{r}+\mathbf{r}_\mu-\mathbf{r}_\nu)\right\rangle. \tag{3.1}$$

Here, N is the total number of particles, $\rho = N/A$ the total number density of the system with A the surface area, $c_{i,j} = N_{i,j}/N$ the fraction of species i or j and $\mathbf{r}_{\mu,\nu}$ the position of particle μ of species i or ν of species j, respectively. This is a more general form of $g(r)$ than that discussed in Section 2.1.2 and allows for the calculation of partial radial distribution functions for bidisperse systems, describing the correlations between like, and/or unlike particles. For a system consisting of two species, here denoted by l for large or s for small particles, three partial radial distribution functions may be calculated: $g_{ll}(r)$, $g_{ls}(r) = g_{sl}(r)$, and $g_{ss}(r)$.

Structure factors are also calculated directly from particle positions using the expression for $S(\mathbf{k})$ from Equation (2.33), which is now written as

$$S(\mathbf{k}) = \frac{1}{N}\left\langle \sum_{i=1}^{N}\sum_{j=1}^{N}\cos(\mathbf{k}\cdot\mathbf{r}_i)\cos(\mathbf{k}\cdot\mathbf{r}_j)\right\rangle + \frac{1}{N}\left\langle \sum_{i=1}^{N}\sum_{j=1}^{N}\sin(\mathbf{k}\cdot\mathbf{r}_i)\sin(\mathbf{k}\cdot\mathbf{r}_j)\right\rangle, \tag{3.2}$$

where $\mathbf{r}_i$ is the position of particle i and $\mathbf{k}$ is the wavevector. As $\mathbf{k}$ is an inverse lengthscale, the magnitude of $\mathbf{k}$ has a minimum value for $k = |\mathbf{k}| = 2\pi/L$, where L is the size of the system as a whole. This minimum value sets the spacing between the vectors in $k-$space such that, in 2D,

$$\mathbf{k} = \frac{2\pi}{L}(n_x\hat{\mathbf{x}} + n_y\hat{\mathbf{y}}) \tag{3.3}$$

where n_x and n_y are integers and $\hat{\mathbf{x}}$ and $\hat{\mathbf{y}}$ are unit vectors in the x and y directions. From geometical considerations, it can be seen that the number of wavevectors that are of equal or similar magnitude increases with increasing k. This greatly improves statistics but also results in a very large number of wavevectors for large values of k. As such, as k increases it is necessary to reduce the sampling of $k-$space to improve the speed of the calculation. Importantly, this is carried out by the removal of equal magnitude bands of wavevectors rather than by simply increasing the spacing between wavevectors. Finally, as the system is isotropic, an azimuthal

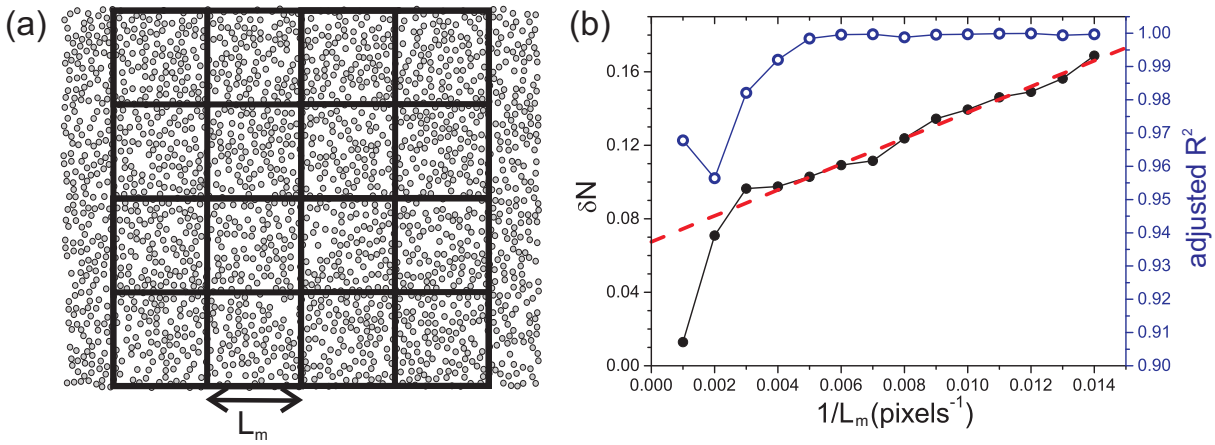

Figure 3.1: (a) An illustration of the gridding used for the sub-box analysis for $m = 4$. (b) An example of the box size-analysis plots used to extrapolate to infinite system size. Here, the filled symbols show δN (computed from Equation (3.5)) as a function of box length L_m for one area fraction and the open symbols indicate the quality of the Gaussian fit as quantified by the adjusted R^2. The dashed line shows the linear fit to the data for $1/L_m > 0.004$ used for the extrapolation.

average over wavevectors of equal magnitude is performed and as such experimental structure factors are discussed in terms of $k = |\mathbf{k}|$.

3.2.3 The limit $S(k \to 0)$ and number fluctuations

An estimate of the limit of $S(k)$ as $k \to 0$ may be obtained either by an extrapolation with a suitable function or by an analysis of number fluctuations within the system (as discussed in Section 2.1.1). In the case of the former, an even order polynomial fit of the form

$$S(k) = a + bk^2 + ck^4 + ..., \tag{3.4}$$

is applied to the data at small k, with a, b and c constants determined from the fits.

To determine the limit $S(k \to 0)$ by a consideration of the number fluctuations a sub-box analysis is performed [131,132], whereby the fluctuations in particle number, δN, in a box with a well defined lengthscale, L_m, are computed according to

$$\delta N = \frac{\langle N^2 \rangle - \langle N \rangle^2}{\langle N \rangle}. \tag{3.5}$$

These number fluctuations depend strongly on the box size under consideration, with the size of

the fluctuations relative to the number of particles present increasing as the box size decreases. In order to determine the expression in the thermodynamic limit, i.e. for an infinite system, number fluctuations are computed as a function of box length for multiple box sizes and subsequently δN is extrapolated to infinite box length to determine $S(k) \to 0$. For the experimental images with a frame size of 1280×1024 pixels, a square box with $L = 1000$ pixels positioned in the centre of the frame defines the maximum lengthscale. To have a well defined length for the smaller boxes, the frame is split into an $m \times m$ grid of squares where m runs from 1 to 14. The lengths of the sides of each square are therefore $L_m = 1000/m$ pixels and an example of this is shown in Figure 3.1a. As a result, the number of boxes considered increases with decreasing boxsize. As such, statistics are significantly better for the smaller box sizes providing that the density of the system is sufficiently high to result in a significant number of particles in each box. While the number fluctuations for each concentration and box length are calculated over $500 - 700$ frames, to ensure that sufficient statistics are achieved for each box size the resulting particle number distributions are compared to the expected Gaussian form of the distribution. Only results with sufficiently Gaussian number distributions (as quantified by the adjusted R^2 of the fit) are used for the extrapolation (see Figure 3.1b).

3.2.4 Structure factors in binary systems

As with the radial distribution functions, three partial static structure factors, $S_{ij}(k)$, can be defined for a binary system: $S_{ll}(k)$, $S_{ls}(k) = S_{sl}(k)$ and $S_{ss}(k)$. These relate to correlations between the individual species, and are calculated as

$$S_{ij}(\mathbf{k}) = \frac{1}{N}\left\langle \sum_{\nu=1}^{N_i}\sum_{\mu=1}^{N_j} \cos(\mathbf{k}\cdot\mathbf{r}_\nu)\cos(\mathbf{k}\cdot\mathbf{r}_\mu)\right\rangle + \frac{1}{N}\left\langle \sum_{\nu=1}^{N_i}\sum_{\mu=1}^{N_j} \sin(\mathbf{k}\cdot\mathbf{r}_\nu)\sin(\mathbf{k}\cdot\mathbf{r}_\mu)\right\rangle, \quad (3.6)$$

where $\mathbf{r}_{\nu,\mu}$ is the position of particle ν of species i or μ of species j, and $\mathbf{k}$ is the wavevector. Additionally, there are three important linear combinations of the partial structure factors, known as the Bhatia-Thornton structure factors [133], which are defined as

$$S_{nn} = S_{ll} + S_{ss} + 2S_{ls}, \quad (3.7)$$

$$S_{cc} = c_s^2 S_{ll} + c_l^2 S_{ss} - 2c_l c_s S_{ls} \quad (3.8)$$

$$S_{nc} = c_l S_{ss} - c_s S_{ll} + (c_l - c_s)S_{ls}. \quad (3.9)$$

Here, c_i is the concentration of component i, defined as $c_i = N_i/N$ $(i = l, s)$ where N_i is the number of large or small particles. Here, n and c as subscripts denote number and concentration, with the three linear combinations providing information on correlations in number and concentration of the two species.

3.3 Results and discussion

3.3.1 Structure in monodisperse systems

First, the equilibrium structure of one-component systems consisting of $\sigma = 2.79$ µm or of $\sigma = 4.04$ µm particles is considered, which corresponds to the lines $q = 0$ and $q = 1$ of Figure 2.2a. Examples of the radial distribution functions and static structure factors for these systems are shown in Figure 3.2. Figure 3.2a and c show $g(r)$ for various total packing fractions as a function of the distance scaled by the particle diameter. The radial distribution functions show an initial sharp peak at $r = \sigma$ followed by a decay in peak height which tends to unity at large r. As the total area fraction increases, both the number and height of peaks increases, consistent with increasing structural order. Even at the highest density considered, no significant evidence of a splitting of the second peak is seen, which would be an indication of hexagonal crystalline order [134]. The same behaviour is seen for both the monodisperse systems with $\sigma = 2.79$ µm and $\sigma = 4.04$ µm.

Colloidal suspensions are considered to be excellent model hard sphere systems, and to test this assumption with respect to structural measures, the radial distribution functions of the quasi-2D monodisperse systems are compared to results for hard disk systems from both fundamental measure theory (FMT) [135–137] and Monte Carlo simulations [138]. Examples of this comparison for the system with $\sigma = 2.79$ µm with MC simulations and for the system with $\sigma = 4.04$ µm with FMT are shown in Figure 3.2a and c respectively. The experimental data and predictions both from FMT and the MC simulation are in excellent agreement, in particular with respect to the contact value, the wavelength of oscillation and the decay length. The same quantitative agreement is seen for all area fractions for both the 2.79 µm and 4.04 µm systems. Importantly, the only input parameter used is the area fraction, which not only confirms the experimental values of particle diameter and packing fractions, but also shows that the colloidal

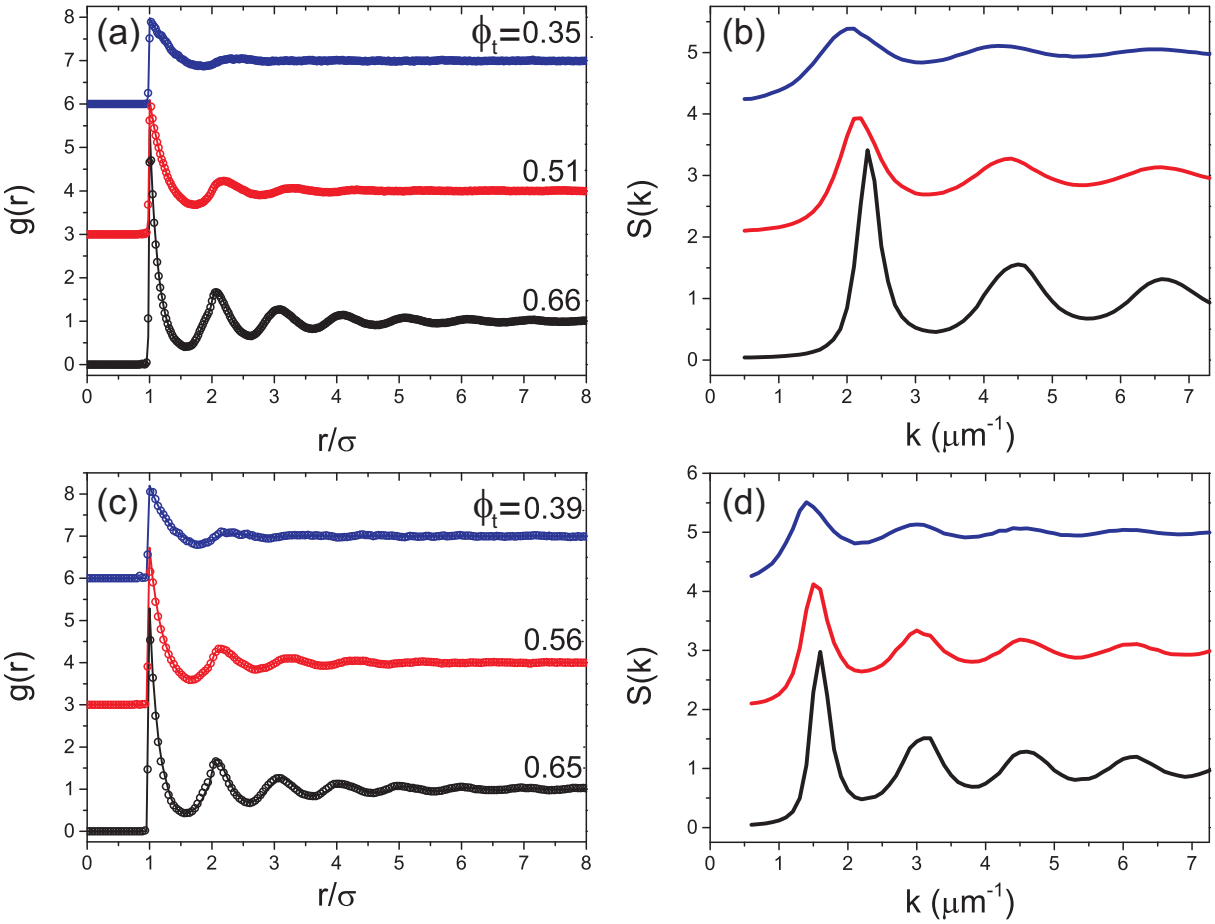

Figure 3.2: The radial distribution function, $g(r)$, and the corresponding static structure factors, $S(k)$, for monodisperse systems with the results for $g(r)$ from FMT and Monte Carlo simulation. (a) and (b) show $g(r)$ and $S(k)$ for the $\sigma = 2.79$ μm system at three values of total area fraction, ϕ_t as indicated in (a). Here, the experimental $g(r)$ (symbols) are compared to the results from MC simulation for hard disks (lines). The $g(r)$ for $\phi_t = 0.51$ and 0.35 are shifted upwards by three and six units respectively. (c) and (d) show the equivalent plots for the $\sigma = 4.04$ μm system at area fractions as indicated in (c). Experimental $g(r)$ (symbols) are now compared with results from FMT (lines).

system is an almost perfect model system for hard disks.

The structure factors that correspond to the radial distribution functions shown in Figure 3.2a and c are shown in Figure 3.2b and d. Here, the first peak relates to structure on the lengthscale of a particle diameter, σ, with subsequent peaks in $S(k)$ related to real space distances smaller than σ. Structure at $k < 2\pi/\sigma$, reflects real space structure which exists over a distance of many particle diameters, with the $k \to 0$ limit providing information about the system in the thermodynamic limit. In both systems, the same behaviour is seen with increasing ϕ_t, with $S(k)$ exhibiting a greater degree of structure and a lower $k \to 0$ limit, consistent with the greater pressure in the system as ϕ_t increases. This exemplifies a strength of the static

structure factor with respect to the radial distribution function, as an accurate extrapolation of the $S(k)$ for low k gives an indication of behaviour on much larger lengthscales.

3.3.2 Links to the equation of state

A key importance of the two-point correlation functions is that under certain assumptions they may be used to directly calculate thermodynamic properties, as discussed in Chapter 2. Perhaps one of the most important of these is the equation of state for the system, which may be calculated from the contact value of the radial distribution function, $g(\sigma)$ (Section 2.1.3), as

$$\frac{\beta P}{\rho} = 1 + 2\phi g(\sigma) \tag{3.10}$$

for hard disks. The equation of state can also be found from the $k \to 0$ limit of $S(k)$ (Section 2.1.1), as

$$S(k \to 0) = \rho k_{\mathrm{B}} T \chi_T, \tag{3.11}$$

with χ_t the isothermal compressibility. While both the $k \to 0$ limit of $S(k)$ and the contact values of $g(r)$ have well-defined values, the experimental determination of the relevant functions with sufficient accuracy to be used quantitatively is more challenging.

Experimental determination of the contact value

Difficulties concerning the experimental determination of the contact value, $g(r = \sigma)$, arise due to the fact that $g(r)$ is a histogram and so must be calculated with a finite bin size. This results in a measured $g(r)$ that is the convolution of the 'true' $g(r)$ for the system with the bin size used in the measurement. As a result, the first peak is shifted to a slightly larger distance and the height of the first peak, g_1, is smaller than the 'true' contact value. The height of the first peak also depends on the size [139] and the positioning of the bins. The first of these follows directly from the fact that an integral over the first peak must equal the number of nearest neighbours, and as such, if the bins used are smaller, the height of this peak must be larger. The second arises because even for dense systems there will be some fluctuation in the measured distance to the first coordination shell of particles, and if the bins are positioned in such a way that this

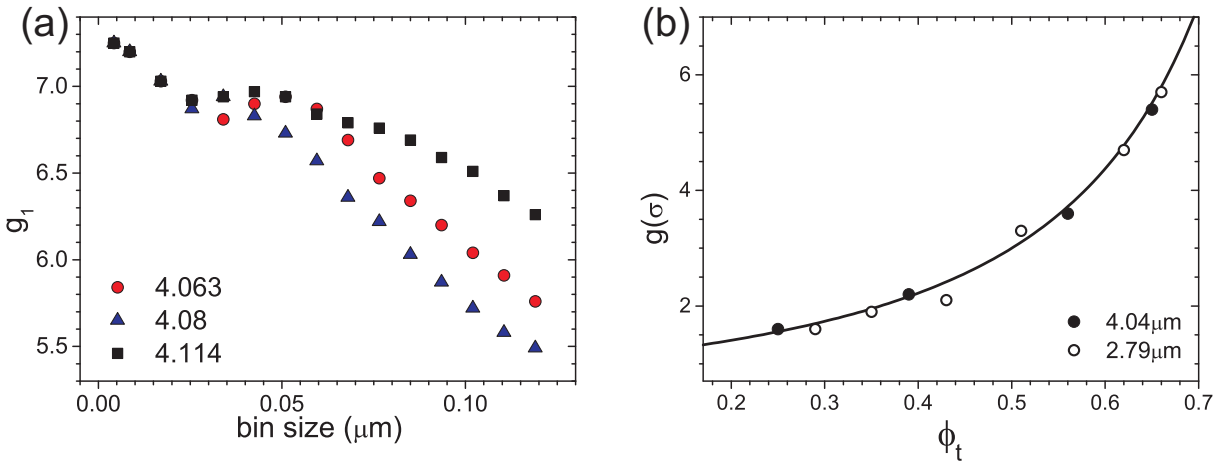

Figure 3.3: (a) The variation in the value of g_1 with bin size and centering position for a monodisperse system with $\sigma = 4.04$ μm and (b) the variation in the contact value with ϕ_t for both monodisperse systems (filled and open symbols) with the prediction from scaled particle theory (Equation (3.13)).

first shell of particles is split between a greater number of bins the overall height of the peak will be less.

This behaviour is shown in Figure 3.3a, where we plot g_1 as a function of the bin size for three centering positions of the bins. As expected g_1 decreases with increasing bin size, but is relatively independent of both the bin size and the centering position of the bins for bin sizes in the range of $0.02 - 0.05$ μm. The distribution functions are therefore computed using a binsize of 0.0425 μm, which is chosen to be at the upper end of this range to optimise statistics. The contact value is subsequently calculated by fitting the decay of the first peak with an exponential function and extrapolating back to the hard disk diameter [139–143]. Various theoretical expressions for the contact value as a function of ϕ_t have been postulated, but the FMT with which our results are compared predicts that for the monodisperse system the variation in the contact value should follow that predicted by scaled particle theory [144]. In this theory

$$\frac{\beta P}{\rho} = \frac{1}{(1-\phi_t)^2} \tag{3.12}$$

and this may be combined with Equation (3.10) to find an expression for the contact value as

$$g(\sigma) = \frac{2-\phi_t}{2(1-\phi_t)^2}. \tag{3.13}$$

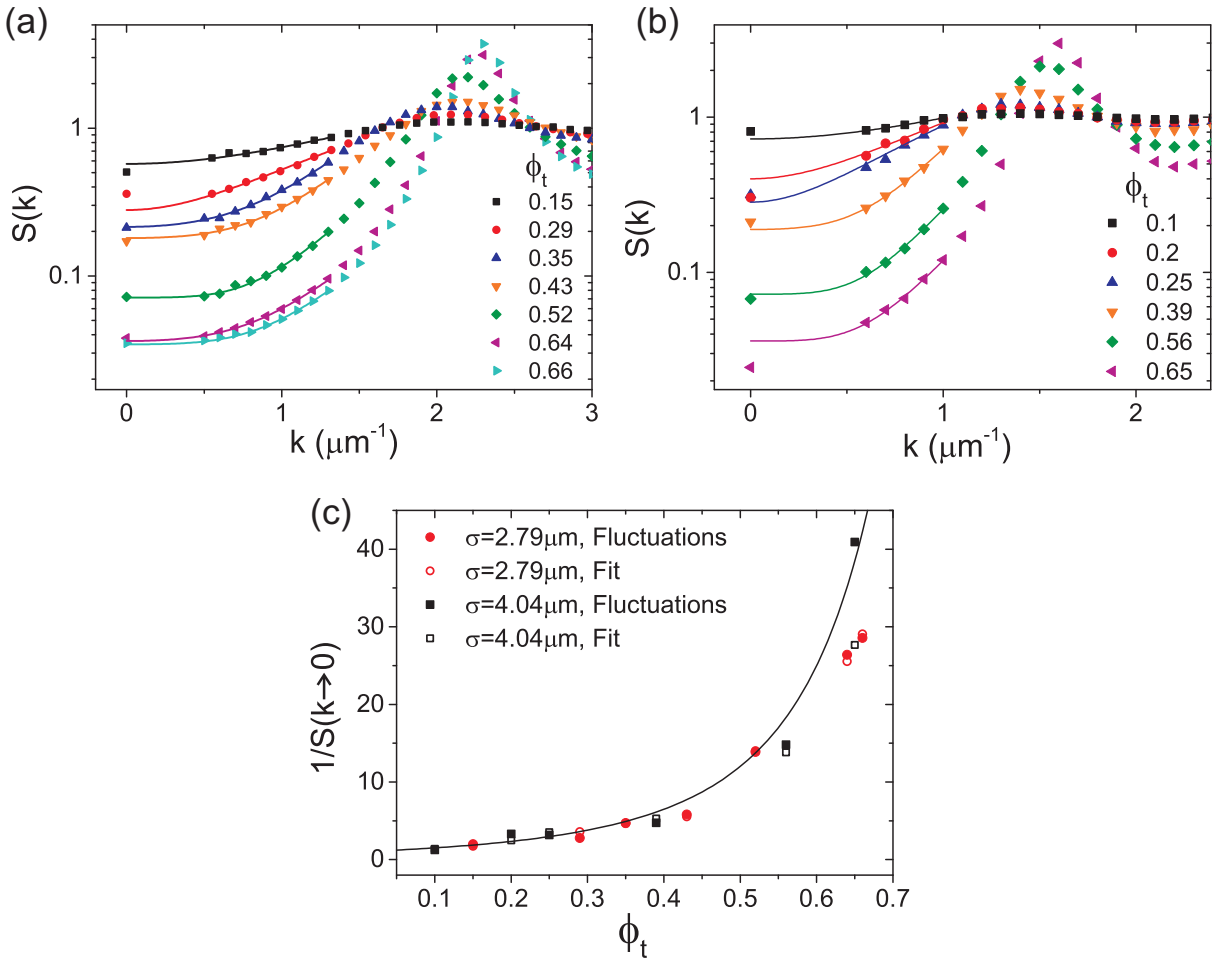

Figure 3.4: The small k limit of the structure factor for monodisperse (a) $\sigma = 2.79$ μm and (b) $\sigma = 4.04$ μm particle systems. Values at $k = 0$ are those determined by an analysis of fluctuations. Lines show a fit of the form $S(k) = a + bk^2 + ck^4 + ...$ (Equation (3.4)). (c) A comparison of the theoretical expression for the $k \to 0$ limit of $S(k)$ (Equation (3.16) shown as a solid line) with the experimentally determined limit from an analysis of fluctuations (filled symbols) and the fit as described in Equation (3.4) (open symbols) for the two monodisperse systems.

Our experimentally determined values are compared with this theory in Figure 3.3b and excellent agreement is found.

The limit of $S(k)$ as determined from both the extrapolation and the result of the fluctuation analysis are shown in Figure 3.4a and b with the original static structure factors. For most systems, reasonable agreement is seen between the apparent limit of the measured $S(k)$, the limit calculated from number fluctuations and the extrapolation. The limit of $S(k \to 0)$ is connected to the equation of state for the system via the isothermal compressibility, which is

found by combining Equations (3.11) and (2.12) to find

$$S(k \to 0) = k_{\mathrm{B}}T \left(\frac{\partial \rho}{\partial P} \right)_T , \tag{3.14}$$

which implies

$$\frac{1}{S(k \to 0)} = \beta \left(\frac{\partial P}{\partial \rho} \right)_T . \tag{3.15}$$

If the equation of state is again that determined from scaled particle theory (Equation (3.12)), it follows that

$$\beta \left(\frac{\partial P}{\partial \rho} \right)_T = \frac{1+\phi}{(1-\phi)^3} \quad \Longrightarrow \quad S(k \to 0) = \frac{(1-\phi)^3}{1+\phi}. \tag{3.16}$$

In Figure 3.4c the prediction from Equation (3.16) is shown with the experimental values of $1/S(k \to 0)$ calculated using both the extrapolation and the analysis of number fluctuations. Good agreement is found between the equation of state and the experimental estimation at low area fractions, but this deteriorates at higher area fractions. This may be due to insufficient statistics for the higher area fractions, where a greater length of time is required for the system to sample enough different configurations to fully capture the fluctuations.

3.3.3 Structure in binary systems

The structure of a range of quasi-2D binary systems is now considered at two different size ratios: a small size ratio system of $\sigma = 2.79$ μm and $\sigma = 4.04$ μm particles, with $\gamma = \sigma_l/\sigma_s = 1.45$, and a large size ratio system of $\sigma = 2.79$ μm and $\sigma = 6.10$ μm particles, with $\gamma = 2.19$. To describe these systems fully, another parameter is defined that arises from the geometry of the system. As the gravitational height of the particles used is very small relative to the particle diameter (see Section 2.3.1), the centres of particles of different sizes do not lie in the same plane when sedimented as illustrated in Figure 3.5. This introduces a nonadditivity into the system, where the nonadditivity, Δ, is described by the equation

$$\sigma_{ls} = \frac{(\sigma_{ll} + \sigma_{ss})}{2}(1 + \Delta). \tag{3.17}$$

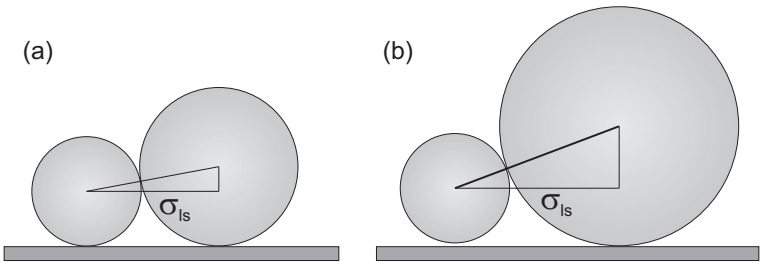

Figure 3.5: The in-plane structure of the binary systems demonstrating the nonadditivity for (a) the small size ratio ($\gamma = 1.45$) and (b) the large size ratio ($\gamma = 2.19$) systems.

The nonadditivity can have a profound effect upon the behaviour of the system due to its implications for the free volume. For positive nonadditive systems with $\Delta > 0$, the overall free volume in the system is increased if there are more contacts between like particles, leading to phase separation, whereas for negative nonadditive systems, the opposite effect will promote ordering to minimise like particle contacts. While the two size ratios considered do not differ significantly, there is a much greater variation in the nonadditivity, with $\Delta = -0.019$ for the small size ratio and $\Delta = -0.07$ for the large size ratio system. In both cases, the negative sign of the nonadditivity indicates that the closest distance between unlike particles in the binary system is lower than the sum of their hard disk radii. One consequence of this nonadditivity is that it is difficult to calculate the total area fraction for the binary systems; while the number of each type of particles can be determined exactly from the images, the effective area for each particle depends upon the composition of its shell of nearest neighbours. For the small size ratio system, the diameter of the large particles in the plane of the small particle centres is not significantly different and hence this effect can be neglected. For the large size ratio system, this difference is larger, and here the diameter in the plane of the centres of the small particles is used for the calculation of the total area fraction (see Section 2.3.1).

3.3.4 Structure in binary monolayers at small size ratio

For the small size ratio system, the three partial radial distribution functions, g_{ll}, $g_{ls} = g_{sl}$ and g_{ss}, are first considered, and are shown in Figure 3.6a-c for systems with $\phi_t \approx 0.66$ and with values of $q = 0.37$, 0.50 and 0.71. These are calculated in the same manner as those for the monodisperse system, only differing in that there is now a distinction between the two particle

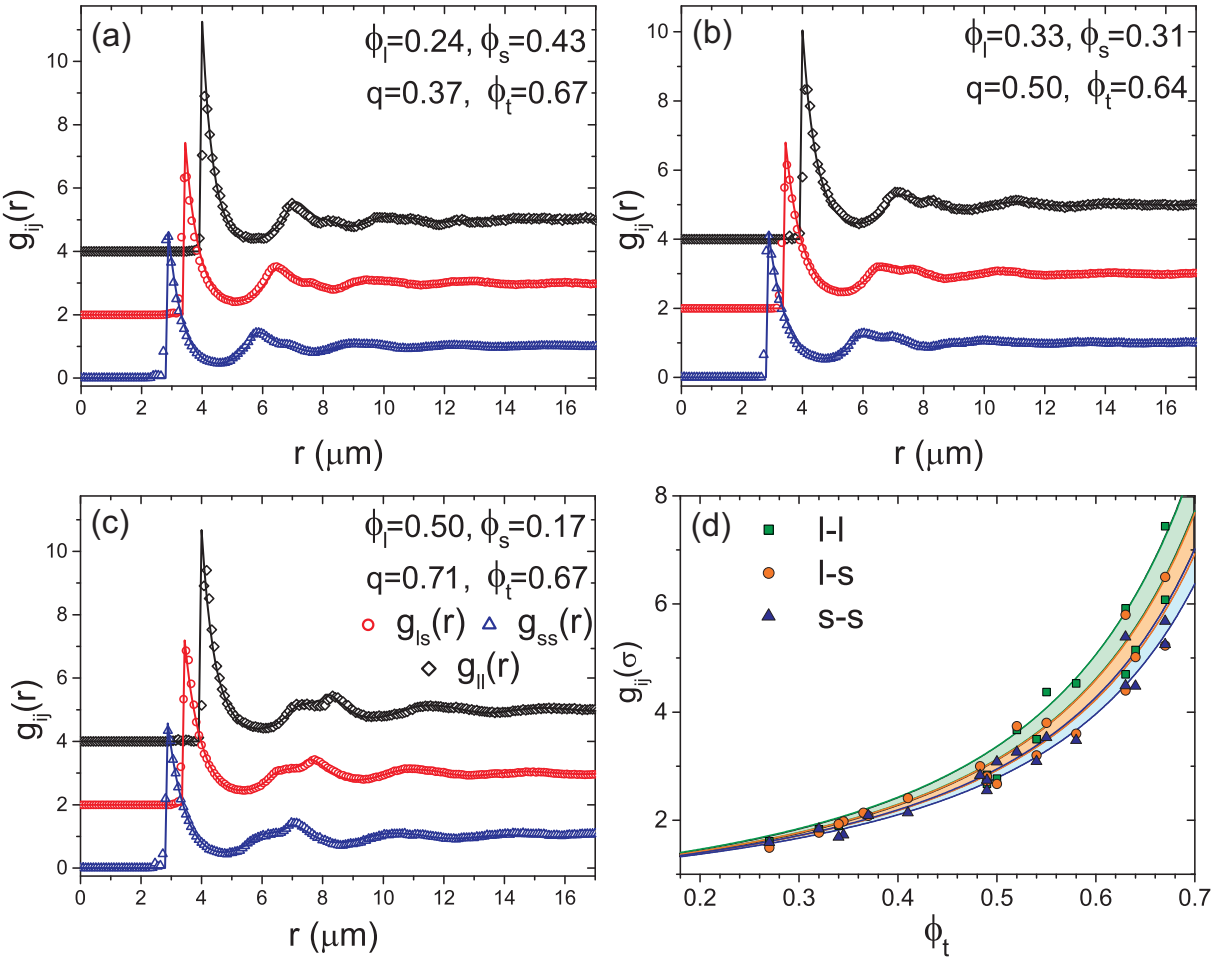

Figure 3.6: (a)-(c) Experimental partial radial distribution functions, $g_{ij}(r)$ for three binary systems at size ratio $\gamma = 1.45$ (symbols) with FMT results for hard disk mixtures (lines). Specific values of ϕ_l, ϕ_s, ϕ_t and q are specified in the plots. $g_{ls}(r)$ and $g_{ll}(r)$ are shifted upwards by two and four units respectively. (d) The contact values of the three partial $g_{ij}(r)$ for the binary systems at all studied compositions. Theory predicts a small composition dependence and the coloured regions denote the range of values for the considered compositions from $q = 0.17$ to $q = 0.71$.

species. It is clear from Figure 3.6a-c, however, that for the high values of ϕ_t considered, $g_{ij}(r)$ shows significantly less structure than in the monodisperse system, with both the number and heights of peaks reduced. This is due to the complex packing effects arising from the mixture of two species, which introduces new lengthscales into the correlation functions. For the small size ratio studied here, however, the diameters are too similar to see structural crossover [145–147].

The experimental radial distribution functions are again compared to results from FMT, this time for hard disk mixtures [78, 135, 136]. These are shown with the experimental data in Figure 3.6a-c. As for the monodisperse systems, the agreement between experiments and theory is excellent for all compositions, even at high values of the total packing fraction ϕ_t. For

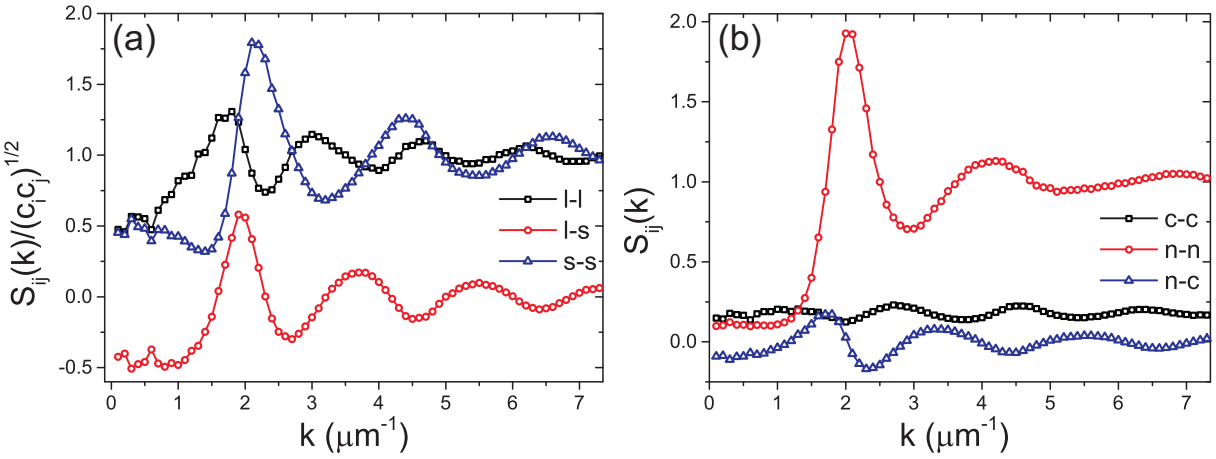

Figure 3.7: (a) The three partial structure factors for the small size ratio system at $\phi_t = 0.63$ and $q = 0.37$. For clarity, $S_{ij}(k)$ is scaled by $(c_i c_j)^{1/2}$. (b) The three linear combinations as described in Equations 3.7−3.9.

the binary mixtures it is necessary to include the size ratio as an additional parameter in the FMT calculation, and the correct value for this parameter is unclear due to the nonadditivity present in the system. An alternative size ratio of $\gamma = 1.41$ may be calculated by projecting the centres of the particles onto the base plane and in the FMT for additive mixtures a size ratio of 1.43, intermediate between this value and the true value of 1.45 is used for all systems. In principle the agreement between theory and experiment may be improved slightly by using $\gamma = 1.45$ (1.41) for systems rich in large (small) particles however the deviations from the results for $\gamma_{FMT} = 1.43$ are small. Importantly, this indicates that at this size ratio the nonadditivity present has a negligible effect on the structure, with the experimental system behaving as a hard disk mixture. The contact values for the three partial radial distribution functions are calculated in the same manner as those for the monodisperse systems and are shown in Figure 3.6d for all studied compositions ($q = 0.17, 0.37, 0.5$ and 0.71). For the binary system, FMT does not give a closed expression for the variation of the contact values of $g_{ij}(r)$ with ϕ_t and previous simulation results [148, 149] have not agreed well with scaled particle theory for binary mixtures [150]. Consequently, our data is instead compared to the prediction of Santos et al. [151], which agrees well with simulation data [149]. This prediction is also shown in Figure 3.6d, where the weak composition dependence of $g_{ij}(\sigma_{ij})$ predicted by Santos is represented as a coloured region with a width accounting for the q dependence. Overall, reasonable agreement is seen with the theoretical prediction, although the composition dependence is too mild to determine the extent to which the contact values conform to this prediction.

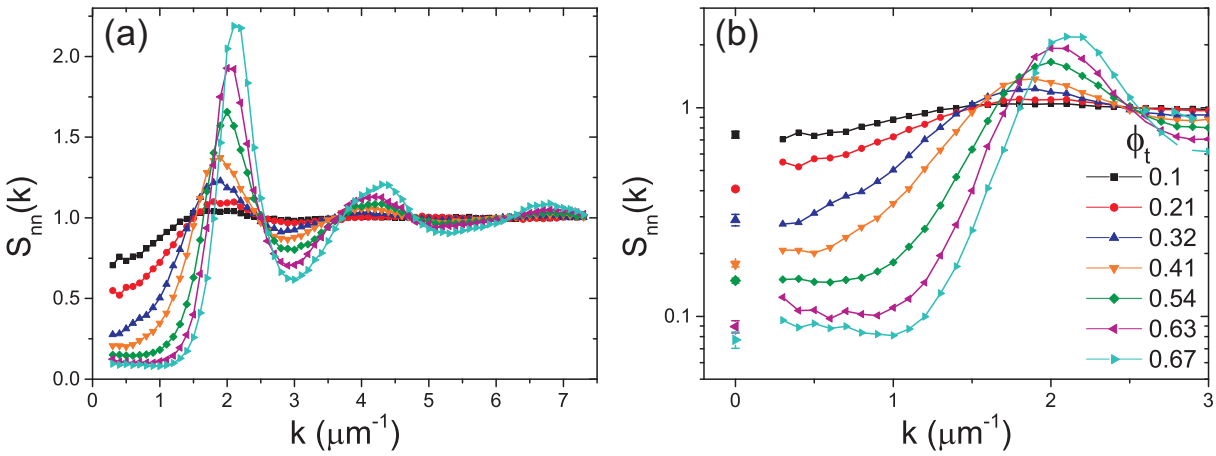

Figure 3.8: (a) The number-number structure factor, $S_{nn}(k)$, for the small size ratio mixture at $q = 0.37$ and at a variety of total area fractions. (b) The small k region of $S_{nn}(k)$ with the $k \to 0$ limit from an analysis of the number fluctuations.

The partial static structure factors, $S_{ij}(k)$, are now considered, which display more complex behaviour. The normalisation is now such that $S_{ll}(k)$ and $S_{ss}(k)$ tend towards the number concentration, $c_i = N_i/N$ of large and small particles respectively and $S_{ls}(k)$, which considers the cross correlations, tends to 0 for large k. An example of the three partial structure factors for the system at $q = 0.37$ and $\phi_t = 0.63$ are shown in Figure 3.7a, with all three functions scaled by $(c_i c_j)^{1/2}$ so that the peaks in the minority component are easily distinguished.

In Section 3.2.2, three important linear combinations of these structure factors were introduced and these are shown for the same area fraction in Figure 3.7b. Here, $S_{nn}(k)$ considers the number fluctuations in the system and is similar to $S(k)$ for the monodisperse systems, with the function tending to unity for large k and to a value related to the number fluctuations of all particles as $k \to 0$. Unlike $S(k)$, however, this limit no longer relates directly to the isothermal compressibility. $S_{cc}(k)$ considers concentration fluctuations and tends at large k to the product of the concentrations of the two species, $c_l c_s$. The final linear combination $S_{nc}(k)$ considers correlations between number and concentration. As for the monodisperse systems, a fluctuation analysis may be used to determine the $k \to 0$ limit of the calculated static structure factors. Here the focus is placed upon the calculation of the limit of $S_{nn}(k)$ from a consideration of number fluctuations, which involves following the same procedure as described for the monodisperse systems (see Section 3.2.2). Importantly, no distinction is made between the particle species. In Figure 3.8a we show the variation of $S_{nn}(k)$ with ϕ_t for the small size ratio system at $q = 0.37$, in which the similarity between $S_{nn}(k)$ and $S(k)$ for the monodisperse system in Figure 3.2 is

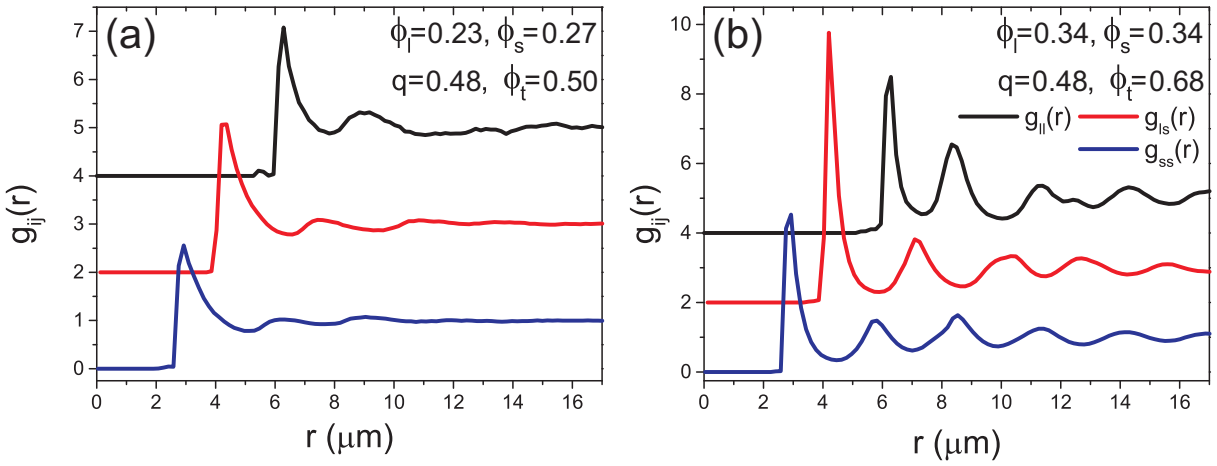

Figure 3.9: The partial radial distribution functions, $g_{ij}(r)$, of the large size ratio binary system at $q = 0.48$ and; (a) $\phi_t = 0.50$, (b) $\phi_t = 0.68$. Specific values of ϕ_l, ϕ_s and ϕ_t are specified in the plots. $g_{ls}(r)$ and $g_{ll}(r)$ are shifted upwards by two and four units respectively.

clear. Figure 3.8b highlights behaviour of the function at small k, where it can be seen that the fluctuation analysis again provides a good estimate of the limit as $k \to 0$. While for $S_{nn}(k)$ this does not allow for the calculation of additional thermodynamic properties, it demonstrates that the method of calculating the $k \to 0$ limit of the structure factors by a fluctuation analysis is also applicable to the binary systems. This is of significance, as for $S_{cc}(k)$, the $k \to 0$ limit is related to the thermodynamic factor of the system, defined as [152]

$$\Phi = \frac{c_l c_s}{S_{cc}(k \to 0)}. \tag{3.18}$$

This quantity is of central importance in the calculation of the interdiffusive properties of the system, and consequently, its application is discussed further in Chapter 6.

3.3.5 Structure in binary monolayers at large size ratio

The same structural analysis is now performed for the system at large size ratio with $\gamma = 2.19$. The comparison between theory and experiment presented in the previous section demonstrates that for the small size ratio system, the behaviour is that of an almost perfect additive hard disk mixture. This is in spite of the small nonadditivity present. For the larger size ratio system, however, the nonadditivity is around four times greater, despite the modest increase in absolute size ratio, and very different structural effects are seen.

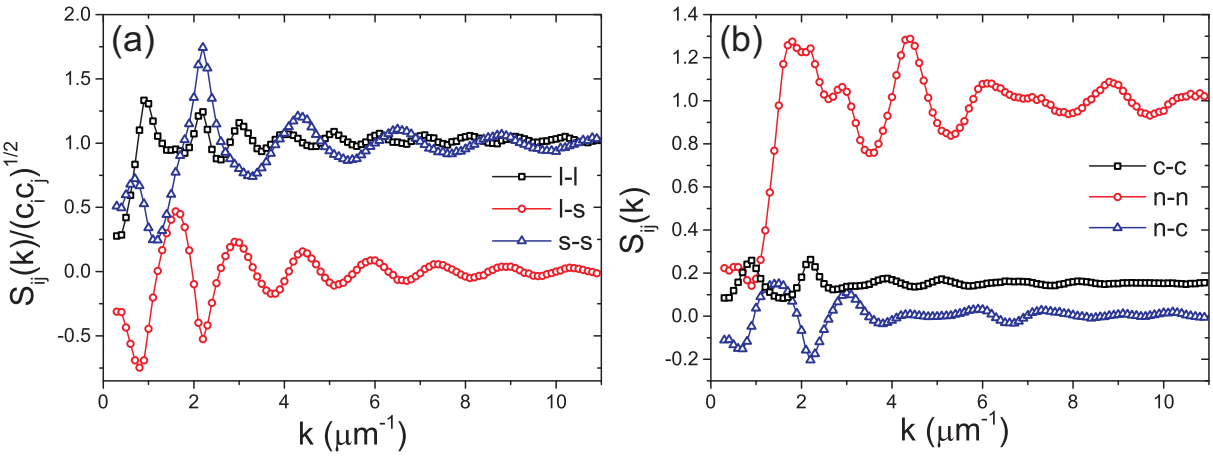

Figure 3.10: The three partial structure factors for the large size ratio system at (a) $\phi_t = 0.59$. (b) The three corresponding linear combinations as described by Equations 3.7−3.9.

The partial radial distribution functions for systems at two total area fractions and $q = 0.48$ are shown in Figure 3.9. These differ from $g_{ij}(r)$ for the small size ratio in a number of respects. Firstly, the relative heights of the peaks differ, showing significant enhancement of peaks related to cross correlations. For example, the contact value of $g_{ls}(r)$ is larger than that of both $g_{ss}(r)$ and $g_{ll}(r)$, and in addition to this, $g_{ll}(r)$ displays a prominent second peak, corresponding to a large-small-large arrangement of particles. Secondly, the range of the correlations at the higher value of ϕ_t is much longer than that seen for the systems at small size ratio (Figure 3.6). These changes suggest that for the large size ratio system there is a higher degree of structural order and that this is particularly associated with structure that favours a mixing of the two species. Here, the radial distribution functions are not compared with the predictions of FMT, as clearly the behaviour of the system is very different to that of an additive mixture.

Similarly, different behaviour is seen in the partial static structure factors and their linear combinations as shown in Figure 3.10. Compared to those at low size ratio, there is now a significant peak in $S_{ll}(k)$ which coincides with the first peak in $S_{ss}(k)$ and also a significant pre-peak is seen in $S_{ss}(k)$. The latter is an indication of significant structure within the system at lengthscales larger than the particle diameter. As expected from the behaviour of the partial static structure factors, S_{nn}, shows a far more complex arrangement of peaks (see Figure 3.11) and in contrast to the data for small size ratio (Figure 3.8), is quite unlike that seen for monodisperse systems (see Figure 3.2b and d). Nevertheless, the analysis of the number fluctuations for this system also gives a good approximation of the $S(k \to 0)$ limit as shown in Figure 3.11b. Here, the shape of S_{nn} as $k \to 0$ shows evidence of the prepeak seen in $S_{ss}(k)$ and as such the

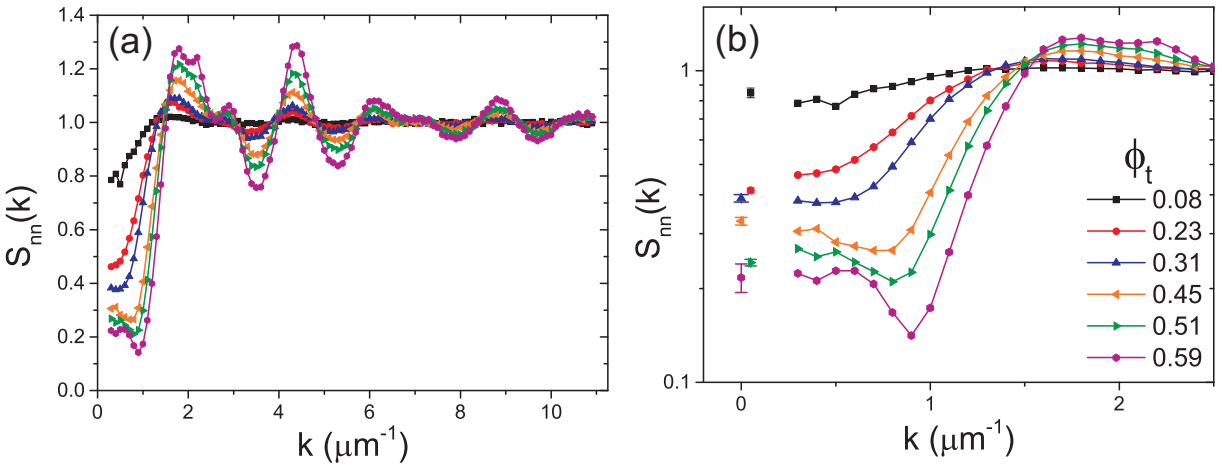

Figure 3.11: (a) The variation of the number-number structure factor, $S_{nn}(k)$, with ϕ_t for the large size ratio mixture. (b) The behaviour of $S_{nn}(k)$ with the $k \to 0$ limit from an analysis of the number fluctuations.

simple fitting used as a secondary estimation for the limit cannot be employed.

We believe the origins of these structural differences lie in the greater nonadditivity seen in the large size ratio system. For these binary mixtures, the effective size of the particles is substantially reduced if a structure is adopted in which the particles order such that there are mainly unlike particles adjacent to each other. This increases the free area, and as such is a more favourable configuration. This is the opposite phenomena to that seen in positive nonadditive mixtures, for example colloid-polymer mixtures, which instead are susceptible to phase separation into phases of high concentration of a single component.

3.4 Conclusions

In conclusion, we have presented a full structural analysis of quasi-two-dimensional monodisperse and binary systems at two different size ratios. Results from the monodisperse system for the radial distribution function show quantitative agreement with those from a Monte Carlo simulation and fundamental measure theory calculations, confirming the experimental area fractions and particle size and demonstrating that the system is an almost perfect experimental realisation of a hard disk system. The static structure factors for the monodisperse system are also calculated, and an analysis of number fluctuations used to estimate the limit of this function as $k \to 0$. Both this limit and the contact value of the radial distribution function are used to confirm the equation of state for the monodisperse system. The behaviour of the binary

systems considered depends sensitively on the size ratio via the nonadditivity of the system. Consequently, results from the small size ratio indicate that this system behaves as a hard disk additive mixture whereas the large size ratio system shows substantially different behaviour.

Acknowledgements

This work was performed in collaboration with Roland Roth, Jürgen Horbach, Simon Schnyder and Dirk Aarts. Thomas Skinner and Michael Juniper are thanked for useful discussions.

Chapter 4

Self-diffusion in quasi-two-dimensional binary colloidal fluids

ABSTRACT

In this Chapter, the dynamic behaviour of monodisperse and binary quasi-two-dimensional colloidal fluids at a range of compositions and area fractions is studied. In particular, the mean squared displacement is calculated and used to determine the short- and long-time self-diffusion coefficients. A comparison of the monodisperse system to a Monte Carlo simulation of hard disks demonstrates that, at long times, particles move according to simple Brownian dynamics and hence that the diffusion coefficient rescaled by the diffusion coefficient at infinite dilution is effectively not affected by hydrodynamic interactions. This contrasts with the behaviour of the short-time diffusion coefficient which clearly depends upon hydrodynamic interactions. As a result, simple theoretical expressions for the dependence of the rescaled long- and short-time self-diffusion coefficients upon the total area fraction are considered.

4.1 Introduction

Understanding the relationship between the structural and dynamic properties of fluids is a complex problem that is yet to be fully understood. This is in spite of vast attention from theory [82, 153–162] and simulation [76, 163, 164]. In recent years, there has been particular interest in elucidating this link for glasses, where structurally liquid-like systems show dramatically different dynamics [165, 166]. Part of the difficulty in addressing this problem experimentally is that it requires a system for which both the structure and dynamics may be probed in detail. As such, the ability to study the behaviour of colloidal fluids at a single particle level over convenient length and timescales make these attractive model systems.

The simplest transport property that may be used to characterise the dynamic behaviour of individual particles is self-diffusion. This is quantified by the self-diffusion coefficient, D, a property readily measured for colloidal systems in scattering and microscopy experiments [63, 65, 66, 84, 167–170]. Here, two diffusive regimes exist; a short-time regime, characterized by the short-time diffusion coefficient, D_S, and associated with the behaviour of particles interacting hydrodynamically but not directly, and a long-time regime, characterized by the long-time diffusion coefficient, D_L, which is only reached following many direct interactions.

This highlights a key difficulty in the description of colloidal dynamics, as both hydrodynamic interactions (HI) and direct interactions between large number of particles must be accounted for [154, 171, 172]. It also emphasises that the dynamic behaviour of colloidal systems is fundamentally different from that of molecular systems, which instead exhibit a short-time ballistic regime [99]. In spite of this, colloidal systems are still used to test theories developed to describe molecular liquids [66].

Numerous studies of dynamics in three-dimensional (3D) colloidal systems, both monodisperse [84, 169, 173–175] and bidisperse [167, 176–179], have been carried out using both scattering techniques and microscopy. For binary systems, which are of particular relevance to studies of the glass transition, significantly different behaviour is expected as the size ratio is varied [180, 181]. In quasi-two-dimensional systems, the emphasis has in general been upon short-time behaviour [55, 63, 182] and in addition to this, in much of the previous work the 2D systems have been highly confined, with the height of the cell comparable to the particle diame-

ter. As hydrodynamic interactions are expected to play an important role in self-diffusion, quite different behaviour may be seen in these systems compared to the system in this work, which has a much greater height and therefore volume of surrounding fluid.

In this Chapter, a systematic characterisation of the self-diffusion of colloidal particles in both monodisperse and bidisperse quasi-2D systems is presented. For the monodisperse systems, the diffusive behaviour at both short and long times is characterised. A comparison to Monte Carlo simulations is used to demonstrate that at long times, the particles behave as hard disks moving according to simple Brownian dynamics. As such, this shows that the ϕ_t dependence of the rescaled long-time diffusion coefficient, D_L/D_0 , is effectively not affected by hydrodynamic interactions. This differs from the behaviour at short-times which is clearly dependent upon HI. Based upon this, a theoretical ansatz based only upon structural quantities, i.e. without the inclusion of terms to describe hydrodynamic interactions, is used to account for the variation of the long-time diffusion coefficient with ϕ_t. The same analysis is performed for a binary system at a variety of compositions, where it is found that the data can be described by the same ansatz if a variable prefactor is used to account for packing effects.

4.2 Experimental techniques and data analysis

4.2.1 Colloidal model system

The quasi-two-dimensional colloidal system used is described in detail in Section 2.3.1. Here, the dynamic behaviour of monodisperse systems of particles, with diameters $\sigma = 2.79$ μm and $\sigma = 4.04$ μm, and of binary systems which are mixtures of these particles, with size ratio $\gamma = 1.45$, is considered. A quasi-2D system is realised by allowing the particles to sediment onto the base of a Hellma cell which has a height of 200 μm (approximately $50-70\ \sigma$). As such, while the colloidal system is structurally two-dimensional, the properties of the surrounding fluid are three-dimensional. For all systems, a wide range of total packing fractions, ϕ_t, are considered and for the binary system all four compositions, $q = \phi_l/\phi_t = 0.17$, 0.37, 0.5 and 0.71 are studied. Full details of the specific systems considered are shown in Figure 2.2a. Images are recorded at a rate of two frames per second for up to 45 minutes and particle coordinates are obtained as described in Sections 2.3.1 and 2.3.3. For the binary systems, particles are identified as either

large or small based upon the brightness of the features found, with the small and large particle subsets then tracked separately. A minimum track length is set in order to eliminate the small percentage of bright interstitials that are identified as particles but that persist only for a short time.

4.2.2 The mean squared displacement and diffusion coefficients

From the particle trajectories, we characterise the particle dynamics by calculating the mean squared displacement (MSD) as

$$\left\langle \delta r^2(t) \right\rangle = \frac{1}{N} \sum_{i=1}^{N} \left\langle \left[\mathbf{r}_i(t) - \mathbf{r}_i(0) \right]^2 \right\rangle , \tag{4.1}$$

with $\mathbf{r}_i$ the position of particle i, N the number of small or large particles and $\langle \dots \rangle$ the average over different time origins. The short- and long-time self-diffusion coefficients are defined as

$$D_S^{s,l} = \lim_{t \to 0} \frac{\left\langle \delta r^2(t) \right\rangle}{4t} \quad \text{and} \quad D_L^{s,l} = \lim_{t \to \infty} \frac{\left\langle \delta r^2(t) \right\rangle}{4t}. \tag{4.2}$$

Experimentally, these diffusion coefficients are determined from the slopes of the MSD at short and long times, respectively. Here, the notation is such that the superscript denotes the type of particle (i.e. small, s, or large, l) and the subscript the type of diffusion (i.e. S for short-time, L for long-time and 0 for infinite dilution). For each binary system studied four diffusion coefficients may therefore be calculated from the mean squared displacement; short-time diffusion for small particles (D_S^s), short-time diffusion for large particles (D_S^l), long-time diffusion for small particles (D_L^s) and long-time diffusion for large particles (D_L^l). The diffusion coefficient at infinite dilution, D_0, is estimated by an extrapolation of the measured short- and long-time diffusion coefficients at low ϕ_t to $\phi_t = 0$. An estimate of this quantity is obtained for all systems studied.

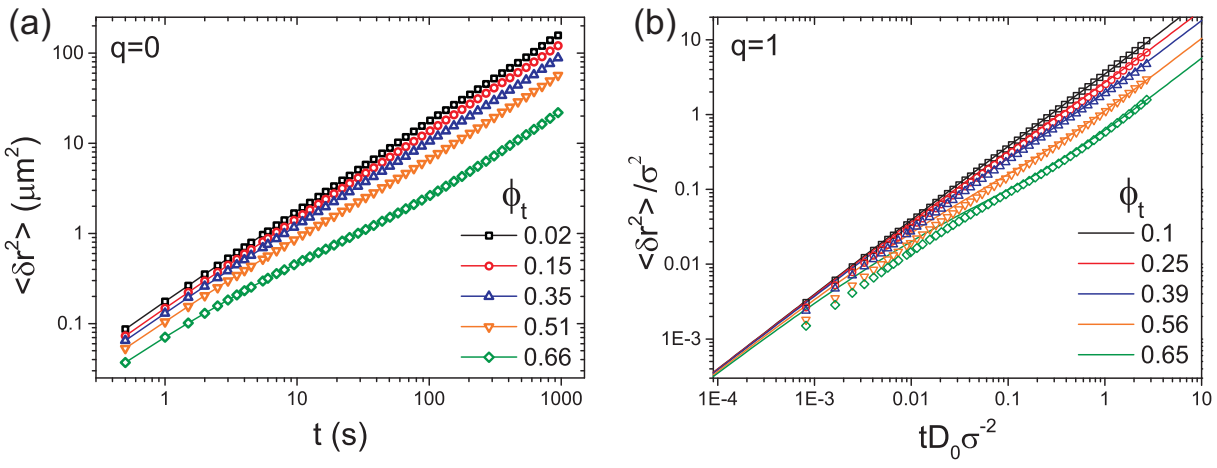

Figure 4.1: (a) The mean squared displacement of $\sigma = 2.79$ μm particles in a monodisperse system ($q = 0$) as a function of time at a range of ϕ_t. (b) The mean squared displacement in units of σ^2 from experiment (symbols) with the corresponding results from MC simulation (lines). The MSD is shown as a function of scaled time, tD_0/σ^2 for total area fractions $\phi_t = 0.1, 0.25, 0.39, 0.56$ and 0.65. Experimental data is from the monodisperse $\sigma = 4.04$ μm system ($q = 1$).

4.3 Results and discussion

4.3.1 Monodisperse system

First, the self-diffusion of the monodisperse small and large particle systems is considered. These are the two limiting cases for the binary mixtures considered later, and correspond to the lines $q = 0$ and $q = 1$ in Figure 2.2a. Plots of the mean squared displacement (MSD) for the $q = 0$ system is shown in Figure 4.1a for a range of total area fractions. In all cases, the MSD is linear at short and long times, indicative of diffusive behaviour. As such, short and long-time diffusion coefficients can be obtained from the initial and long-time slopes of the MSD as in Equation (4.2). At intermediate times the onset of a plateau is seen, which becomes more prominent as the total area fraction is increased. This non-linear behaviour is related to the period of time during which the particle has interacted directly with the surrounding particles, but is yet to interact with enough other particles to feel the rest of the system in an averaged way. This is consistent with the onset of caging and cage breaking behaviour at high ϕ_t [51,183]. Qualitatively, there is no difference in the behaviour seen for the $\sigma = 2.79$ μm and $\sigma = 4.04$ μm systems. Values of D_0 are calculated as described in Section 4.2.2 and are shown in Table 4.1 for all systems considered. The extrapolated values vary slightly, but are consistent with the value of D_0 as predicted by Equation (2.43) when the presence of the wall is accounted for by

Faxen's correction [184].

In Figure 4.1b the experimental mean squared displacements for the monodisperse particles with $\sigma = 4.04$ μm are compared to MSDs obtained from a Monte Carlo (MC) simulation of hard disks. While these simulations are usually employed for the study of equilibrium properties, this comparison of dynamics is valid as, under certain conditions, MC simulations have been shown to be equivalent to Brownian Dynamics simulations [79,185]. Here, in order to directly compare the simulation and experimental data, lengths are expressed in units of σ and time in units of σ^2/D_0.

In the short-time regime, the MSD of the simulation is independent of the area fraction whereas the experimental MSD clearly depends on ϕ_t. This ϕ_t dependence is also seen in the variation of the short-time diffusion coefficient, D_s, with ϕ_t as shown in Figure 4.2b for both monodisperse systems. Here, D_s can be well described by a linear expression of the form

$$\frac{D_s}{D_0} = 1 - \alpha\phi_t, \tag{4.3}$$

with α a constant to be determined. Values of α are found to be 0.87 ± 0.06 and 0.84 ± 0.04 for the $\sigma = 2.79$ μm and $\sigma = 4.04$ μm particle systems, respectively (see Table 4.1). Therefore, Equation (4.3) is shown in Figure 4.2b with an average value of $\alpha = 0.85$. There has been significant theoretical and experimental work considering expressions of the form of Equation (4.3) for 3D systems [153, 159, 168, 169, 174, 186, 187], where theoretical calculations suggest $\alpha = 1.83$. In 2D, the expected behaviour is less clear, however, it has been reported that α should be reduced relative to its value in 3D [62, 63, 121], consistent with our findings. Crucially, in all cases the variation of the short-time dynamics with ϕ_t is ascribed to hydrodynamic interactions between the particles and/or with other surfaces present such as the wall of the sample container. As the MC simulation is of a hard disk system with no solvent, there are clearly no HI, and so this difference between the experimental and simulation MSDs at short times is unsurprising.

In contrast to the short-time behaviour, Figure 4.1b shows that at long times the MSDs of the experiment – with solvent – and those of the simulation – without solvent – exhibit quantitative agreement. This is also evident from Figure 4.2a where the rescaled long-time self-diffusion coefficients, D_L/D_0, from both simulation and experiment are compared. These results indicate that hydrodynamic interactions are effectively absent with respect to the ϕ_t-

q	$D^s_{0,S}$	$D^s_{0,L}$	$D^l_{0,S}$	$D^l_{0,L}$	α_s	α_l	β_s	β_l
0.00	0.0438	0.0420	-	-	0.87±0.06	-	1.62± 0.06	-
0.17	0.0411	0.0363	0.0260	0.0249	0.69± 0.09	0.73± 0.10	1.35± 0.04	1.13± 0.06
0.37	0.0460	0.0420	0.0271	0.0251	0.75± 0.05	0.80± 0.04	1.32± 0.01	1.01± 0.02
0.50	0.0561	0.0478	0.0339	0.0274	0.91± 0.07	0.93± 0.07	1.71± 0.10	1.25± 0.07
0.71	0.0466	0.0405	0.0289	0.0250	0.85± 0.10	0.80± 0.08	1.17± 0.03	0.90± 0.04
1.00	-	-	0.0266	0.0267	-	0.84±0.04	-	1.73± 0.09

Table 4.1: Experimentally determined values of the self-diffusion coefficient at infinite dilution, $D_{0,S/L}$ ($\mu m^2\ s^{-1}$), calculated from both D_L and D_S. Also, experimental values of the parameters α (Equation (4.3)) and β (Equation (4.5)) for both small and large particles – indicated by the subscript s, l, respectively – across a range of values of q.

dependence of the long-time self-diffusion coefficient, i.e. that the reduction in the diffusion coefficient with increasing ϕ_t is that expected by the action of direct interactions alone. The underlying physical mechanism that leads to the agreement between simulation and experiment for D_L/D_0 is currently unclear. A simple interpretation, however, is that the single particle dynamics at long times are dominated by the direct hard interactions and thus do not reflect the strong dependence of the short-time diffusion coefficient on ϕ_t. This would be a surprising result, as it has been suggested that D_L can be expressed as [154, 160]

$$D_L = D_S f_{DI}(\phi_t), \tag{4.4}$$

where $f_{DI}(\phi_t)$ is a function that describes only the direct interactions, with the effect of HI on D_L assumed to be fully accounted for by D_S. In our system, the direct hard core interactions in the simulation and the experiment are identical, as confirmed by the excellent agreement between the simulated and experimental $g(r)$ shown in Figure 3.2. This implies that $f_{DI}(\phi_t)$ is identical for the simulation and the experiment. Hence, the quantitative agreement between simulation and experiment for D_L/D_0 and disagreement for D_S, indicates that Equation (4.4) does not hold for our system.

An alternative explanation of this result is that hydrodynamic interactions are in fact contributing to the long-time diffusive behaviour, but in a more complex manner than suggested by Equation (4.4). For this to be the case, the observed agreement requires that there is an extra multiplicative term in Equation (4.4) to account for the HI at long times that, importantly, must exactly cancel with D_S/D_0 for all area fractions. In 3D, studies on hard sphere systems have shown that HI have a small, but measurable, effect on the long-time self-diffusion coefficient

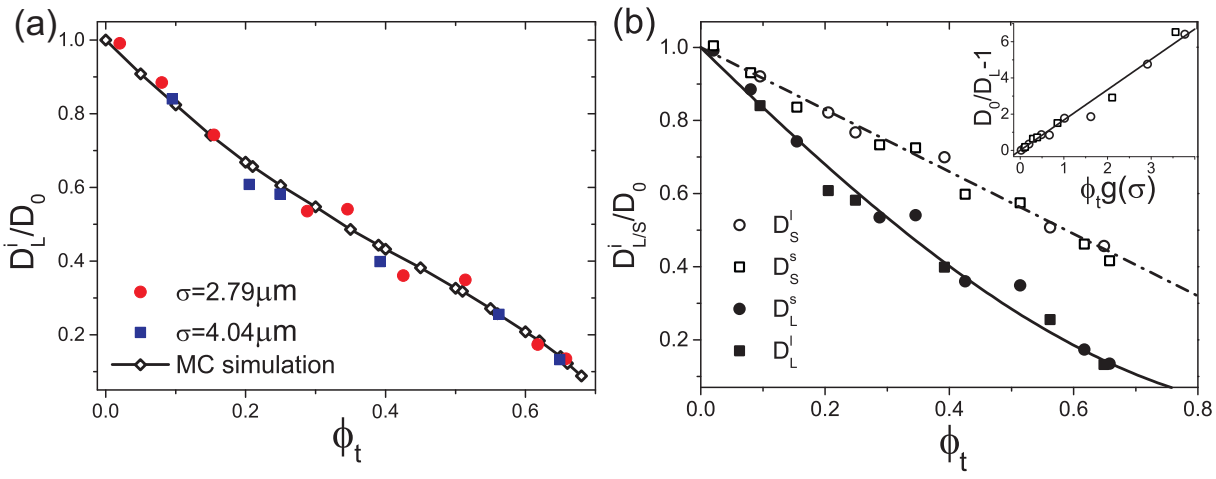

Figure 4.2: (a) A comparison of the experimental long-time self-diffusion coefficient for the monodisperse systems with that calculated from MC simulations. (b) Short- and long-time self-diffusion coefficients for the monodisperse small and large particle systems, scaled by D_0 (see Table 4.1). The dashed line shows the prediction for the short-time self-diffusion coefficient from Equation (4.3) with $\alpha = 0.85$ and the solid line the prediction from Equation (4.5) with $\beta = 1.675$. Inset is the linear fit from Equation (4.6) used to compute the value of β.

[84,188,189]. Here, while a full understanding of the mechanism is also lacking, there is evidence that Equation (4.4) does not describe the data well. If it is the case that the long-time self-diffusive behaviour involves a complex cancellation of hydrodynamic effects, the better agreement observed in our quasi-2D system suggests that the geometry of the system may be of importance.

Now, the ability to describe our data using a simple theoretical expression for D_L as a function of ϕ_t is considered. In light of the comparison to simulation, this expression only describes the effect of direct interactions upon the diffusion coefficient. These interactions will depend significantly on the structure of the system and this structural dependence has been described by an expression of the form [154, 162]

$$D_{\mathrm{L}} = \frac{D_0}{1 + \beta\phi_t g(\sigma)}, \tag{4.5}$$

where $g(\sigma)$ is the contact value of the radial distribution function and β is a constant to be determined. For 3D systems, the value of β is found to be two, in agreement with calculations for the linear expression appropriate at low ϕ_t [161,190]. A similar analysis in 2D suggests that the same expression may be used with $\beta = 2$ [191], again in agreement with the expression for the low ϕ_t behaviour [190]. It is seen, however, that the expression fails for higher area fractions and mode-coupling terms are required to describe the behaviour [191]. To test the applicability

of a purely structural expression of the form of Equation (4.5) to describe the behaviour of the long-time diffusion coefficient over the entire range of ϕ_t, the relationship

$$\frac{D_0}{D_L} - 1 = \beta\phi_t g(\sigma) \tag{4.6}$$

is used as a fit to the experimental data, with β as a fitting parameter. Following from the results in Section 3.3.2, $g(\sigma)$ is taken to be the scaled particle theory expression for the contact value (Equation (3.13)) [144]. The resultant linear fits produce values of $\beta = 1.62 \pm 0.06$ for the $\sigma = 2.79$ μm system and $\beta = 1.73 \pm 0.09$ for the $\sigma = 4.04$ μm system (Table 4.1). A comparison of the experimental data to Equation (4.6) with an averaged value of $\beta = 1.675$ is shown in the inset of Figure 4.2b, where linear behaviour is seen across the whole range of area fractions. Although we find the general form of the expression to describe our data well, the value of β is a little lower than that predicted from theory and the origin of this difference is unclear. In Figure 4.2b we show D_L/D_0 as a function of ϕ_t for the two monodisperse systems, with the prediction from Equation (4.5) calculated using $\beta = 1.675$. With the experimentally determined value of β this appears to be a good estimation of the variation of the long-time diffusion coefficient over the whole range of area fractions considered. When compared to Figure 4.2, however, it can be seen that the theoretical expression shows different qualitative behaviour to the simulation results for $\phi_t > 0.4$ and as such does not fully capture the behaviour of the long-time diffusion coefficient as a function of ϕ_t.

4.3.2 Binary system

Next the dynamic behaviour of the same $\sigma = 2.79$ μm and $\sigma = 4.04$ μm particles in a range of binary mixtures is considered. To this end, MSDs are plotted for both the small and large particles in systems of fixed composition and increasing total area fraction (shown for $q = 0.37$ in Figure 4.3) and for a fixed total area fraction ($\phi_t \approx 0.4$) and changing composition ($q = 0 \rightarrow 1$) (Figure 4.3a and b inset). For the former, similar to the monodisperse system, the MSD is linear at short and long times, indicating diffusive behaviour, and shows clearly the onset of subdiffusive behaviour at intermediate times for the higher area fractions. The same qualitative behaviour is seen for both the large and small particles for all compositions considered.

The comparison of MSD plots for systems of the same ϕ_t but different composition is more

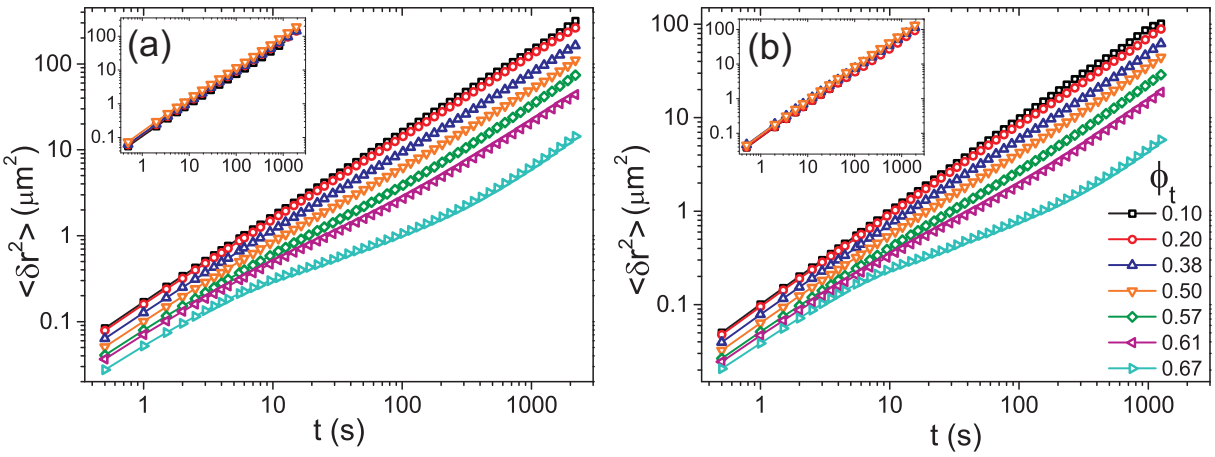

Figure 4.3: The mean squared displacement of (a) small and (b) large particles in a binary system with composition $q = 0.37$ as a function of t. Values of ϕ_t in panel (b) refer to both panels. Insets show the mean squared displacement for (a) small and (b) large particles in systems with varying composition ($q = 0.17, 0.37, 0.50$ and 0.71) but an approximately constant area fraction of $\phi_t \approx 0.4$.

challenging as the manner in which the samples are prepared makes it difficult to fix ϕ_t. As a result, approximately the same behaviour for the large and small particles across the state diagram is seen, with small variations in the total area fraction obscuring any differences in the MSD due to composition change.

The short- and long-time diffusion coefficients for the binary system at $q = 0.37$ are shown in Figure 4.4a and b. As expected from the MSDs, similar behaviour to that of the monodisperse system is seen, with both D_L and D_S decreasing with increasing total area fraction. The extrapolated values for D_0 for the small and large particles for short- and long-time diffusion are also similar to those for the monodisperse systems (see Table 4.1), with all values consistent with the Einstein expression (Equation (2.43)) when corrected for the presence of the wall [184]. The behaviour of the short-time diffusion coefficient with ϕ_t is again seen to be approximately linear over the considered range of compositions, and linear fits to the data of the form of Equation (4.3) are used to determine values of α. These are presented in Table 4.1 for both particle species in the four binary systems with $q = 0.17, 0.37, 0.50$ and 0.71. In all cases, values of α for the large and small particles in the same system are similar, and all values do not deviate significantly from those found for the monodisperse systems. Based upon Equation (2.43), the values of the diffusion coefficient are expected to scale inversely with the particle diameter and this is found to be the case for the short-time diffusion coefficients. For the long-time diffusion coefficients, however, the values of D_L for the large and small particles begin to converge as ϕ_t

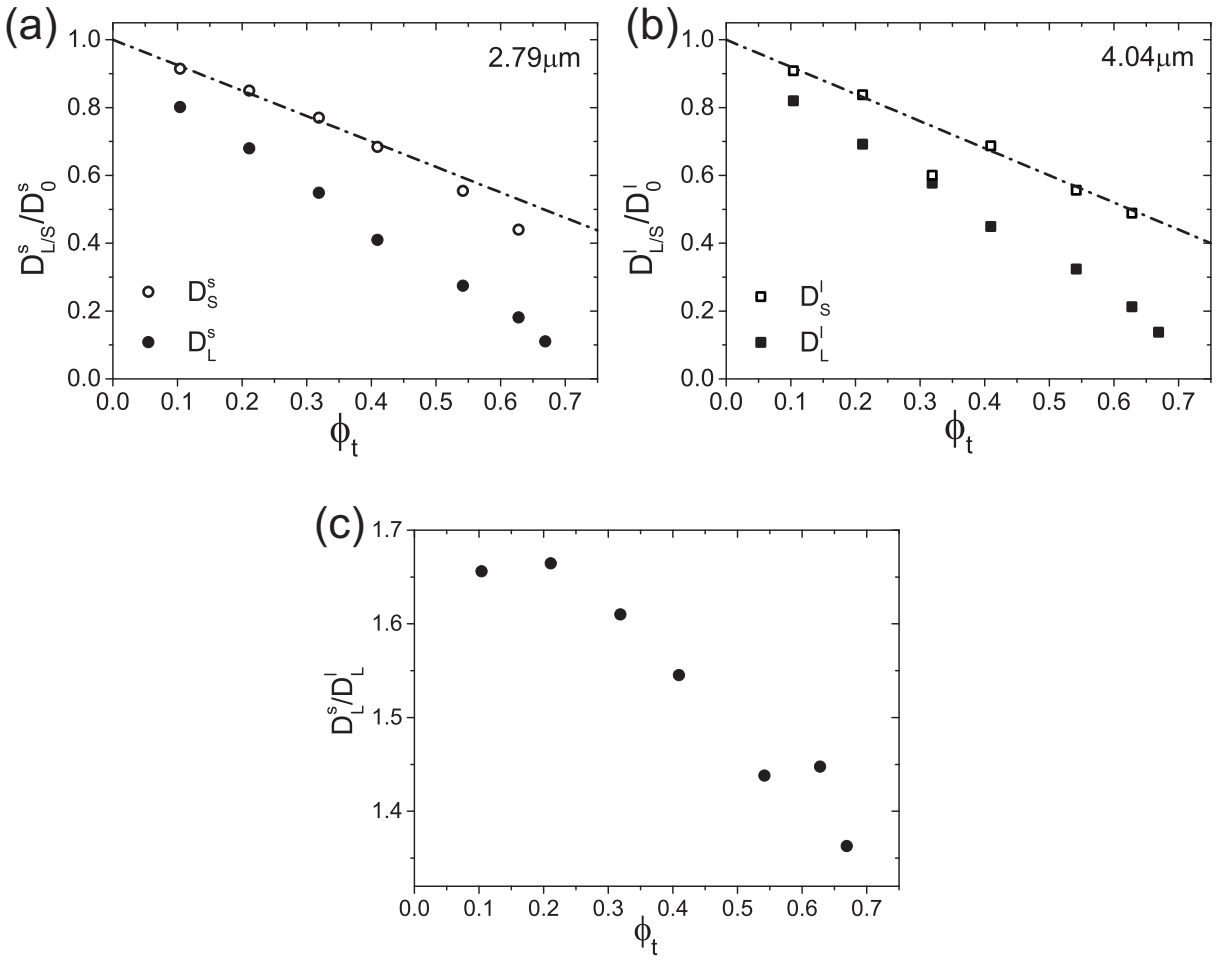

Figure 4.4: Short- and long-time self-diffusion coefficients scaled by D_0 for (a) small and (b) large particles in a binary system at $q = 0.37$. Filled circles show the long-time self-diffusion coefficient and open circles the short-time self-diffusion coefficients. The dashed line shows Equation (4.3) with $\alpha = 0.8$ in (a) and $\alpha = 0.75$ in (b). (c) The ratio of the long-time self-diffusion coefficients for the large and small particles as a function of ϕ_t.

increases. This can be seen clearly in the ratio D^l_L/D^s_L which is shown in Figure 4.4c. At low ϕ_t the value of approximately 1.65 is a little higher than the ratio of particle diameters (1.45) but is consistent with the ratio of the diffusion coefficients at infinite dilution that we find. We believe this small difference may arise from small variations in Faxen's corrections for the small and large particles.

Following the approach employed for the monodisperse systems, an ansatz to describe the long-time self-diffusion coefficient in binary systems based upon Equation (4.5) is compared to the data. This expression is of the form

$$\frac{D^i_L}{D^i_0} = \frac{1}{1 + \beta\phi_t \left[c_i g_{ii}(\sigma_{ii}) + c_j g_{ij}(\sigma_{ij})\right]}, \tag{4.7}$$

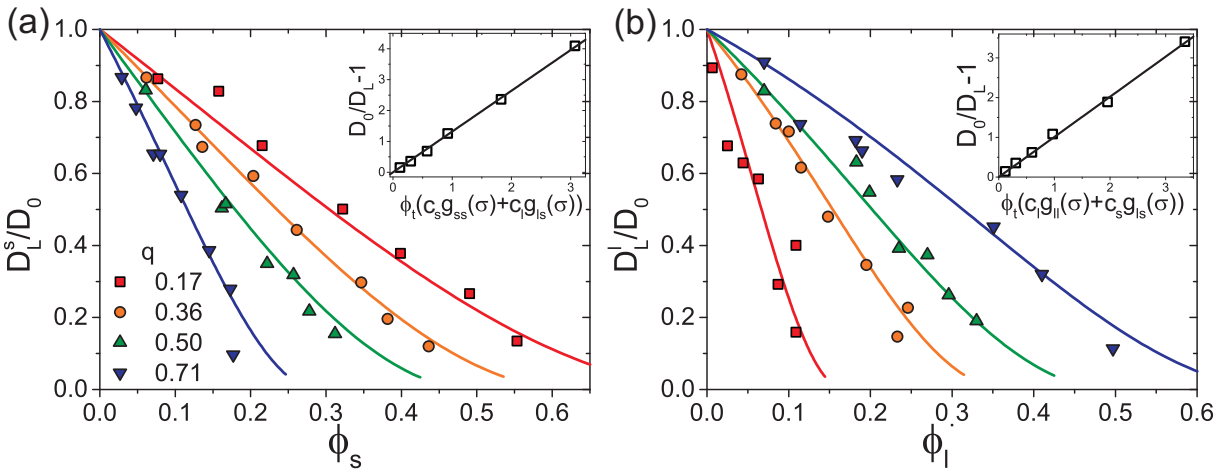

Figure 4.5: The rescaled long-time self-diffusion coefficients, D_L^i/D_0^i, for the binary systems at $q = 0.17, 0.37, 0.5$ and 0.71 for (a) small particles and (b) large particles. Also shown is the prediction from Equation (4.7). Here, diffusion coefficients for each component are plotted against the area fraction of that component for clarity. The inset shows an example of the linear plot used to calculate β for the (a) small and (b) large particles in the $q = 0.37$ system.

where i, j indicates the type of particle, c_i is the number concentration of species i, and $g_{ij}(\sigma_{ij})$ is the contact value of the partial radial distribution function with $\sigma_{ij} = (\sigma_i + \sigma_j)/2$. To account for the interactions between different types of particle the structural dependence of the expression is now changed to a linear combination of the contact values of the partial radial distribution functions scaled by their respective number concentrations. As with the monodisperse case, the contact values are well characterised (see Section 3.3.4 and [151]) allowing us to use a rearrangement of Equation (4.7), similar to Equation (4.6), to determine values of β for the small and large particles. Examples of these fits are shown in the insets of Figure 4.5 for the large and small particle subsets of the $q = 0.37$ system. In Figure 4.5 the long-time self-diffusion coefficients for (a) small and (b) large particles in systems with $q = 0.17, 0.37, 0.50$ and 0.71 are shown, with the predictions from Equation (4.7). Here, D_L^i is plotted against ϕ_i to more clearly demonstrate the level of agreement. In all cases, the data is well described by Equation (4.7).

The values of β determined for the large and small particles in binary systems with differing compositions are presented in Table 4.1. In contrast to the value of α, β is found to be systematically larger for the small particles. As β arises from an expression that considers only direct interactions via the structure of the system (Equation (4.7)), this suggests that the complex packing effects seen in binary systems have a substantial impact upon the particle diffusion. The dependence of the self-diffusion coefficient on the differing values of β will be more pronounced at high values of ϕ_t where the linear combination of contact values becomes larger.

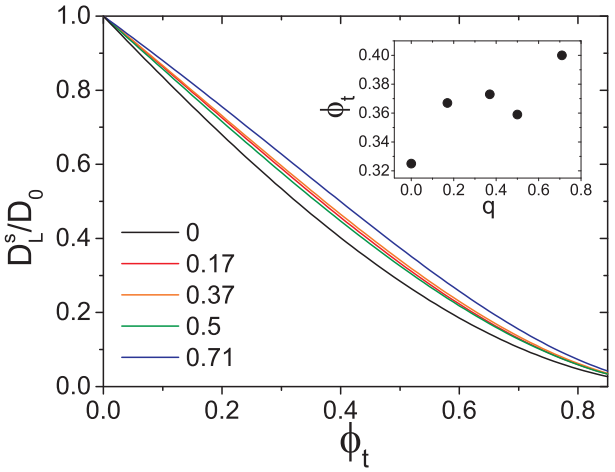

Figure 4.6: The rescaled long-time self-diffusion coefficient computed using Equation (4.7) with the experimentally determined values of β for small particles. Here the expression is plotted as a function of ϕ_t to demonstrate the variation with composition, q. Inset is the total area fraction at which the scaled long time diffusion coefficient, D_L^s/D_0, is equal to 0.5.

As such, this suggests that the convergence in the diffusion coefficients seen in Figure 4.4c may also have its origin in these packing effects.

Further to this, the variation of β with q suggests that the particle dynamics show a weak dependence upon composition. The effect of this composition dependence on the long-time diffusion coefficient can be seen from a comparison of Equation (4.7) computed for the small particles in systems with $q = 0.17, 0.37, 0.50$ and 0.71. This is shown in Figure 4.6, where the inset also shows the variation in the area fraction at which $D_l/D_0 = 0.5$ for systems at varying values of q. While a systematic trend in the composition dependence is not clear, all binary systems display faster dynamics at the same total area fraction than the monodisperse systems. The complex dependence on composition seen here is consistent with previous studies of structural relaxation in binary systems [192], where properties were seen to depend upon the composition and size ratio in an extremely complex manner.

4.4 Conclusions

The dynamic behaviour of quasi-two-dimensional monodisperse and binary colloidal systems has been studied over a wide range of total area fractions and for a variety of compositions. Mean squared displacements and self-diffusion coefficients are used to quantify the particle dynamics and show the expected trends with increasing ϕ_t. Comparison of the results for monodisperse

systems with a MC simulation indicates that at long times hydrodynamic interactions have a negligible effect upon the particle dynamics, even though hydrodynamic effects are important at short times. Short- and long-time self-diffusion coefficients for both the large and small particles are subsequently described using expressions based upon direct interactions alone, which provide a good estimation of the dynamic behaviour of the system. For the binary systems, a small dependence on the composition is seen.

Acknowledgements

This work was performed in collaboration with Jürgen Horbach, Roberto Rozas and Dirk Aarts. Thomas Skinner, Michael Juniper and Ard Louis are thanked for useful discussions.

Chapter 5

The Gaussian approximation in quasi-two-dimensional colloidal fluids

ABSTRACT

In this Chapter, the behaviour of the self-intermediate scattering function and self-van Hove correlation function for quasi-two-dimensional colloidal systems at a range of total area fractions is considered. The functions are computed both directly from the particle coordinates and via the Gaussian approximation, allowing the validity of this approximation to be probed over a range of length and timescales. Deviations from Gaussian behaviour are quantified using the non-Gaussian parameter and by a consideration of the relaxation times for the decay of the intermediate scattering function. These results are discussed with respect to the hydrodynamic limits for colloidal systems. A scaling relation is subsequently developed which is used to directly determine the combinations of wavevectors and times at which the non-Gaussian behavior is seen and to study the crossover between the diffusive regimes at long and short times.

5.1 Introduction

Light scattering techniques play an important role in the study of colloidal suspensions, where they have been used to consider various phenomena related to the structure and dynamics of these systems [168, 170, 187, 193–196]. In dynamic light scattering experiments, the central dynamic quantity is the intermediate scattering function (ISF), $F(k,t)$, which is directly related to the fluctuations in the intensity of the scattered light as a function of time [171]. $F(k,t)$ can be split into two components, which describe either the self or collective behaviour of particles, with the self (incoherent) part of the intermediate scattering function, $F_s(k,t)$, measurable using systems with strongly scattering tracer particles [168]. Calculation of this function allows a number of other properties to be determined, most importantly the self-diffusion coefficients and the mean squared displacement (MSD).

A commonly used route to convert between the self-intermediate scattering function obtained from scattering measurements and the mean squared displacement (MSD), $\langle \delta r^2(t) \rangle$, is the Gaussian approximation. This assumes that the self-ISF is Gaussian and related to the MSD as

$$F_s(k,T) = \exp(-\langle \delta r^2(t) \rangle k^2/2d), \tag{5.1}$$

where k is the wavevector and d is the dimensionality. Equation (5.1) is seen to hold in a variety of circumstances, including in the description of the motion of a harmonic oscillator and that of a system of diffusing particles. In the case of diffusion, this result arises from the fact that particles exhibit a random walk, characterised by a sequence of small independent displacements with zero mean, and hence that the central limit theorem applies. For diffusion, the combinations of wavevector and timescale for which Equation (5.1) holds is termed the hydrodynamic limit. For colloidal diffusion in particular, two diffusion coefficients and thus two hydrodynamic limits exist. These are associated with Gaussian behaviour as

$$F_s(k,t) = \exp(-D_i k^2 t), \quad i = \mathrm{S}, \mathrm{L}, \tag{5.2}$$

where D_i either corresponds to the short-time self-diffusion coefficient, D_S, or the long-time self-diffusion coefficient, D_L. For short-time diffusion, the hydrodynamic limit is associated with

length and time scales that are large compared to the characteristic scales of the surrounding solvent. This implies that values of $k \gg k_{\mathrm{p}}$ must be considered, where $k_{\mathrm{p}} = 2\pi/\sigma$ is the length associated with the diameter, σ, of the colloidal particle in reciprocal space. For long time diffusion, the opposite limit of $k \ll k_{\mathrm{p}}$ has to be considered. At intermediate length and time scales, correlated collisions for fluids at intermediate densities and the caging of particles in dense fluids lead to a failure of Equation (5.1). While this failure may lead to only small deviations of $F_s(k,t)$ from the Gaussian approximation, a clear method by which to determine precisely the regimes in which the Gaussian approximation holds is lacking.

In recent years, microscopy has become an increasingly popular alternative to light scattering for the study of colloidal systems [197, 198]. Here, the ability to directly obtain particle coordinates from the experimental images has led to properties of the system being considered mainly in terms of real space functions, such as the van Hove correlation function and the mean squared displacement. It is clear from the definitions of functions such as $F_s(k,t)$, however, that these Fourier space quantities may also be calculated directly from particle coordinates. Consequently, from microscopy it is possible to measure both the MSD and the intermediate scattering function directly, and thus to perform a rigorous test of the Gaussian approximation over a wide range of time and length scales.

In this Chapter, the self-intermediate scattering function, $F_s(k,t)$, and the self-van Hove correlation function, $G_s(x,t)$, are calculated for quasi-two-dimensional colloidal systems at a range of total area fractions. $F_s(k,t)$ and $G_s(x,t)$ are computed by two methods: firstly, directly from particle coordinates and secondly, using the particle mean squared displacements via the Gaussian approximation. A comparison of these results is used to test the validity of the Gaussian approximation over a range of length and timescales and to probe the two hydrodynamic limits, corresponding to the long- and short-time self-diffusion coefficients that are defined for colloidal fluids. Deviations from Gaussian behaviour are quantified primarily using the non-Gaussian parameter but also through a consideration of the relaxation times of $F_s(k,t)$. To this end, a scaling relation based upon the decay of the self-intermediate scattering function is used to determine directly the combinations of wavevectors and times at which the non-Gaussian behavior is seen and to study the crossover between the two diffusive regimes.

5.2 Theory

The self-intermediate scattering function, $F_{\mathrm{s}}(k,t)$, for a system of N particles is defined as

$$F_s(k,t) = \left\langle \frac{1}{N}\sum_{j=1}^{N} \exp\left[i\mathbf{k}\cdot(\mathbf{r}_j(t)-\mathbf{r}_j(0))\right] \right\rangle, \tag{5.3}$$

where $\mathbf{r}_j(t)$ is the position of particle j at time t, $\mathbf{k}$ is the wavevector and $\langle ... \rangle$ denotes a time and ensemble average. Note that as a homogeneous fluid is considered, only the magnitude of the wavevector, $k = |\mathbf{k}|$, is required. At small k, $F_s(k,t)$ may be written as a cumulant expansion of the form [199]

$$\ln F_s(k,t) = -\frac{k^2\langle \delta r^2(t)\rangle}{4} + \frac{1}{2}\alpha_2(t)\left(\frac{k^2\langle \delta r^2(t)\rangle}{4}\right)^2 + ..., \tag{5.4}$$

where $\langle \delta r^2(t)\rangle$ is the self-mean squared displacement. In the Gaussian approximation only the first term of this expansion is considered, and as such, in two dimensions (2D), the intermediate scattering function can be expressed as

$$F_{\mathrm{s}}(k,t) = \exp(-\langle \delta r^2(t)\rangle k^2/4). \tag{5.5}$$

This implies that for perfectly Gaussian particle displacements, $\alpha_2(t)$ and all higher order cumulants in Equation (5.4) are equal to zero. As such, an estimation of the extent to which a system deviates from the Gaussian approximation is provided by calculation of the non-Gaussian parameter, $\alpha_2(t)$, which is defined in 2D [200] as

$$\alpha_2(t) = \frac{1}{2}\frac{\langle \delta r^4\rangle}{\langle \delta r^2\rangle^2} - 1. \tag{5.6}$$

Here, $\langle \delta r^n(t)\rangle$ is the n^{th} moment of the self-part of the van Hove distribution, $\langle \delta r^n(t)\rangle = \int r^n G_s(r,t)\mathrm{d}r$.

The self-van Hove correlation function, is the real space analogue of the self-intermediate scattering function, and is calculated as

$$G_s(r,t) = \left\langle \frac{1}{N}\sum_{i=1}^{N} \delta[\mathbf{r}-\mathbf{r}_i(t)+\mathbf{r}_i(0)] \right\rangle. \tag{5.7}$$

This function describes the probability that a particle, i, has moved to position $\mathbf{r}_i$, after a time t, given that it was at a certain position at $t = 0$. The van Hove function may also be written in the Gaussian approximation as [99]

$$G_s(r,t) = \left(\frac{1}{\pi\langle\delta r^2(t)\rangle}\right)\exp(-r^2/\langle\delta r^2(t)\rangle), \tag{5.8}$$

with $\langle\delta r^2(t)\rangle$ again the self-mean squared displacement.

5.3 Experimental methods and data analysis

5.3.1 Colloidal model system

The quasi-2D colloidal system used is described in Section 2.3.1. Here, the dynamic behaviour of monodisperse systems of particles with diameter $\sigma = 2.79$ μm is considered. Images are recorded at two frames per second and particle coordinates are obtained as described in Sections 2.3.1 and 2.3.3. Correlation functions are calculated from the particle positions for at least 2000 frames of data. For all systems, the total packing fraction, $\phi_t = \rho\pi\sigma^2/4$, is varied over the entire range of densities characteristic of a fluid (approximately $\phi_t = 0.02$ to 0.66). The full range of systems considered are detailed in Figure 2.2a (line $q = 0$).

5.3.2 Dynamic correlation functions

The self-intermediate scattering function (ISF) is calculated from particle coordinates as

$$F_s(k,t) = \left\langle \frac{1}{N}\sum_i \exp[i\mathbf{k}\cdot(\mathbf{r}_i(t) - \mathbf{r}_i(0))] \right\rangle, \tag{5.9}$$

where $\mathbf{k}$ is the wavevector. Values of $k = |\mathbf{k}|$ are chosen to range from approximately $k = 2.5$ to 0.1 μm^{-1}, where the length in $k-$space corresponding to the particle diameter is $k = 2.25$ μm^{-1} for the $\sigma = 2.79$ μm system. The smallest value of k chosen is larger than the minimum value of k set by the field of view i.e. $k \approx 0.04$ μm^{-1}. The self-ISF is also computed in the Gaussian approximation via Equation (5.5), where the self-mean squared displacement, $\langle\delta r^2(t)\rangle$,

is calculated as (see Chapter 4)

$$\left\langle \delta r^2(t) \right\rangle = \frac{1}{N} \sum_{i=1}^{N} \left\langle [\mathbf{r}_i(t) - \mathbf{r}_i(0)]^2 \right\rangle . \tag{5.10}$$

The self-van Hove function for a uniform fluid in one dimension (1D) is calculated directly from the particle coordinates as

$$G_s(x,t) = \left\langle \frac{1}{N} \sum_{i=1}^{N} \delta[x - x_i(t) + x_i(0)] \right\rangle , \tag{5.11}$$

where for a homogeneous, isotropic system in 2D, calculation of Equation (5.11) for movement in the x or y direction leads to identical results. $G_s(x,t)$ is also calculated from the mean squared displacement in 1D via the Gaussian approximation as

$$G_s(x,t) = \left(\frac{1}{2\pi \langle \delta x^2(t) \rangle} \right)^{1/2} \exp(-x^2 / 2\langle \delta x^2(t) \rangle), \tag{5.12}$$

with

$$\left\langle \delta x^2(t) \right\rangle = \frac{1}{N} \sum_{i=1}^{N} \left\langle [x_i(t) - x_i(0)]^2 \right\rangle . \tag{5.13}$$

The degree of non-Gaussian behaviour may be quantified by the non-Gaussian parameter, $\alpha_2(t)$, in 1D, where

$$\alpha_2(t) = \frac{\langle \delta x^4(t) \rangle}{3\langle \delta x^2(t) \rangle} - 1. \tag{5.14}$$

This is calculated from the MSD and the analogous measurement for $\langle \delta x^4(t) \rangle$.

5.4 Results and discussion

Firstly, the self-intermediate scattering functions at a variety of total area fractions are considered. In Figure 5.1a and b, $F_s(k,t)$ is shown for the monodisperse system of particles with $\sigma = 2.79$ μm at $\phi_t = 0.08$ and 0.66. Here, the ISF has been calculated both directly from particle coordinates as described by Equation (5.9) and from the mean squared displacements (shown in Figure 5.1c) via the Gaussian approximation as in Equation (5.5). For the higher area

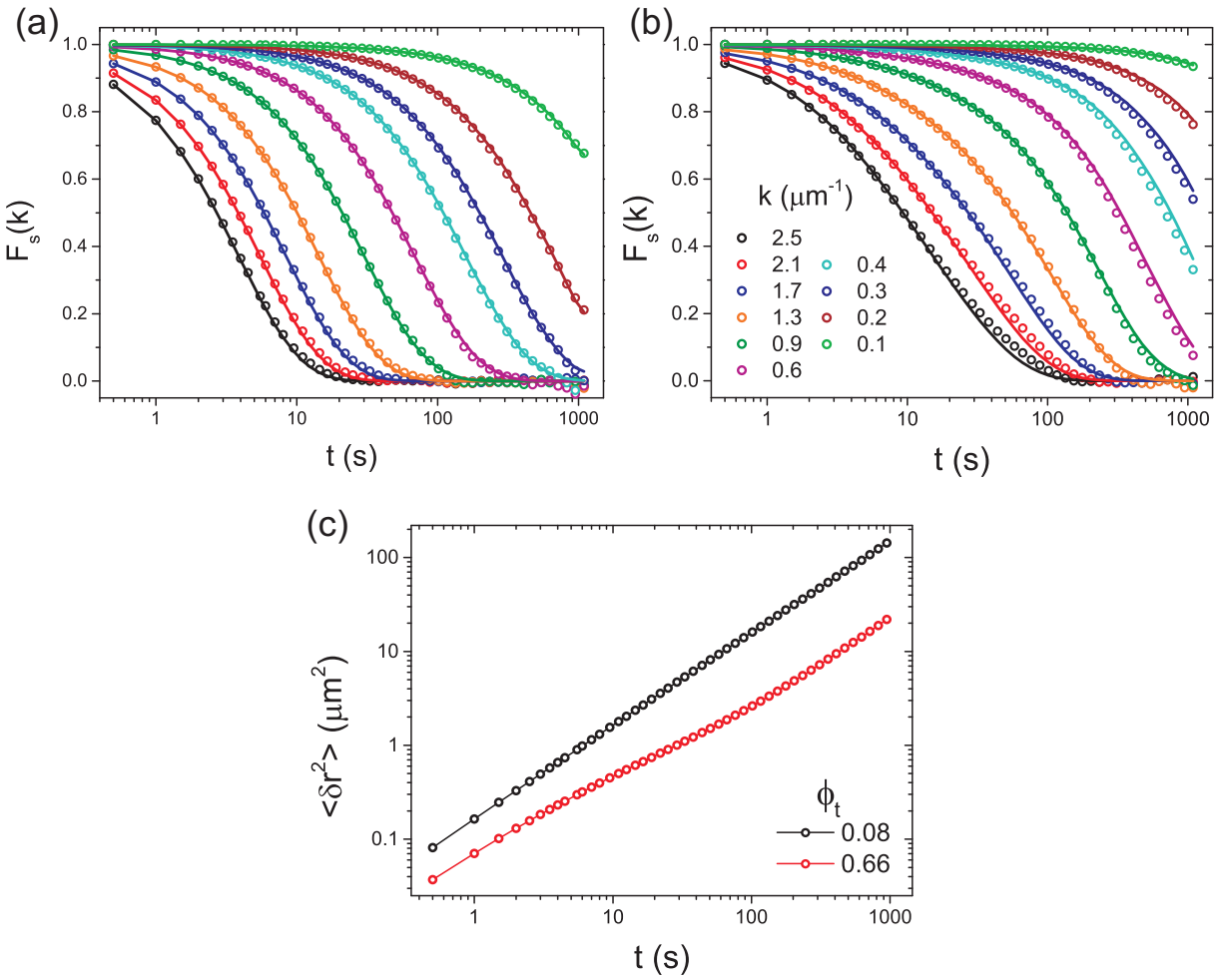

Figure 5.1: The self-intermediate scattering function as a function of k for (a) $\phi_t = 0.08$ and (b) $\phi_t = 0.66$. Values of k in (b) apply to both panels. Symbols show $F_s(k,t)$ computed from Equation (5.9) and lines are calculated from the MSD (as shown in panel (c)) using the Gaussian approximation, Equation (5.5).

fraction, slower decay of $F_s(k,t)$ at a particular value of k is seen. This is consistent with the smaller particle displacements and thus slower particle motion seen at higher ϕ_t in the MSDs. The $F_s(k,t)$ calculated directly from the particle coordinates shows good agreement with $F_s(k,t)$ calculated via the Gaussian approximation, however, small deviations are seen at long times for the system with $\phi_t = 0.66$ at almost all values of k.

The self-van Hove functions, $G_s(x,t)$, corresponding to the self-intermediate scattering functions in Figure 5.1 are shown in Figure 5.2. For comparable time delays, clearly much smaller particle displacements are observed at higher ϕ_t. This is consistent with the slower diffusion seen at higher ϕ_t as discussed in Chapter 4. Data is again shown for a direct calculation of $G_s(x,t)$ using Equation (5.11) and for a calculation via the Gaussian approximation as in

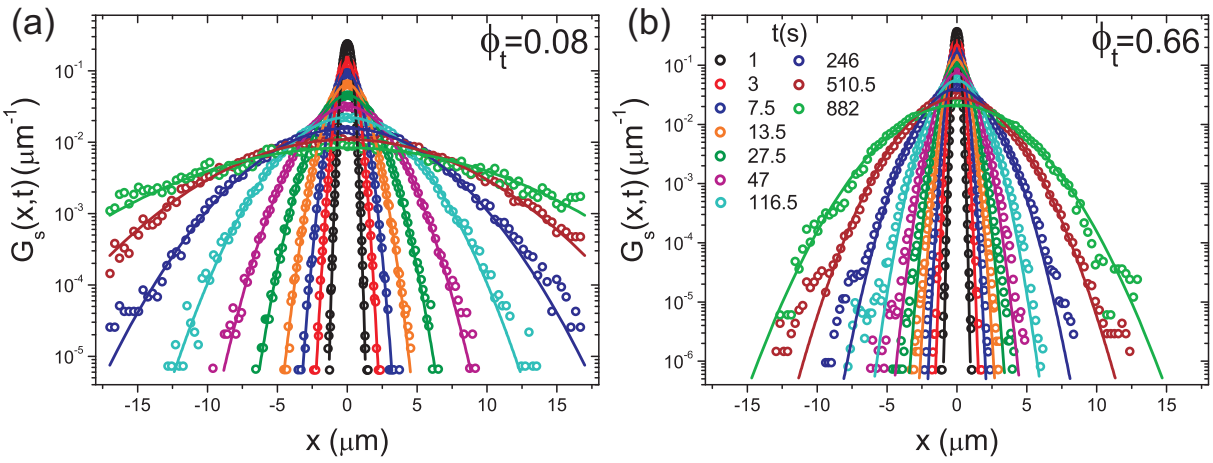

Figure 5.2: The variation of the self-van Hove function with time at (a) $\phi_t = 0.08$ and (b) $\phi_t = 0.66$. Symbols show $G_s(r,t)$ computed from Equation (5.11) and lines are calculated from the MSD using the Gaussian approximation as in Equation (5.12). Values of t in (b) apply to both panels.

Equation (5.12). Consistently, the Gaussian approximation is seen to be in good agreement with $G_s(x,t)$ calculated directly from particle coordinates, however, there are clearly some deviations at intermediate times for the system at higher ϕ_t.

Figures 5.1 and 5.2 illustrate the general trends in the behaviour of $F_s(k,t)$ and $G_s(r,t)$. In both cases, deviations from the Gaussian approximation are seen at certain values of t and k, which are small in overall magnitude, but larger for higher ϕ_t. This dependence upon total area fraction is shown more clearly in Figure 5.3a, where the variation in the behaviour of the self-intermediate scattering function with ϕ_t for a fixed value of $k = 2.2$ μm^{-1} is considered. Here, with increasing ϕ_t, both the slower decay and the increase in deviations to the Gaussian approximation at intermediate times are evident. Deviations from purely Gaussian behaviour as a function of time are now also quantified by the non-Gaussian parameter, $\alpha_2(t)$, and the variation of $\alpha_2(t)$ with ϕ_t is shown in Figure 5.3b. The agreement exhibited in Figure 5.2 is confirmed by the non-Gaussian parameter which shows only small deviations from zero. These deviations are clearly largest at intermediate time and increase with increasing ϕ_t. The non-Gaussian parameter, however, gives only an indication of the average behaviour with time, and does not provide any detailed information about the lengthscale dependence of the deviations from Gaussian behaviour seen.

To determine directly the combinations of wavevectors and times at which the non-Gaussian

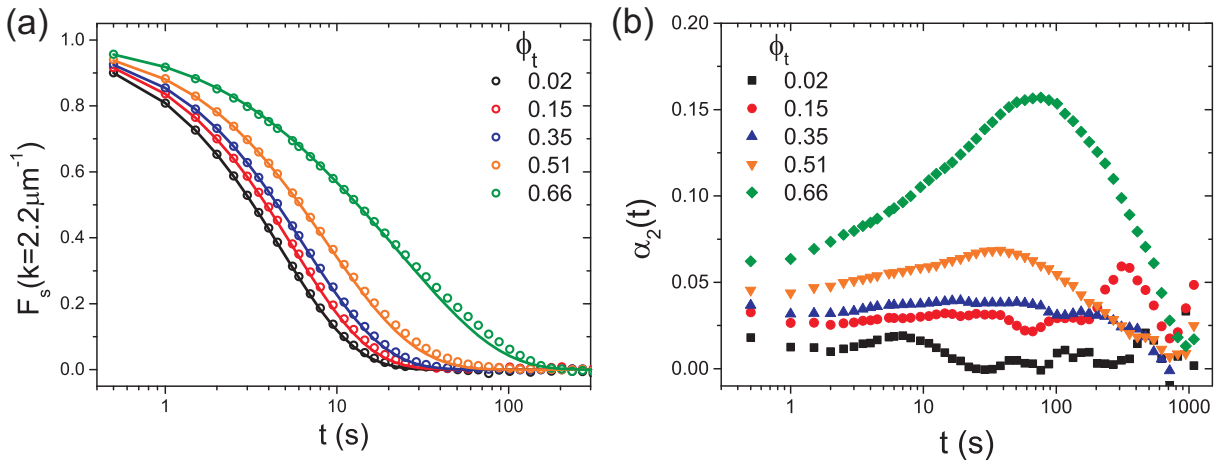

Figure 5.3: (a) The variation of the self-intermediate scattering function with total area fraction at a fixed value of k. Symbols show $F_s(k,t)$ computed from Equation (5.9) and lines are calculated from the MSD using the Gaussian approximation as in Equation (5.5). (b) The variation in the non-Gaussian parameter, $\alpha_2(t)$, with ϕ_t.

behavior is seen, the time scale $\tau_A(k)$ at which $F_s(k,t)$ decays to a given value A, is considered:

$$A = F_s(k, t = \tau_A(k))\,. \tag{5.15}$$

If $F_s(k,t)$ is Gaussian, then in the hydrodynamic limits for the colloidal system Equation (5.2) applies and Equation (5.15) becomes

$$A = \exp\left(-D_i k^2 \tau_A(k)\right), \tag{5.16}$$

where D_i with $i = S, L$ is the short- or long-time self-diffusion coefficient. From the definitions of the hydrodynamic limits, behaviour at large k and small t is expected to be governed by D_s, while that at small k and large t by D_L. It follows that

$$\frac{\ln A}{\tau_A(k)} = -D_i k^2\,, \tag{5.17}$$

and that, a scaling function, $C(k)$, may be defined as

$$C(k) = -\frac{\ln A}{\tau_A(k) k^2}\,. \tag{5.18}$$

For a fixed value of A, $C(k)$ approaches D_L for small values of k and D_S for large values of k. The intermediate k regime of $C(k)$ describes the crossover between the two diffusive regimes.

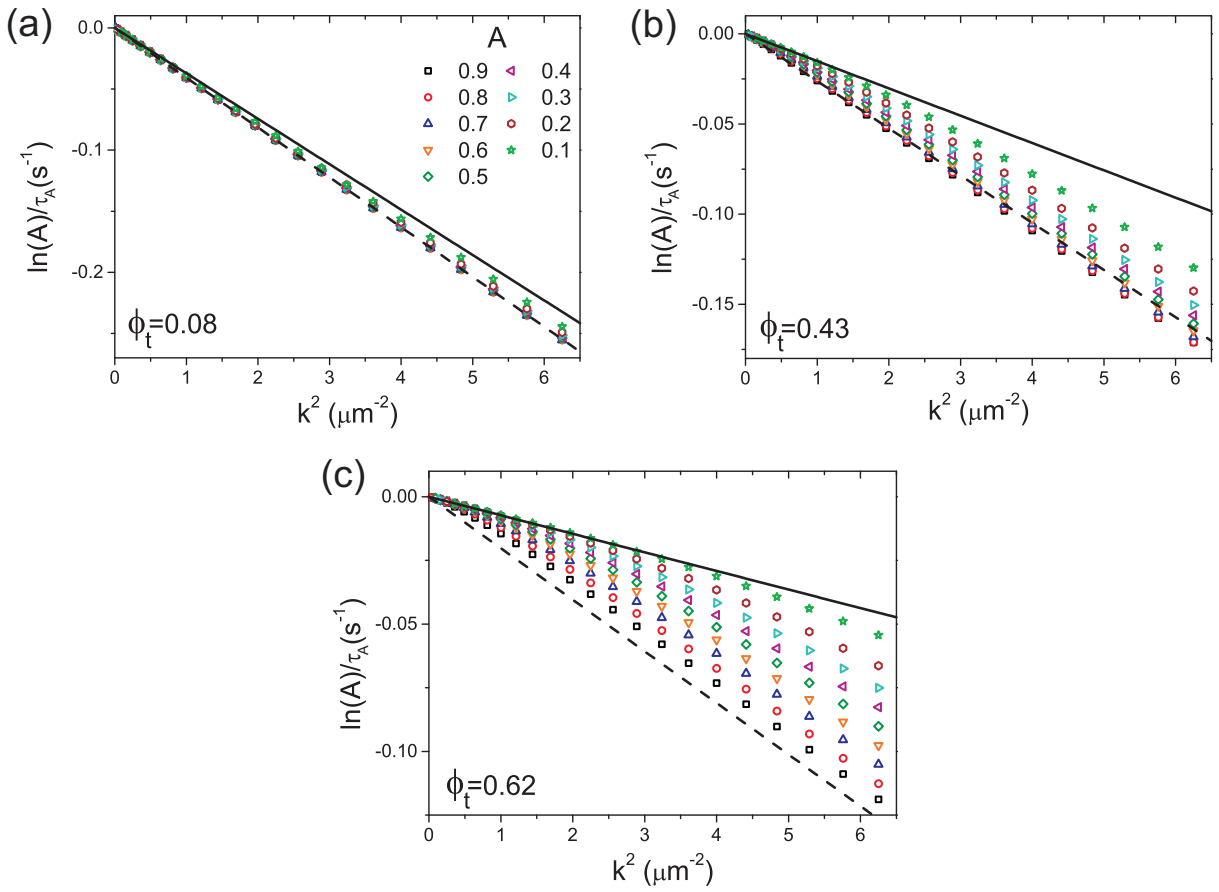

Figure 5.4: The relaxation time as defined by Equation (5.17) shown for a range of values of A at (a) $\phi_t = 0.08$, (b) $\phi_t = 0.43$ and (c) $\phi_t = 0.62$. Values of A relate to all panels. Lines show the expected gradient from an independent measurement of the self-diffusion coefficients using the mean squared displacement (see Chapter 4). Here, the dashed line is calculated from the short-time self-diffusion coefficient, D_S, and the solid line from the long-time self-diffusion coefficient, D_L.

The values of τ_A for fixed values of A, ranging from 0.9 to 0.1, are calculated by performing an interpolation upon the data for $F_s(k,t)$. The variation of τ_A with k is shown in Figure 5.4 for systems at $\phi_t = 0.08, 0.43$ and 0.62. Here, results are considered in the form described by Equation (5.17) and thus the gradient is equal to $-D_i$. As such, lines corresponding to Equation (5.17) computed using the short- and long-time self-diffusion coefficients measured from the MSDs in Chapter 4 are also shown. The comparison between the relaxation times of $F_s(k,t)$ and the two limiting gradients set by the self-diffusion coefficients in Figure 5.4a-c clearly demonstrates that there is a crossover from short to long-time behaviour with decreasing k and A. This is consistent with the fact that k is an inverse lengthscale and therefore relaxation times measured at higher k will reflect behaviour over shorter lengthscales which is naturally associated with shorter times. The value of A impacts upon the timescale probed; a longer

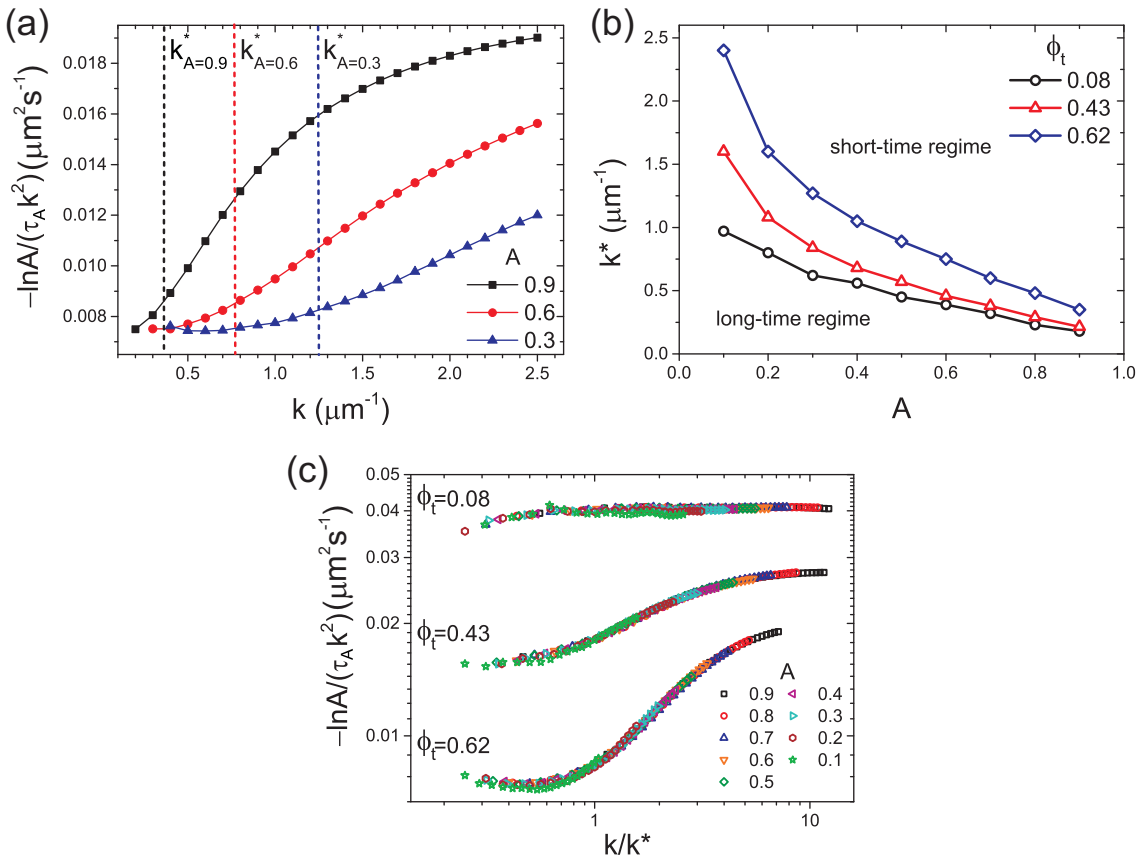

Figure 5.5: (a) The dependence of the self-diffusion coefficient via Equation (5.17) on k for three different values of the parameter A at $\phi_t = 0.62$. Vertical dashed lines indicate the value of k^* for each curve. (b) The value of k^* as a function of A for systems at $\phi_t = 0.08$, 0.43 and 0.62. (c) The variation of $C(k)$ (Equation (5.18)), with k rescaled by k^* for $\phi_t = 0.08$, 0.43 and 0.62.

time is required for $F_s(k,t)$ to decay to a lower value of A, and this automatically results in a consideration of behaviour at longer times.

The dependence of τ_A upon A is clearly much stronger for the systems at higher ϕ_t. This reflects the greater difference in the magnitude of the long- and short-time diffusion coefficients at higher ϕ_t and the differing timescales associated with the two regimes. For systems at low ϕ_t, a particle experiences relatively few direct interactions during a certain period of time due to the large average distance between particles. As such, the difference between the short-time and long-time diffusion coefficients, which arises from direct interactions, is relatively small, and only at very long times and lengthscales is the crossover to the long-time behaviour seen (see Figure 5.4a). In contrast, for higher area fractions, the distance a particle must travel in order to directly interact with another particle is very short, resulting in significant number of direct interactions at short times. This both significantly reduces the value of the long-time diffusion

coefficient relative to its short-time value, but also results in a crossover from the short- to long-time regime at much earlier time and lengthscales. This is illustrated in Figure 5.4c where τ_A exhibits a gradient consistent with the long-time diffusion coefficient at reasonably high values of k .

An alternative representation of the data in Figure 5.4 is presented in Figure 5.5, where the scaling relation of Equation (5.18) is considered. Figure 5.5a shows the variation of $C(k)$ with k at three values of A for the system with $\phi_t = 0.62$. Also indicated is the value of k^* determined from the point of inflection of these lines. The value of k^* indicates a crossover point between short- and long-time behaviour, and in Figure 5.5b k^* is plotted as a function of A. For all three values of ϕ_t, k^* increases with decreasing A. This is because the behaviour at small A corresponds to that at long times and thus long-time behaviour is seen even for large values of k. Furthermore, k^* for a fixed value of A is seen to decrease with ϕ_t, demonstrating that as the total area fraction decreases, the lengthscale associated with the crossover between short- and long-time behaviour increases.

Finally, $C(k)$ computed for all values of A is replotted with k now rescaled by k^*. This is shown in Figure 5.5c for systems with $\phi_t = 0.08$, 0.43 and 0.62, where data for different values of A for each ϕ_t are seen to fall onto one master curve. Here, the presence of the long- and short-time regimes for the three different area fractions is clear, with the difference in long- and short-time behaviour seen to increase with ϕ_t. In addition to this, universal behaviour is seen with respect to the scaling relation $C(k)$, at intermediate values of k. This is surprising, due to the fact that the mechanisms that govern particle motion at intermediate times are complex, and expected to differ with area fraction. As a general point, both Figure 5.4 and Figure 5.5 provide significantly more information regarding the nature of the crossover from long- to short-time behaviour than that available from calculation of the non-Gaussian parameter. In particular, the quantity k^* characterises the ranges of k for which the two hydrodynamic limits as a function of ϕ_t are seen.

5.5 Conclusion

The self-intermediate scattering function, $F_s(k,t)$, and the self-van Hove correlation function, $G_s(x,t)$, for quasi-two-dimensional colloidal systems have been considered, with a particular

focus upon the estimation of these quantities using the Gaussian approximation. In general the Gaussian approximation is in good agreement with a direct measurement of $G_s(x,t)$ and $F_s(k,t)$, however, small deviations are seen that depend sensitively upon time, total area fraction and the wavevector by which the system is probed. These deviations are found to disappear in the two hydrodynamic limits defined for colloidal fluids, governed by the long- and short-time diffusion coefficients, respectively. The relaxation times of $F_s(k,t)$ are seen to obey a scaling relation, $C(k)$, which allows for the determination of the combinations of wavevectors and times at which the non-Gaussian behavior is seen. Furthermore, as $C(k)$ approaches D_L for small values of k and D_S for large values of k, the intermediate k regime of $C(k)$ is used to quantify the crossover between the two diffusive regimes.

Acknowledgements

This work was performed in collaboration with Jürgen Horbach and Dirk Aarts. Michael Juniper is thanked for useful discussions.

Chapter 6

Interdiffusion in quasi-two-dimensional binary colloidal fluids

ABSTRACT

In this Chapter, interdiffusion in quasi-two-dimensional binary colloidal fluids at two different size ratios is studied. Firstly, the thermodynamic drive for interdiffusion is considered in terms of the thermodynamic factor, which is calculated from the small wavevector limit of the concentration-concentration structure factor using an analysis of the concentration fluctuations. The thermodynamic factor varies substantially with the size ratio of the binary fluid, indicating that structural ordering occurs for the large size ratio system. Next, the interdiffusion mean squared displacement (MSD) is measured in two ways: via the Darken equation, which is based on a linear combination of self-diffusion coefficients, and directly from the particle trajectories by developing an expression in terms of the centre of mass MSD. The agreement between the MSDs calculated by the two routes is found to vary with both the size ratio and the composition, and consequently the applicability of the Darken equation to these systems is discussed.

6.1 Introduction

Collective transport phenomena are dynamic processes which involve the movement of multiple single interacting entities in a cooperative way [201]. Understanding these effects is of significant interest due to their ubiquity, playing an important role in a diverse range of systems varying from bacterial colonies [202] and flocks of birds [203] to granular matter [204] and glasses [205]. Within this range of systems, a clear distinction is made between those at equilibrium and those that are active, with the primary difference the momentum conservation properties of collisions between individual units. Liquids, as considered in this thesis, clearly belong to the set of equilibrium systems that exhibit collective behaviour, which here governs properties including their thermal diffusivity and bulk viscosity [99]. In this case, many of the transport properties of single particles have collective analogues, a simple example of this being collective diffusion, which involves the movement of particles from regions of higher to lower particle number [171, 206]. For systems at a certain particle density, this may in fact be faster than self-diffusion [121, 171].

The process by which one species in a mixture of two types of particles moves down its respective concentration gradient to form a more homogeneous mixture is known as interdiffusion [152]. The key transport coefficient associated with this is the interdiffusion coefficient, D_{ab} [99]. As many physical systems are in fact made up of multiple components, understanding mixing effects such as interdiffusion is of fundamental importance for the characterisation and design of new materials. An obvious class of systems for which an understanding of interdiffusion is thus particularly relevant is that of metallic alloys. Experimentally, studies of interdiffusion in these systems are performed on set-ups with a macroscopic concentration gradient using the long-capillary technique [207]. Here, however, various experimental difficulties, including the possibility of convective flow or inhomogeneities in the sample [208], make the accurate measurement of an interdiffusion coefficient very difficult. Consequently, systematic studies of the diffusive behaviour of these systems are rare.

In simulation, it is possible to study interdiffusion by probing the relaxation of concentration fluctuations in a binary system at equilibrium [152, 209, 210]. In principle, similar data is available for colloidal systems, however an equivalent analysis of an experimental system has not yet been performed. This is primarily due to the fact that the expressions developed for the statistical mechanical ensembles used in simulation are not applicable to an experimental

system best described by the grand canonical ensemble. For both microscopy and simulation the determination of collective properties is more difficult than for their self-counterparts. This arises from a combination of the inevitably poorer statistics for collective properties, where it is no longer possible to average over multiple particles, and the need to consider finite size effects; i.e. the impact of the system size upon the measurement.

These difficulties associated with the measurement of the interdiffusion coefficient mean that significant interest lies in the ability to approximate this property from the more easily determined self-diffusion coefficients. A widely used theoretical approximation for D_{ab} is the empirical expression of Darken [211], where

$$D_{ab} = \Phi(c_a D_b + c_b D_a), \tag{6.1}$$

with c_i the concentration of species i, Φ the thermodynamic factor and D_i the self-diffusion coefficient of species i. This has been shown to be a good estimate of the interdiffusion coefficient in simulation, experiment and mode coupling theory studies [207, 209, 212], even for systems relatively close to the glass transition [152].

In this Chapter, interdiffusion in quasi-two-dimensional binary colloidal fluids with size ratios $\gamma = 1.45$ and $\gamma = 2.19$ is studied, with a focus upon the applicability of the Darken equation to these systems. Interdiffusion is characterised by the behaviour of the interdiffusion mean squared displacement (MSD), which is calculated in two ways; firstly, via the Darken equation, and secondly from an expression based upon the centre-of-mass MSD of a subset of particles. For the calculation by the Darken equation, the thermodynamic factor is first determined from the small wavevector limit of the concentration-concentration structure factor, $S_{cc}(k)$, using an analysis of the concentration fluctuations. The dependence of the thermodynamic factor upon the total area fraction is seen to vary with γ, and this is discussed in relation to the nonadditivity. Self-diffusive properties are calculated as in Chapter 4. For the computation of the centre of mass MSD, an expression is developed that allows for a direct measurement of the interdiffusion MSD from the centre of mass MSD of a subset of large or small particles. Experimental determination of the interdiffusion mean squared displacement by this method is discussed, and in particular, its dependence upon the size of the particle subset. Finally, the agreement between the interdiffusion MSDs calculated by the two methods is considered to determine the validity of the Darken equation for systems at different size ratios.

6.2 Theory

The most commonly used expression for describing the interdiffusion coefficient, D_{ab}, is given by

$$D_{ab} = M\Phi(c_a D_b + c_b D_a), \tag{6.2}$$

with $c_i = N_i/N$ the number concentration of species i, D_i the self-diffusion coefficient, M the Manning factor and Φ the thermodynamic factor. Equation (6.2) implies that the rate at which a system will mix depends on both thermodynamic and kinetic properties of the system. In Equation (6.2) the kinetic component is approximated by a linear combination of the weighted self-diffusion coefficients, and the thermodynamic component by the thermodynamic factor, Φ [209] , which is related to the $k \to 0$ limit of the concentration-concentration static structure factor as

$$\Phi = \frac{c_l c_s}{S_{cc}(k \to 0)}. \tag{6.3}$$

The thermodynamic factor accounts for the tendency of concentration fluctuations to relax over large lengthscales. To exemplify this, for a system close to the critical point, $S_{cc}(k \to 0)$ will be extremely large due to large scale concentration fluctuations [210, 213] and consequently the thermodynamic factor very small. For systems which tend to order the opposite behaviour is seen [152]. The choice of a linear combination of self-diffusion coefficients in Equation (6.2) excludes cross-correlations between the two types of particles, and as such M acts as a correction factor to account for these cross-correlations and other non-ideal mixing effects. If $M = 1$, the Darken equation (Equation (6.1)) is recovered, and the Manning factor may therefore be used to quantify the extent to which the Darken equation is a good approximation to the observed interdiffusive behaviour. This may depend sensitively upon the system composition, as simulation results suggest that both the thermodynamic and kinetic components of Equation (6.3) show complex and differing dependencies upon composition [209].

6.2.1 The interdiffusion coefficient

For a binary fluid consisting of N_a particles of type a and N_b particles of type b the interdiffusion current, $\mathbf{J}_{ab}(t)$, is defined as [152]

$$\mathbf{J}_{ab}(t) = \sum_{i=1}^{N_a} \mathbf{v}_{a,i}(t) - c_a \left[\sum_{i=1}^{N_a} \mathbf{v}_{a,i}(t) + \sum_{i=1}^{N_b} \mathbf{v}_{b,i}(t) \right], \tag{6.4}$$

where $\mathbf{v}_{j,i}(t)$ is the velocity of a particle, i, of species $j = a, b$ at time t and c_a is again the number concentration of species a. The behaviour of the interdiffusion current will vary with the type of ensemble under consideration, and a simplified form of Equation (6.4) may be obtained using an ensemble-dependent expression to link the velocities of the two components.

The interdiffusion coefficient is now obtained by constructing the autocorrelation function of $\mathbf{J}_{ab}$ as

$$C_{ab}(t) = \langle \mathbf{J}_{ab}(t) \cdot \mathbf{J}_{ab}(0) \rangle, \tag{6.5}$$

which is related to the interdiffusion coefficient via a Green-Kubo integral [152] by

$$D_{ab} = \frac{1}{dNS_{cc}(k \to 0)} \int_0^\infty C_{ab}(t) \mathrm{d}t. \tag{6.6}$$

with d the dimensionality. Importantly, diffusion and interdiffusion coefficients calculated by a Green-Kubo relation must be identical to those calculated from the Einstein relation (Equation (2.42)) [99]. The equivalence of these approaches may be seen by combining (6.4) and (6.5) with Equation (6.6). The resulting integrand is a function of the particle velocities, and thus may be related to particle displacements by considering the relationship

$$\int_0^t \mathbf{v}_i(t') \mathrm{d}t' = \mathbf{r}_i(t) - \mathbf{r}_i(0). \tag{6.7}$$

where $\mathbf{r}_i(t)$ is the position of particle i at time t. As such, the interdiffusion coefficient may also be obtained from the computation of an appropriate mean squared displacement.

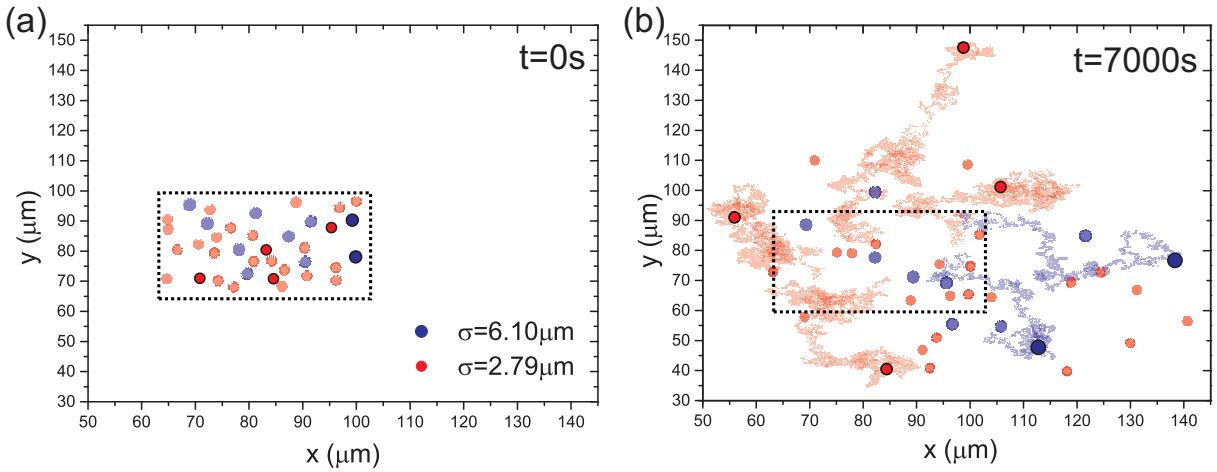

Figure 6.1: An example of the particle tracking procedure used: (a) The position of a subset of small and large particles at $t = 0$ and (b) the positions of the same particles after 7000s with a few tracks to illustrate the particle motion.

6.3 Experimental methods and data analysis

6.3.1 Colloidal model system

The binary quasi-2D colloidal model system used is described in Section 2.3.1. Here, the specific systems considered are those at large size ratio, with $\gamma = 2.19$ and $q = 0.48$, and those at small size ratio with $\gamma = 1.45$ and compositions $q = 0.37$ and $q = 0.5$. The behaviour is considered at a variety of total area fractions, ϕ_t, where for the system at $\gamma = 2.19$ the area fraction of large particles is calculated using the in-plane large particle radius (see Section 3.3.3).

Video-microscopy is used to record images at a rate of two frames per second for up to 120 minutes and particle trajectories are acquired as described in Sections 2.3.1 and 2.3.3. Static correlation functions are calculated from particle positions for at least 200 frames of data and self-diffusive behaviour is determined as described in Chapter 4.

6.3.2 Centre of mass coordinates

For the determination of the centre of mass coordinates, the particle tracking must be performed such that no particles are lost over the length of the data. To achieve this, particles are selected from within a certain region in the $t = 0$ frame, and then only these particles are tracked throughout the data, as illustrated in Figure 6.1. This region is selected such that no particles

move out of view throughout the course of the experiment. Consequently, this area is smaller for systems at lower total area fractions in which the particle displacements are larger. From these trajectories, the centre of mass (COM) coordinates of the two components are defined as

$$\mathbf{R}_a(t) = \frac{1}{N_a}\sum_{i=1}^{N_a}\mathbf{r}_{a,i}(t) \quad \text{and} \quad \mathbf{R}_b(t) = \frac{1}{N_b}\sum_{i=1}^{N_b}\mathbf{r}_{b,i}(t), \tag{6.8}$$

and the COM of all tagged particles, i.e. both large and small, as

$$\mathbf{R}(t) = \frac{1}{N}\sum_{i=1}^{N}\mathbf{r}_i(t) = \frac{1}{N}\left[\sum_{i=1}^{N_a}\mathbf{r}_{a,i}(t) + \sum_{i=1}^{N_b}\mathbf{r}_{b,i}(t)\right]. \tag{6.9}$$

6.3.3 The concentration-concentration structure factor.

Partial static structure factors for the binary systems, $S_{ij}(k)$ $(i,j = l,s)$, are calculated as

$$S_{ij}(\mathbf{k}) = \frac{1}{N}\left\langle\sum_{\nu=1}^{N_i}\sum_{\mu=1}^{N_j}\cos(\mathbf{k}\cdot\mathbf{r}_\nu)\cos(\mathbf{k}\cdot\mathbf{r}_\mu)\right\rangle + \frac{1}{N}\left\langle\sum_{\nu=1}^{N_i}\sum_{\mu=1}^{N_j}\sin(\mathbf{k}\cdot\mathbf{r}_\nu)\sin(\mathbf{k}\cdot\mathbf{r}_\mu)\right\rangle, \tag{6.10}$$

where $\mathbf{r}_{\nu,\mu}$ is the position of particle ν of species i or μ of species j, and $\mathbf{k}$ is the wavevector. These are used to form the linear combination related to concentration fluctuations, $S_{cc}(k)$, as

$$S_{cc}(k) = c_j^2 S_{ii}(k) + c_i^2 S_{jj}(k) - 2c_i c_j S_{ij}(k). \tag{6.11}$$

with c_i the number concentration. As for the monodisperse and number-number structure factors (see Section 3.2.3), the value of the $k \to 0$ limit of $S_{cc}(k)$ may be estimated by an analysis of fluctuations within the system. The variable of interest is now the fluctuation in number concentration, δc_i, defined as

$$\begin{aligned}\delta c_i &= \frac{1}{N}\left[\langle c_i^2\rangle - \langle c_i\rangle^2\right] \\ &= \frac{1}{N}\left[\left\langle\frac{N_i^2}{N^2}\right\rangle - \left\langle\frac{N_i}{N}\right\rangle^2\right],\end{aligned} \tag{6.12}$$

where i denotes either the large or small species. As the number of small and large particles are linked via the total number of particles, N, a consideration of either the small or large particle concentration fluctuations produces equivalent results. Again, δc_i is calculated for a range of

box sizes with an extrapolation to infinite box size used to determine the value of c_i for an infinite system size (see Section 3.2.3).

6.4 Results and discussion

Firstly, an expression for the interdiffusion coefficient relevant to the experimental system considered here is developed following the approach described in Section 6.2.1. The interdiffusion current, $\mathbf{J}_{ab}(t)$, is again defined as

$$\mathbf{J}_{ab}(t) = \sum_{i=1}^{N_a} \mathbf{v}_{a,i}(t) - c_a \left[\sum_{i=1}^{N_a} \mathbf{v}_{a,i}(t) + \sum_{i=1}^{N_b} \mathbf{v}_{b,i}(t) \right], \tag{6.13}$$

where $\mathbf{v}_{j,i}(t)$ is the velocity of a particle of species $j = a, b$ at time t and c_a is the number concentration of species a. The centre of mass velocity of species j is defined as

$$\mathbf{V}_j = \frac{1}{N_j} \sum_{i=1}^{N_j} \mathbf{v}_{j,i}(t), \tag{6.14}$$

where $j = a, b$, and as such Equation (6.13) may be rewritten as

$$\mathbf{J}_{ab} = N_a \mathbf{V}_a(t) - c_a[N_a \mathbf{V}_a(t) + N_b \mathbf{V}_b(t)]. \tag{6.15}$$

In our system the numbers of a and b particles are fixed (see Figure 6.1), so the term in square brackets of Equation (6.13) is in fact the sum over all particles or equivalently,

$$\sum_{i=1}^{N_a} \mathbf{v}_{a,i}(t) + \sum_{i=1}^{N_b} \mathbf{v}_{b,i}(t) = \sum_{i=1}^{N} \mathbf{v}_i(t) = N\mathbf{V}(t), \tag{6.16}$$

allowing us to write Equation (6.15) as

$$\mathbf{J}_{ab} = N_a \mathbf{V}_a(t) - c_a[N\mathbf{V}(t)] = N_a[\mathbf{V}_a(t) - \mathbf{V}(t)]. \tag{6.17}$$

Here, $\mathbf{V}(t)$ is the centre of mass velocity of all particles. It can be seen that the interdiffusion current is related to the centre of mass velocity of one component relative to the centre of mass velocity of the whole system. As such, a relative centre of mass velocity is now defined for

component a as

$$\widetilde{\mathbf{V}}_a(t) = \mathbf{V}_a(t) - \mathbf{V}(t). \tag{6.18}$$

To obtain the interdiffusion coefficient, the autocorrelation function of $\mathbf{J}_{ab}$ is constructed as

$$C_{ab}(t) = \langle \mathbf{J}_{ab}(t) \cdot \mathbf{J}_{ab}(0) \rangle = N_a^2 \langle \widetilde{\mathbf{V}}_a(t) \cdot \widetilde{\mathbf{V}}_a(0) \rangle. \tag{6.19}$$

The Green-Kubo formula for the interdiffusion coefficient in 2D is

$$D_{ab} = \frac{1}{2NS_{cc}(k \to 0)} \int_0^\infty C_{ab}(t) \mathrm{d}t \tag{6.20}$$

or equivalently using Equation (6.3) and Equation (6.19),

$$\begin{aligned} D_{ab} &= \frac{\Phi}{2Nc_a c_b} \int_0^\infty N_a^2 \langle \widetilde{\mathbf{V}}_a(t) \cdot \widetilde{\mathbf{V}}_a(0) \rangle \mathrm{d}t \\ &= \frac{N\Phi c_a}{2c_b} \int_0^\infty \langle \widetilde{\mathbf{V}}_a(t) \cdot \widetilde{\mathbf{V}}_a(0) \rangle \mathrm{d}t. \end{aligned} \tag{6.21}$$

Finally, the relative centre of mass position, $\widetilde{\mathbf{R}}_a$, is defined using Equation (6.8) as

$$\begin{aligned} \widetilde{\mathbf{R}}_a &= \mathbf{R}_a(t) - \mathbf{R}(t) \\ &= \frac{1}{N_a} \sum_{i=1}^{N_a} \mathbf{r}_{a,i}(t) - \frac{1}{N} \left[\sum_{i=1}^{N_a} \mathbf{r}_{a,i}(t) + \sum_{i=1}^{N_b} \mathbf{r}_{b,i}(t) \right], \end{aligned} \tag{6.22}$$

where $\widetilde{\mathbf{R}}_a(t) - \widetilde{\mathbf{R}}_a = \int_0^t \widetilde{\mathbf{V}}_a(t') \mathrm{d}t'$. Thus, the equivalence of the Einstein and Green-Kubo relations (see Section 6.2.1) implies that the interdiffusion coefficient may be expressed as

$$\begin{aligned} D_{ab} &= \lim_{t \to \infty} N\Phi \frac{c_a}{c_b} \frac{[\widetilde{\mathbf{R}}_a(t) - \widetilde{\mathbf{R}}_a(0)]^2}{4t} \\ &= \lim_{t \to \infty} N\Phi \frac{c_a}{c_b} \frac{\langle \delta \widetilde{R}_a^2(t) \rangle}{4t}, \end{aligned} \tag{6.23}$$

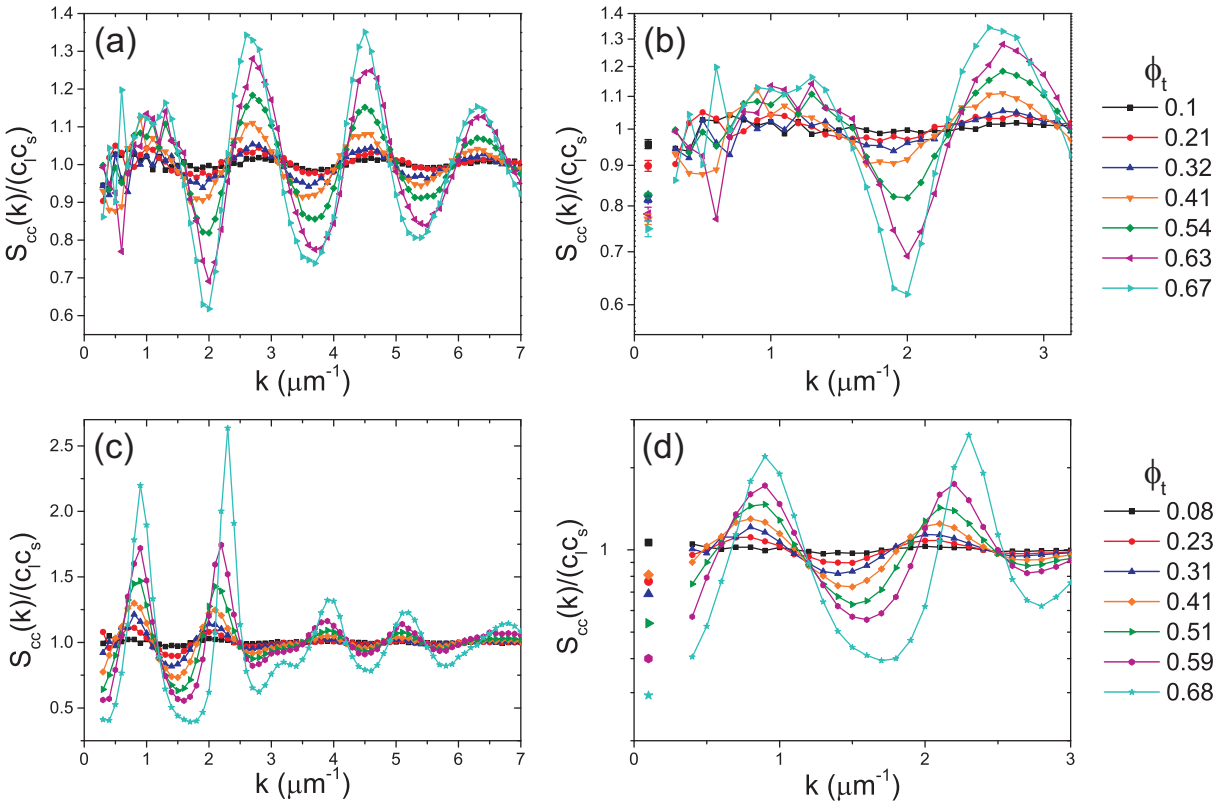

Figure 6.2: The variation in the concentration-concentration structure factor, $S_{cc}(k)$, with ϕ_t for binary systems: (a) and (b) $\gamma = 1.45$ and $q = 0.37$; (c) and (d) $\gamma = 2.19$ and $q = 0.48$. Note that $S_{cc}(k)$ is rescaled by the product of the number concentrations of the two components, $c_l c_s$. (b) and (d) show the small k behaviour with the results of the concentration fluctuation analysis.

where $\langle \delta \widetilde{R}_i^2(t) \rangle$ with $i = a, b$ is the centre of mass mean squared displacement. From this the interdiffusion MSD, $\langle \delta R^2(t) \rangle_{\text{int,COM}}$, is defined by

$$D_{ab} = \Phi \lim_{t \to \infty} \frac{\langle \delta R^2(t) \rangle_{\text{int,COM}}}{4t}, \tag{6.24}$$

so that

$$\langle \delta R^2(t) \rangle_{\text{int,COM}} = N \frac{c_a}{c_b} [\langle \delta \widetilde{R}_a^2(t) \rangle]^2. \tag{6.25}$$

Conveniently, this expression can be directly compared to the kinetic part of the Darken equation, $c_a D_b + c_b D_a$ (Equation (6.1)). Note that while Equation (6.25) is written in terms of the centre of mass of species, a, identical interdiffusion coefficients can be measured from a consideration of either set of particle coordinates. Also, in the following the species a and b are the large and small particles, and so are replaced with l and s.

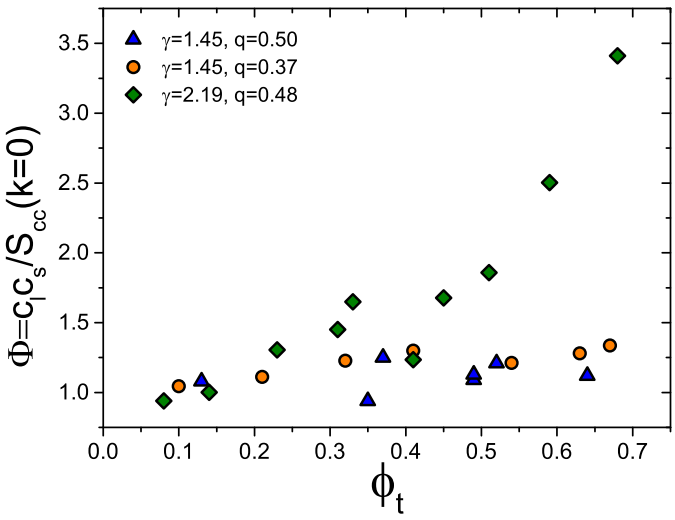

Figure 6.3: The thermodynamic factor, Φ, as a function of ϕ_t for the systems at $\gamma = 1.45$ with $q = 0.37$ and $q = 0.50$; and for the system with $\gamma = 2.19$ and $q = 0.48$.

Now, the thermodynamic driving force for interdiffusion is considered by calculation of the thermodynamic factor from the $k \to 0$ limit of the concentration-concentration structure factor, $S_{cc}(k)$. The variation in $S_{cc}(k)$ with total area fraction, ϕ_t, for the small size ratio system ($\gamma = 1.45$) at $q = 0.37$ and large size ratio ($\gamma = 2.19$) at $q = 0.48$ is shown in Figure 6.2a and c, respectively. Equation (6.11) shows that the composition effects are here governed by the number concentration, c_i, not the area fraction ratio, q. Systems compared are, therefore, those with the most similar number concentrations. The large-k limit of $S_{cc}(k)$ is expected to tend to the product of the number concentrations of the two components, and as such the data is rescaled by this product and thus tends to unity for large k. This removes any variation in the large k limit that arises from small fluctuations in the relative concentrations of the two components, allowing for the dependence of S_{cc} upon ϕ_t alone to be studied. Evident in both plots is the increase in structure of $S_{cc}(k)$ as the total packing fraction increases, however, for comparable values of ϕ_t the amplitudes of the peaks of $S_{cc}(k)$ are clearly much larger for the system at $\gamma = 2.19$.

The variation of $S_{cc}(k)$ in the limit $k \to 0$ is clearly much greater for the system at a large size ratio. This can be seen more clearly in Figure 6.2b and d, where the small k region of $S_{cc}(k)$ is shown with the results of the concentration fluctuation analysis described in Section 6.3.2. In general, good agreement is seen between the apparent limit of the concentration-concentration

structure factor and the limit found from the fluctuations in c_i. The thermodynamic factor, Φ, can now be readily calculated from $S_{cc}(k \to 0)$ using Equation (6.3) and the variation of Φ with total area fraction is shown in Figure 6.3. For $\gamma = 1.45$, very little variation in Φ is seen for both the systems with composition $q = 0.37$ and $q = 0.50$ over the entire area fraction range. This indicates that for the small size ratio system, there are no significant mixing effects even at high total packing fraction. In contrast to this, for $\gamma = 2.19$, the thermodynamic factor exhibits a significant increase across the range of ϕ_t considered. This indicates that as the total area fraction increases, concentration fluctuations within the system are increasingly suppressed, and this is characteristic of a system that exhibits ordering phenomena. The structural behaviour of the two systems has already been discussed in Chapter 3 where the ordering effects displayed by the system at $\gamma = 2.19$ were ascribed to its higher nonadditivity. This is consistent with the behaviour of the thermodynamic factor.

Next, the kinetic component of the expression for the interdiffusion coefficient is considered by calculating the interdiffusion MSD directly from the centre of mass (COM) MSD using Equation (6.25) and comparing the result to the kinetic part predicted by the Darken approximation. From Equation (6.25) it is seen that to probe interdiffusion in the system, any concerted movement of the whole tagged subset of particles is removed by subtracting the COM of all particles from that of each subset. In Figure 6.4a, an example of the particle trajectories over 500 s of data for the system at $\gamma = 2.19$, $q = 0.48$ and $\phi_t = 0.33$ is shown with, in Figure 6.4b, the corresponding corrected COM trajectories for the subsets of small and large particles over the whole length of the data. It can be seen that the tracks for the small and large particles are closely related to each other, which is consistent with the fact that the interdiffusion of the two subsets must balance in order for there to be no net movement of particles for a system at equilibrium. The differing magnitude of the displacements for the two subsets arises from the mismatch in the number of large and small particles; a greater number of small particles are involved in the process and as such the interdiffusion current associated with them is smaller, again to balance the effect for large and small particles. The COM mean squared displacement, $\langle \delta \widetilde{R}_i^2(t) \rangle$, for the large and small particle subsets may then be calculated from the corrected COM tracks. As with the COM trajectories, $\langle \delta \widetilde{R}_i^2(t) \rangle$ for the large and small particles are related. This is a direct consequence of the relationship between the two COM coordinates, which follows from (6.8) and (6.9) as $\mathbf{R}(t) = c_a \mathbf{R}_a(t) + c_b \mathbf{R}_b(t)$. Therefore, the centre of mass mean squared displacements

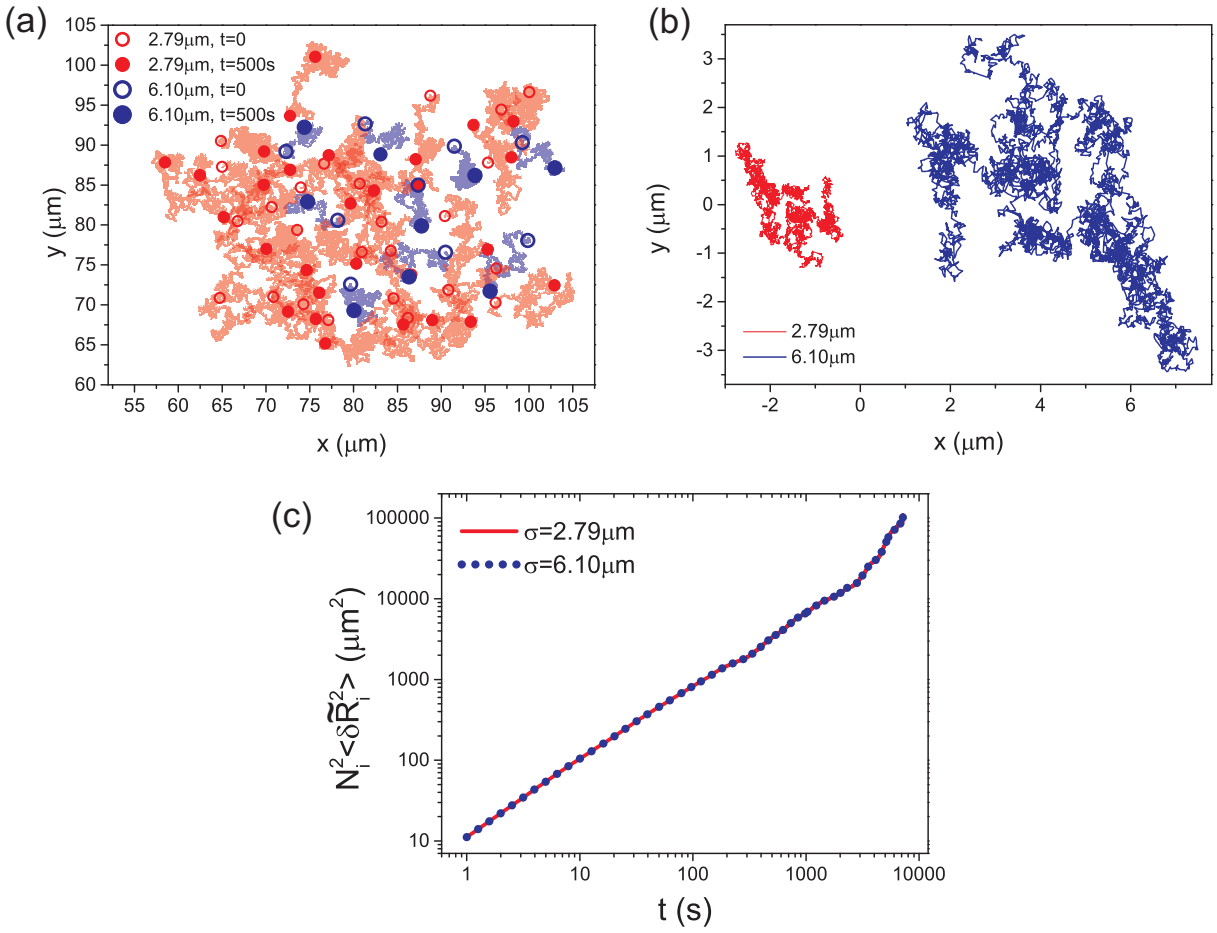

Figure 6.4: Diagrams to demonstrate the particle and centre of mass (COM) tracking process. (a) The trajectories of a subset of particles in a system at $\gamma = 2.19$ and $\phi_t = 0.33$ with the initial and final positions of the particles indicated. (b) COM trajectories for subsets of large and small particles relative to the COM trajectory of all particles. (c) The centre of mass MSD for the large and small particles scaled by the number of particles as described in Equation (6.26).

are coupled as

$$\begin{aligned}
\langle \delta \widetilde{R}_a^2(t) \rangle &= \langle [\widetilde{\mathbf{R}}_a(t) - \widetilde{\mathbf{R}}_a(0)]^2 \rangle \\
&= \langle [\{\mathbf{R}_a(t) - \mathbf{R}(t)\} - \{\mathbf{R}_a(0) - \mathbf{R}(0)\}]^2 \rangle \\
&= \left\langle \left[\left\{ \frac{1}{c_a}(\mathbf{R}(t) - c_b \mathbf{R}_b(t)) - \mathbf{R}(t) \right\} - \left\{ \frac{1}{c_a}(\mathbf{R}(0) - c_b \mathbf{R}_b(0)) - \mathbf{R}(0) \right\} \right]^2 \right\rangle \\
&= \left\langle \left[-\frac{c_b}{c_a} \{\mathbf{R}_b(t) - \mathbf{R}(t) - \mathbf{R}_b(0) + \mathbf{R}(0)\} \right]^2 \right\rangle = \frac{c_b^2}{c_a^2} \langle \delta \widetilde{R}_b^2(t) \rangle. \qquad (6.26)
\end{aligned}$$

This allows the interdiffusion MSD to be calculated from either component, and it also provides a useful consistency check on the results obtained, as shown in Figure 6.4c. Note that the calculation of $\langle \delta \widetilde{R}_i^2(t) \rangle$ is the same as for the self-MSD, however each subset only contributes one

trajectory and as such the statistics are much poorer than for the corresponding self properties.

One way in which statistics may be improved is by varying the size of the subset used, as this allows for multiple equivalently sized subsets to be tagged in the same initial frame and subsequently averaged. In addition to improving the statistics, this also probes finite size effects expected to arise due to the collective nature of interdiffusion. Therefore, $\langle \delta \widetilde{R}_i^2(t) \rangle$ is calculated for the largest area over which all the particles may be tracked over all times, and subsequently also for this area split into 1, 2, 4, 6, 8 and 16 equal areas. In all cases, exactly the same particle trajectories are used; it is simply the number of these trajectories used for the calculation of the COM coordinates which differs. Importantly, it is ensured that the smallest subsets used still include multiple particles as collective properties are studied. Hence, for lower ϕ_t only smaller numbers of larger subsets can be considered.

In Figure 6.5, examples of the interdiffusion MSDs calculated directly from $\langle \delta \widetilde{R}_i^2(t) \rangle$ (Equation (6.25)) are shown. These are compared with the interdiffusion MSD calculated from the Darken equation, which in direct analogy to the interdiffusion coefficient from the Darken equation (Equation (6.1)), may be calculated from a linear combination of the self-MSDs as

$$D_{ab}(t) = \Phi \lim_{t \to \infty} \frac{\langle \delta R^2(t) \rangle_{\text{int,Darken}}}{4t}, \tag{6.27}$$

with

$$\langle \delta R^2(t) \rangle_{\text{int,Darken}} = c_a \langle \delta r_b^2(t) \rangle + c_b \langle \delta r_a^2(t) \rangle. \tag{6.28}$$

Here, $\langle \delta r_i^2(t) \rangle$ is the self-MSD of one component (see Chapter 4). The interdiffusive behaviour of the system at large size ratio ($\gamma = 2.19$ and $q = 0.48$) is compared to both small size ratio systems with either a similar number concentration ($\gamma = 1.45$ and $q = 0.37$) or a similar area fraction ratio ($\gamma = 1.45$ and $q = 0.50$). Each line is related to a different number of tagged subsets as indicated in the legend in Figure 6.5a, with the size of the subset scaling inversely with the number of boxes.

Figure 6.5 clearly shows that while all interdiffusion MSDs show very good agreement at short times, there are deviations of $\langle \delta R^2(t) \rangle$ from the Darken equation at long times. The size of these deviations are seen to depend upon the composition and size ratio, with much larger deviations for the system at $\gamma = 2.19$. Here, at long times, the centre of mass MSD is no

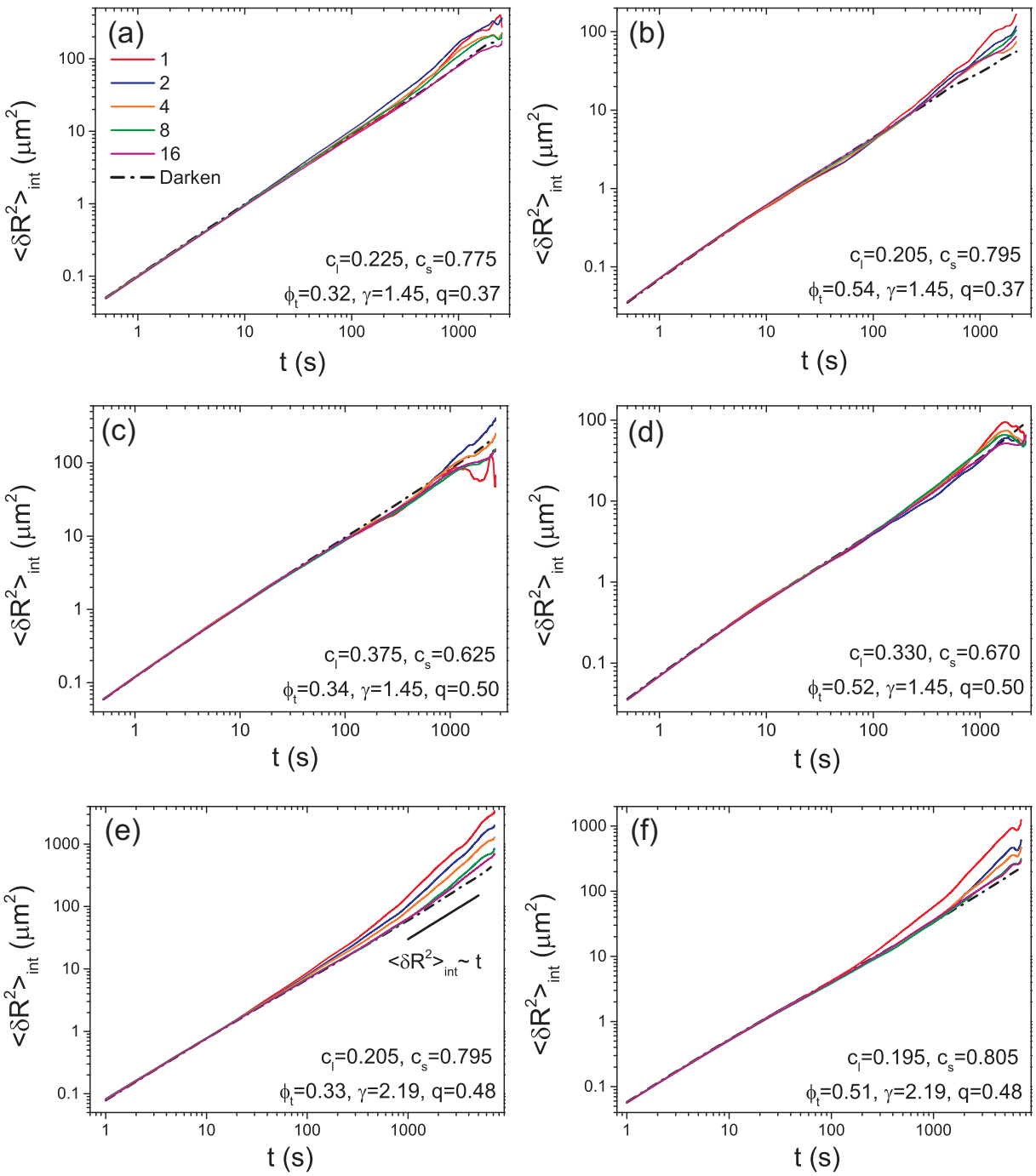

Figure 6.5: The interdiffusion mean squared displacement, $\langle \delta R^2(t) \rangle_{\rm int}$, calculated from both $\langle \delta \widetilde{R_i}^2(t) \rangle$ (Equation (6.25)) and from the Darken approximation (Equation (6.28)). Results are shown for systems with $\gamma = 1.45$ and $q \approx 0.37$ ((a) and (b)), $\gamma = 1.45$ and $q \approx 0.50$ ((c) and (d), and $\gamma = 2.19$ and $q \approx 0.48$ ((e) and (f)). (a),(c) and (e) show MSDs at $\phi_t \approx 0.3$ and (b),(d) and (f) at $\phi_t \approx 0.5$. The legend in (a) indicates the number of particle subsets used to calculate the COM MSDs in all panels.

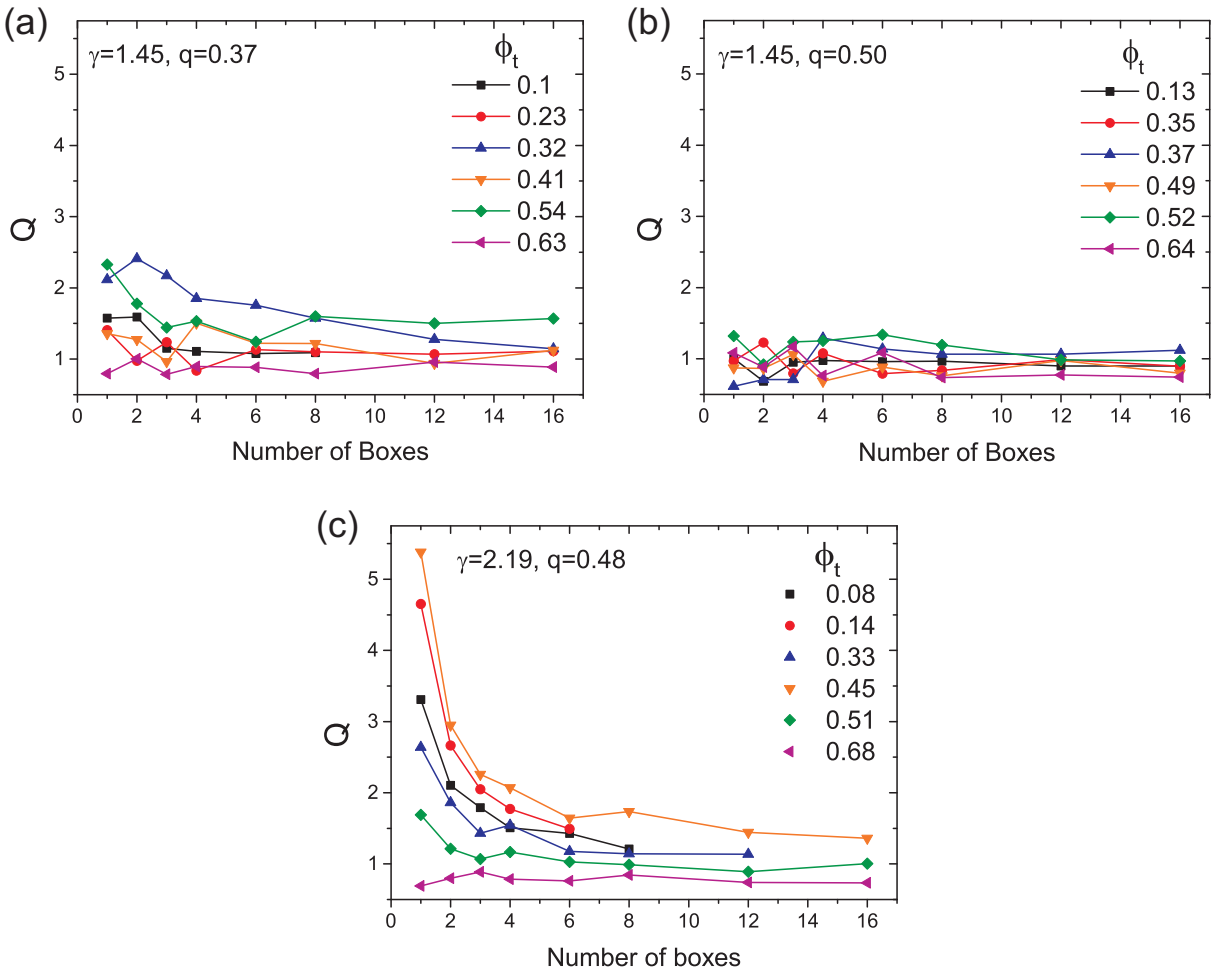

Figure 6.6: The ratio Q (Equation (6.29)), used to quantify deviations of the centre of mass MSD from the Darken equation, as a function of the number of boxes used. Results are shown for systems with (a) $\gamma = 1.45$ and $q = 0.37$, (b) $\gamma = 1.45$ and $q = 0.50$, and (c) $\gamma = 2.19$ and $q = 0.48$.

longer linear with time. This is in spite of the fact that the self-MSDs of both the large and small particles are linear at long times (see Chapter 4) as demonstrated by the linear long-time regime of the MSD calculated from the Darken approximation (Equation (6.28)). The size of this deviation is clearly dependent upon the size ratio, composition and size of the subset used. The dependence on the latter suggests it arises due to collective phenomena, as the change in subset size leads to a change in the number of particles for which the collective dynamics is studied [132]. To quantify the deviations with the Darken approximation more thoroughly, the ratio

$$Q = \frac{\langle \delta R^2(t) \rangle_{\text{int,COM}}}{\langle \delta R^2(t) \rangle_{\text{int,Darken}}} \tag{6.29}$$

is considered at $t = 1000$ s and shown in Figure 6.6. Here, the differing long-time behaviour of the systems is more clearly demonstrated. Firstly, the size of the deviations for the system at $\gamma = 2.19$ are generally larger than those for the systems at $\gamma = 1.45$. A comparison of Figure 6.6a and b, however, shows that the value of the ratio Q also depends upon the composition, with larger values of Q seen for the system with $q = 0.37$ compared to that with $q = 0.50$. Figure 6.6c also demonstrates that there is possibly some dependence upon the value of ϕ_t, with larger deviations seen for lower total area fractions.

The origin of the deviation from the Darken equation is currently unclear. While it cannot be discounted that it arises from the poorer statistics associated with the calculation of the COM MSD, it seems unlikely that this is the sole cause due to the fact that the same behaviour is not observed in the results for all systems considered. Additionally, there is no evidence that the effect is caused by errors in the tracking procedure or calculation of particle trajectories in light of the expected behaviour of the self-MSD. One possible explanation is that while the Darken equation assumes there to be no cross-correlations, the structural behaviour of the system with $\gamma = 2.19$ clearly indicates that the negative nonadditivity leads to significant cross-correlations. Thus it is perhaps unsurprising that the Darken equation does not hold in this case. Also, as collective diffusion is expected to be faster than self diffusion, it is possible that the superlinear behaviour observed in Figure 6.5 is an intermediate time regime, which represents the crossover to another diffusive regime at longer times with a diffusion coefficient greater than that predicted by the Darken equation.

6.5 Conclusions

In conclusion, interdiffusion in a range of binary colloidal fluids has been studied. The rate of interdiffusion is considered in terms of both thermodynamic and kinetic factors with the dependence of the interdiffusive behaviour upon the size ratio γ, composition q and total area fraction ϕ_t probed. Calculation of the thermodynamic factor, Φ, from $S_{cc}(k \to 0)$ using an analysis of concentration fluctuations is used to demonstrate that the thermodynamic drive for interdiffusion is larger for the system at large size ratio. This is attributed to the structural ordering caused by the higher non-additivity in these systems. The interdiffusion mean squared displacement (MSD) is then measured via both the Darken equation, and from the centre of

mass MSD. The Darken equation is found to describe the behaviour well at short times, but at long times significant discrepancies are seen between the interdiffusion MSDs calculated by different routes. This indicates that the Darken equation does not fully describe the interdiffusive behaviour of these systems and that, for the large size ratio system in particular, non-ideal mixing effects are important.

Acknowledgements

This work was performed in collaboration with Jürgen Horbach and Dirk Aarts. Lia Verhoeff and Michael Juniper are thanked for useful discussions.

Chapter 7

Melting of quasi-two-dimensional colloidal hard spheres

ABSTRACT

In this Chapter, the melting of quasi-two-dimensional colloidal hard spheres is studied by considering a tilted monolayer of particles in sedimentation-diffusion equilibrium. This allows the full phase behaviour to be probed in one sample. The density profile and the equation of state are determined and both quantities display a discontinuity upon increasing area fraction. This indicates a first order transition and coexistence region and hence, an interface. The interface between ordered and disordered phases is subsequently located using the argument of the bond-orientational order parameter and fluctuations of the interface are analysed using capillary wave theory. Height-height correlations are calculated and used to quantify both the size of the coexistence gap and the anisotropic stiffness of the interface.

7.1 Introduction

The spatial dimensionality of a system can have a profound effect upon its physical properties. This may be observed in both structural and dynamic phenomena, with examples including the absence of long-range positional order in a two-dimensional (2D) crystal [13] and the differing diffusive behaviour seen in one and two dimensions [214, 215]. Another notable and widely studied example is the melting transition in 2D. Here, unlike melting in 3D, it is proposed that an additional hexatic phase exists between the 2D liquid and crystalline phases [15–17]. This phase is characterised by short-ranged positional and quasi-long-ranged orientational order, with similar phases seen in smectic phases of liquid crystals and polydisperse colloidal disks [216,217].

The Kosterlitz-Thouless-Halperin-Nelson-Young (KTHNY) theory [15–17] describes scenarios by which the 2D crystalline phase melts to become a disordered liquid. One such scenario involves two continuous phase transitions, via an intermediate hexatic phase, with the increasing disorder upon melting described in terms of the unbinding of topological defects. More specifically, in the first step, the unbinding of dislocation pairs changes the 2D crystal with long-range orientational and quasi-long-ranged positional order into the hexatic phase, which has long-range orientational and short-ranged positional order. This is followed by the transition to a liquid which possesses only short-ranged orientational and positional order due to the unbinding of dislocations into isolated disclinations. A number of alternative scenarios have, however, been proposed, for example, that melting is via a single solid-fluid transition [218]. Also, evidence from simulations suggest that the transition may depend very sensitively upon specific properties of the system. This has been studied in detail for the case of the pair potential [219, 220], but has also been considered with respect to out-of plane fluctuations [88], finite-size effects, pinned particles [221,222] or vacancies [223]. For experimental systems, many aspects of KTHNY theory, including the continuous nature of the two phase transitions, have been observed in two-dimensional systems of super-paramagnetic colloids interacting via a soft potential [64, 224, 225]. Nevertheless, evidence for a range of alternative scenarios has been seen in other experimental systems, for instance, those involving microgel particles [226,227] or particles interacting via a Yukawa potential [120] or a short ranged repulsion [126,228].

The nature of the melting transition for the simplest possible interacting system in 2D, hard disks, has for some time been unclear, despite the fact that the phase behaviour of these

systems was first considered over 50 years ago [74, 229–234]. Recent simulations have shown that, in contrast to the KTHNY scenario, melting occurs via two steps where the transition from crystal to hexatic is continuous but that from hexatic to liquid is first order [89, 219, 234]. This first order transition is seen to persist even in the quasi-two-dimensional systems realisable experimentally [88], but the nature of the transition for an experimental model hard disk system has yet to be confirmed.

In this Chapter, melting of a quasi-two-dimensional colloidal hard sphere system is studied by considering the sedimentation-diffusion equilibrium in a monolayer of particles tilted by a small angle with respect to the horizontal. The behaviour of the system is probed by systematically varying the tilt angle. First, the density profile and the equation of state are measured, where in both cases a discontinuity indicates the presence of a coexistence gap and hence an interface. This interface between an ordered and disordered phase is subsequently located by a consideration of the argument of the bond-orientational order parameter. Furthermore, the fluctuations of this interface are analysed using capillary wave theory to quantify both the size of the coexistence gap and the anisotropic stiffness of the interface.

7.2 Theory

7.2.1 The KTHNY scenario for two-dimensional melting

The KTHNY scenario [15–17], predicts that a two-dimensional crystal melts to a liquid via two consecutive continuous transitions involving an intermediate hexatic phase. These transitions are driven by the unbinding of topological defects, and the key types of defects found in the different phases are dislocation pairs, dislocations and disclinations, which are illustrated in Figure 7.1.

In 2D, crystalline states do not exhibit the long-ranged positional order seen in 3D due to long-wavelength thermal fluctuations [13]. They do, however, possess positional order that is much longer ranged than that in liquids, combined with long-ranged orientational order. Figure 7.1 demonstrates that the only type of defect consistent with this is a dislocation pair, shown in Figure 7.1a, which is comprised of two five-fold and two-seven fold coordinated particles. The diagram clearly shows that the presence of a dislocation pair in a crystal does not disrupt the positional or orientational order of the crystal. KTHNY theory suggest that the crystalline

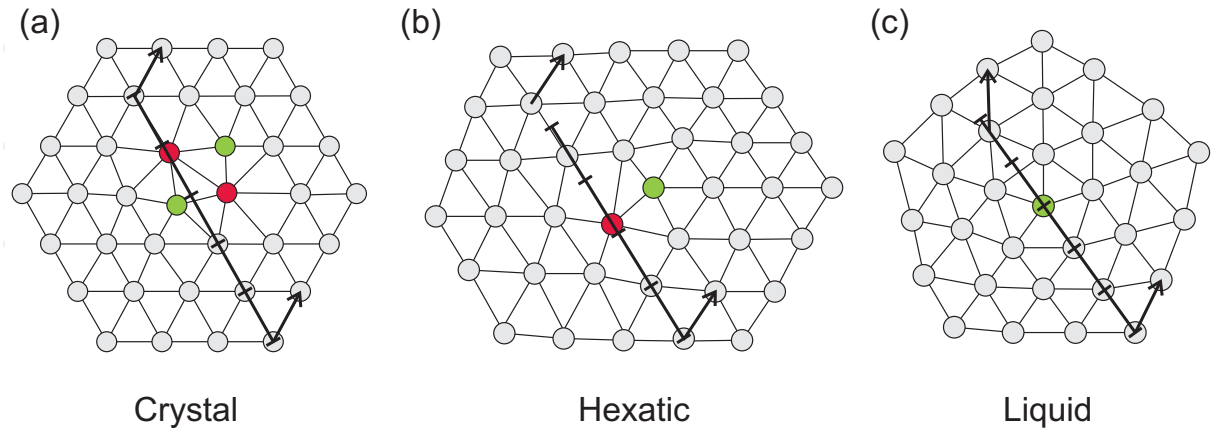

Figure 7.1: An illustration of the defects seen in the melting of 2D crystals: (a) a dislocation pair ; (b) a dislocation; and (c) a 5-fold disclination. Particles coloured red are those with seven nearest neighbours and particles coloured green are those with five nearest neighbours. Arrows indicate the bond-orientation on each side of the defect and lines mark the particle positions expected for systems with positional order.

system melts via a two-step process where the first step is a continuous transition associated with the unbinding of a dislocation pair to form isolated dislocations. A dislocation, consisting of a five-fold and a seven-fold coordinated particle, is shown in Figure 7.1b, and clearly leads to a loss of positional order but retention of orientational order. The resulting hexatic phase is therefore characterised by short-ranged positional order and quasi-long-ranged orientational order. In the second step, there is another continuous phase transition from the hexatic to the liquid phase. This transition is associated with the unbinding of dislocations to form isolated five- and seven-fold disclinations (see Figure 7.1c) which disrupt the system with respect to both the positional and orientational order. The resulting liquid phase thus has only short-ranged positional and orientational order.

To characterise the liquid, hexatic and crystal phases, order parameters and correlation functions that quantify the orientational and positional order are required. The positional order parameter may be defined as [235]

$$\rho_G(\mathbf{r}) = \exp(i\mathbf{G}\cdot\mathbf{r}), \tag{7.1}$$

and the corresponding positional correlation function as [64]

$$g_G(r) = \langle \rho_G(\mathbf{r})\rho_G(\mathbf{0})\rangle, \tag{7.2}$$

where $\mathbf{G}$ is a reciprocal lattice vector and r is the distance between two particles. This correlation function is predicted to decay algebraically for a crystal, but exponentially for both the hexatic and liquid phases [235]. The bond-orientational order is quantified by the bond-orientational order parameter, $\psi_{6,i}$, as

$$\psi_{6,i} = \frac{1}{n}\sum_{j=1}^{n}\exp(i6\theta_{ij}), \tag{7.3}$$

where n is the number of nearest neighbours and θ_{ij} is the angle between the vector connecting the central particle, i, with neighbouring particles, j, and a fixed reference axis. This quantifies the degree to which the neighbouring particles adopt a regular hexagonal position, with the modulus equal to unity for perfectly hexagonal order [236]. The range of the bond-orientational order is quantified by the bond-orientational correlation function

$$g_6(r) = \langle\psi_{6,i}(\mathbf{r})\psi_{6,i}(\mathbf{0})\rangle. \tag{7.4}$$

In the crystal $g_6(r)$ attains a constant value at large r, but in contrast to this decays algebraically in the hexatic phase, with $g_6(r) \sim r^{-1/4}$ at the transition between the hexatic and liquid [64]. In the liquid, the short-ranged orientational order leads to an exponential decay of $g_6(r)$.

It is also possible to use dynamic criteria to distinguish between the liquid, hexatic and crystal [224]. These are particularly useful for the consideration of experimental systems imaged over a finite distance for a long time. Firstly, an expression similar to Equation (7.4) can be used which instead considers the variation in the value of $\psi_{6,i}$ with time, as

$$g_6(t) = \langle\psi_{6,i}(t)\psi_{6,i}(0)\rangle. \tag{7.5}$$

For long times, $g_6(t)$ tends towards a constant for the crystal phase, decays algebraically in the hexatic phase and as $g_6(t) \sim t^{-1/8}$ at the hexatic-liquid transition [235], and finally exponentially in the liquid phase. Additionally, a modified Lindemann parameter, $\gamma_L(t)$ [237], may be considered where

$$\gamma_L(t) = \frac{\langle(\Delta\mathbf{r_i}(t) - \Delta\mathbf{r_j}(t))^2\rangle}{2a^2}, \tag{7.6}$$

with a the lattice constant and $\Delta\mathbf{r_i}(\mathbf{t}) = \mathbf{r}_i(t) - \mathbf{r}_i(0)$. As such, $\gamma_L(t)$ considers the mean square

displacement of a particle relative to its nearest neighbours. This parameter diverges in the liquid and hexatic phases, while tending to a constant value in the crystalline phase [224].

7.2.2 Sedimentation-diffusion equilibrium

A system of colloidal particles under gravity will establish a sedimentation-diffusion equilibrium in which the flux of particles due to gravity is opposed by a diffusive flux driven by concentration gradients [171]. This implies that at each height, the gravitational force must be balanced by the osmotic pressure per unit area, which can be used to measure the number density profile, $\rho(z)$, and subsequently the equation of state [238]. Here, the sedimentation-diffusion equilibrium considered is that of a 2D system tilted with respect to the horizontal by an angle, α.

At a certain height, z, the osmotic pressure, $\Pi(z)$, is the integral of the weight supported at that point,

$$\Pi(z) = \int_z^\infty m^* g \sin\alpha \rho(z') \mathrm{d}z', \tag{7.7}$$

where m^* is the buoyant mass. This can be rewritten in terms of the equation of state as

$$\begin{aligned} \frac{\Pi(z)}{\rho(z) k_\mathrm{B} T} &= \frac{1}{\rho(z) h_{g\|}} \int_z^\infty \rho(z') \mathrm{d}z' \\ &= \frac{1}{\phi(z) h_{g\|}} \int_z^\infty \phi(z') \mathrm{d}z'. \end{aligned} \tag{7.8}$$

Here $h_{g\|} = k_\mathrm{B}T/(m^* g \sin\alpha)$ is the in-plane gravitational height. The second equality arises from the link between the number density, $\rho(z)$, and the area fraction, $\phi(z)$, via $\phi(z) = \rho(z)\pi\sigma^2/4A$ where A is the area of the system. Using the scaled particle theory expression for the equation of state (Equation (3.12)), which was shown to be an excellent description of our system in Chapter 3, the following expression for $\phi(z)$ is obtained:

$$\frac{1}{(1-\phi(z))^2} = \frac{1}{\phi(z) h_{g\|}} \int_z^\infty \phi(z') \mathrm{d}z'. \tag{7.9}$$

It is also possible to find the equilibrium density profile for the system by solving this equation iteratively. Note that in the following, the term 'density profile' refers to the expression in terms of the area fraction, $\phi(z)$.

7.2.3 Capillary wave theory

The thermal fluctuations of a one-dimensional interface in a 2D system can be analysed using capillary wave theory [239–242]. Note that for clarity, the following derivation is discussed in terms of an interface between liquid and hexatic phases, as this is the interface relevant to this Chapter. The static fluctuation spectrum is given by [59, 241, 243]

$$\langle |A(k)|^2 \rangle = \frac{k_{\mathrm{B}}T}{L\Gamma(k^2 + L_c^{-2})}, \tag{7.10}$$

where $A(k)$ is the amplitude at wavevector $k = n2\pi/L$, with n an integer, L the length of the interface and $L_c = \sqrt{\Gamma/(\Delta\tilde{\rho}g)}$ the capillary length, with $\Delta\tilde{\rho} = \tilde{\rho}_{hex} - \tilde{\rho}_{liq}$ the difference in mass densities of the liquid and hexatic phases. The interfacial stiffness, Γ, depends upon both the interfacial tension γ and the second derivative of this quantity with respect to the orientation of the ordered phase, γ'', as $\Gamma = \gamma + \gamma''$. The anisotropy in the interfacial free energy is expected to be very small, however the presence of the second derivative can lead to large differences in the interfacial stiffness with the orientation of the ordered phase [244, 245].

The static spectrum (Equation (7.10)) is related to the real space height-height correlation function, $g_h(x)$, via a Fourier transform as

$$g_h(x) = \frac{k_{\mathrm{B}}T}{\Gamma L} \sum_k \frac{1}{(k^2 + L_c^{-2})} \exp(ikx). \tag{7.11}$$

This can be expressed in terms of sine and cosine functions and converted to an integral where it is assumed that $k_{min} = 0$ and $k_{max} = \infty$ [59]. By noting the symmetry of sine and cosine, the following expression for $g_h(x)$ is obtained:

$$\begin{aligned} g_h(x) &= \frac{k_{\mathrm{B}}T}{\pi\Gamma} \int_0^\infty \frac{1}{(k^2 + L_c^{-2})} \cos(kx)\mathrm{d}k \\ &= \frac{k_{\mathrm{B}}T}{2\Gamma} L_c \exp(-x/L_c). \end{aligned} \tag{7.12}$$

The correlation function depends upon the difference in mass densities of the two phases, $\Delta\tilde{\rho}$, via the capillary length, L_c, where $\Delta\tilde{\rho}$ is expressed in terms of mass densities as

$$\Delta\tilde{\rho} = \tilde{\rho}_{hex} - \tilde{\rho}_{liq} = \frac{(N_{hex} - N_{liq})m^*}{A}. \tag{7.13}$$

Here, N_j is the number of particles in phase j, A the area of the system, $m^* = \pi\sigma^3\Delta\tilde{\rho}_{p-s}/6$ the buoyant mass of a particle, with σ the particle diameter and $\Delta\tilde{\rho}_{p-s}$ the mass density difference between a particle and the solvent. The mass density difference between the hexatic and liquid phases, $\Delta\tilde{\rho}$, can be alternatively expressed in terms of the area fractions, ϕ, by noting that

$$\Delta\phi = \phi_{hex} - \phi_{liq} = \frac{(N_{hex} - N_{liq})\pi\sigma^2}{4A}. \tag{7.14}$$

Combining (7.13) and (7.14) thus leads to

$$\Delta\tilde{\rho} = \frac{2\Delta\phi\Delta\tilde{\rho}_{p-s}\sigma}{3}. \tag{7.15}$$

Importantly, this shows that a value of $\Delta\tilde{\rho}$ can be used to directly measure the width of the coexistence region, $\Delta\phi$.

7.3 Experimental methods and data analysis

7.3.1 Colloidal model system

The colloidal system used in this Chapter is the $\sigma = 2.79$ μm monodisperse system described in Section 2.3.1. Sample cells are prepared as described in Section 2.3.1 at a total packing fraction of $\phi_t \approx 0.15$ and are then placed upon the stage of the tilted microscopy set-up described in Section 2.3.2 as illustrated in Figure 7.2a. Samples are left to equilibrate until the number of particles imaged remains constant over many hours. For the initial equilibration this could take

α (°)	θ (°)	$h_{g\parallel}$ (μm)
0.56	46.2	7.00
0.44	45.5	8.89
0.35	30.0	11.2
0.25	58.7	15.7
0.22a	6.6	17.8
0.22b	33.5	17.8
0.083	20.9	48.4.
0.067	14.2	55.9

Table 7.1: Experimentally determined values of the tilt angle α, the average value of orientation of the ordered region, θ, and the gravitational height parallel to the plane, $h_{g\parallel}$. Note that two values of θ are reported for the system at $\alpha = 0.22°$, due to the presence of a grain boundary.

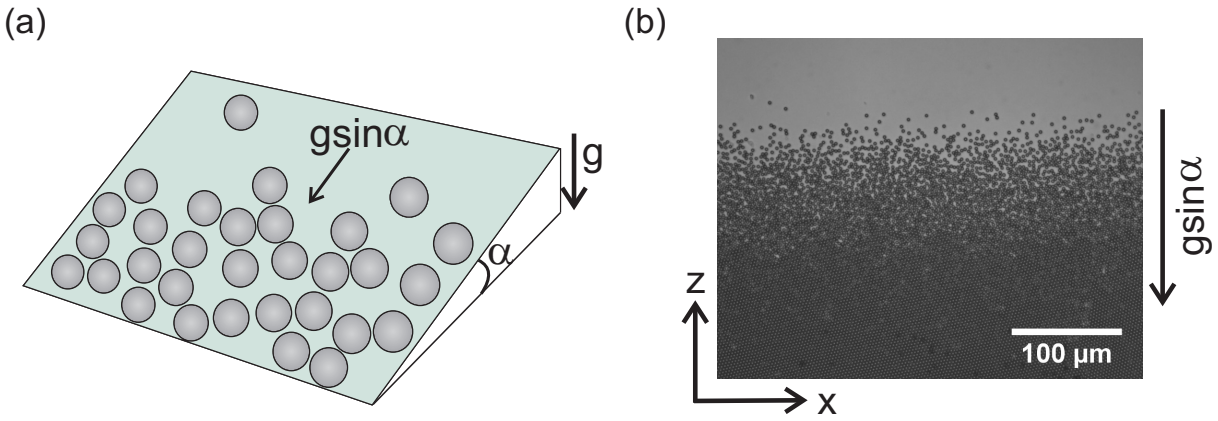

Figure 7.2: (a) A diagram to show the effect of tilting the sample by a small angle, α, and the resultant in-plane component of gravity. (b) An example of an experimental image for a tilt angle of $\alpha = 0.56°$.

up to a month. The angle at which the microscope is tilted is varied up to a maximum tilt angle, α, of approximately 1°. Gravitational heights perpendicular and parallel to the plane (see Section 2.3.2) may then be defined as

$$h_{g\perp} = \frac{k_{\mathrm{B}}T}{m^* g \cos\alpha} \quad \text{and} \quad h_{g\parallel} = \frac{k_{\mathrm{B}}T}{m^* g \sin\alpha}, \tag{7.16}$$

where g is the acceleration due to gravity and $m^* = \pi\sigma^3\Delta\tilde{\rho}_{p-s}/6$ the buoyant mass of the particle. For the system considered here, $\Delta\tilde{\rho}_{p-s} = 540$ kg m^{-3}. Even at the highest value of α, $h_{g\perp}$ is effectively unchanged from that of the flat system as $\cos\alpha \approx 1$ and the particles remain a monolayer confined to the 2D plane over the region of interest for all angles, α. The value of $h_{g\parallel}$ describes the extent to which particles may move up the tilted plane due to $k_{\mathrm{B}}T$ and varies substantially with tilt angle, from roughly two particle diameters for the largest α to approximately 20 particle diameters at the smallest α (see Table 7.1). The tilt angle, α, is initially estimated using a digital spirit level, which is sufficiently accurate to determine the relative change in angle between measurements but does not provide a good absolute measure of the tilt angle. The actual absolute angles are determined directly from the experimental density profiles (see Section 7.2.2).

The system is imaged using a 20× objective with images recorded on a PixeLINK CMOS camera at a resolution of 1280×1024 pixels. A typical image of the system at $\alpha = 0.56°$ is shown in Figure 7.2b. Here, the field of view is approximately 387×309 μm^2, which is significantly larger than in the experiments described previously. Following equilibration, data is recorded

at a rate of one frame per second for two hours. As the tilt angle, and therefore the in-plane gravitational height, is varied, the width of the interface increases and thus multiple datasets at differing z are taken to ensure that the whole density profile is imaged.

Standard particle tracking procedures [106] are used to obtain particle coordinates and tracks as in Section 2.3.3, with approximately $9000 - 14000$ particles found in each frame, dependent on the area fraction of the region considered. A consequence of the lower magnification used for these experiments is that it is more difficult to distinguish between particles and bright interstitials. Conditions on the length of tracks remove these interstitials and thus particle positions are extracted from the tracked data, rather than directly from the particle finding routine. Note that in the following discussion, the coordinate axes are defined such that the z axis runs parallel to the $\phi(z)$ gradient and the x axis perpendicular to it as shown in Figure 7.2b.

7.3.2 Density profiles

Density profiles, $\phi(z)$, are calculated for at least 1000 frames of data. These are computed from particle positions by splitting the data into 50 bins in the z direction, with a binsize of approximately 5.9 μm, and calculating the area fraction for each bin from the number of particles.

7.3.3 Interface localisation

To localise the interface between the ordered and disordered phase, first the hexagonal bond-orientational order parameter, $\psi_{6,i}$, introduced in Equation (7.3), is computed for all particles. To this end, the nearest neighbours of each particle are found using a Delauney triangulation and $\psi_{6,i}$ is then calculated as

$$\psi_{6,i} = \frac{1}{n}\sum_{j=1}^{n}\exp(i6\theta_{ij}), \tag{7.17}$$

with n the number of nearest neighbours and θ_{ij} the angle between a fixed reference axis and the vector connecting the central particle i with a neighbouring particle, j. The local orientation of each particle, θ_i, is then

$$\theta_i = \frac{\arg(\psi_{6,i})}{6}, \tag{7.18}$$

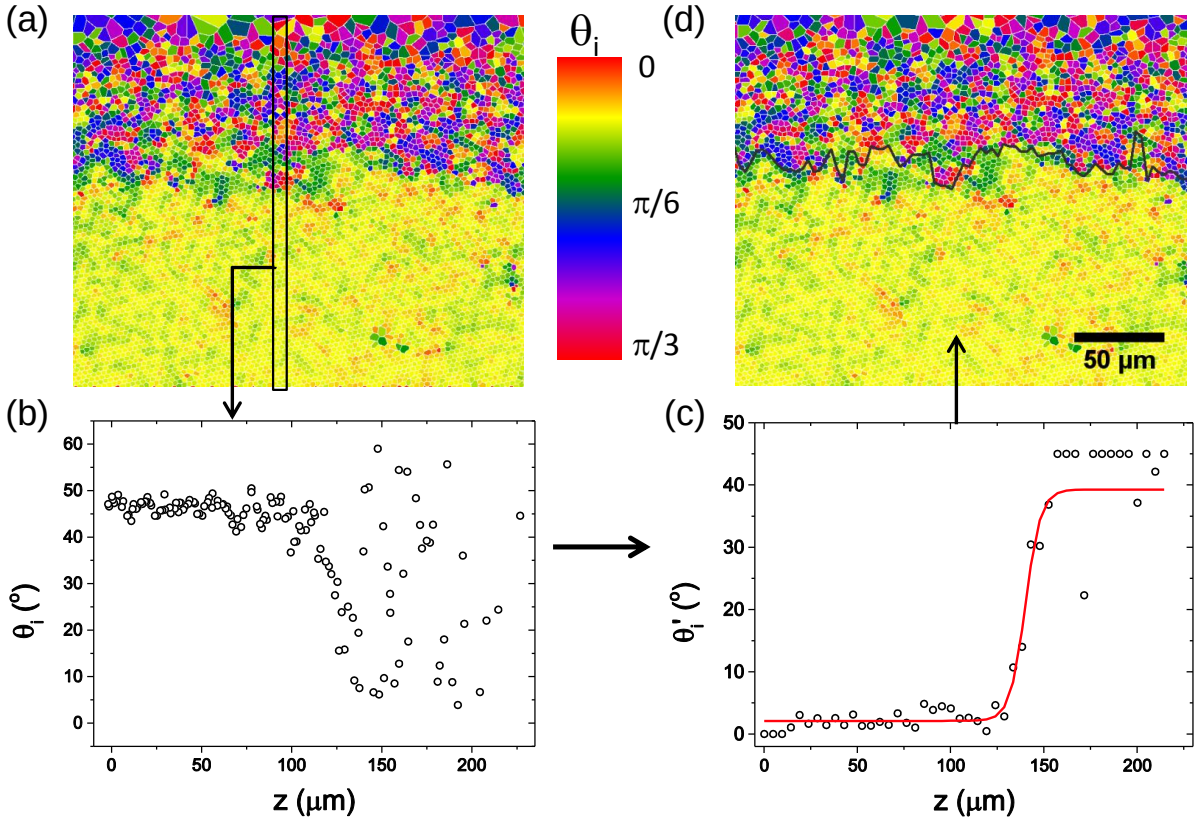

Figure 7.3: An illustration of the interface localisation process: (a) a Voronoi plot coloured by the value of θ_i for each particle; (b) the value of θ_i as a function of height for all particles in a single bin; (c) the tangent hyperbolic fit to values of $\theta_i' = |\theta_i - \theta|$; (d) the Voronoi plot with the located interface.

which varies between 0 and $\pi/3$ due to hexagonal symmetry. Figure 7.3a shows a Voronoi construction, where the Voronoi cells are coloured according to θ_i. Next, the variation of the local orientation θ_i as a function of z is used to localise the interface between disordered and ordered phases, as illustrated in Figure 7.3b and c. The values of θ_i are first split into 120 bins in the x direction, where the width of each bin is approximately the particle diameter. Plots of θ_i for each bin show a clear change at the interface from an approximately constant value, θ, indicative of the ordered phase, to a substantially varying value in the disordered phase as shown in Figure 7.3b. Now, θ_i is rescaled as $\theta_i' = |\theta_i - \theta|$ and the values of θ_i' are binned in z, with only the highest value of θ_i' kept for each bin. Importantly, the localisation of the interface requires no assumptions to be made about the values of individual particle properties in a certain phase, i.e. no arbitrary value of $\psi_{6,i}$ or θ_i is used to identify particles as belonging to either the ordered or disordered phase. Values of θ_i' as a function of z are then fitted with a tangent hyperbolic function (see Figure 7.3c) to find the interface as shown in Figure 7.3d.

The result of this analysis is the acquisition of the interface height as a function of position and time, $h_{exp}(x,t)$.

Note that Figure 7.3b shows that the random orientation of particles in the disordered phase can lead to regions with orientation equal to that of the ordered phase. Additionally, defects in the ordered phase may lead to θ_i values in the ordered phase that are dissimilar to θ. Thus, if these particles lie far from the interface, their orientation is rotated either to increase the mismatch between θ_i and θ (in the disordered phase) or so that $\theta_i = \theta$ (in the ordered phase), to ensure that interface localisation is accurate.

7.3.4 Height-height correlation function

Before using $h_{exp}(x,t)$ to compute the height-height correlation function, $g_h(x)$, it is first necessary to ensure that the average height per frame, $h_0(t) = \langle h_{exp}(x,t)\rangle_x$, does not drift. If $h_0(t)$ is calculated, however, it can be seen from Figure 7.4a, that only for the higher values of α is the average height per frame constant over the whole dataset. Thus, the experimental data as a function of time, $h_{exp}(x,t)$, is first corrected to $h(x,t) = h_{exp}(x,t) - h_0(t)$ so that the interface in each frame is centred around zero.

Additionally, the experimental data may display the effect of long-wavelength fluctuations that do not relax over the timescale of the measurement. These should be removed in order to only probe the fluctuations of the interface. To account for this, the average interface, $\bar{h}(x) = \langle h(x,t)\rangle_t$, is subtracted from the data, with $g_h(x)$ then calculated as

$$g_h(x) = \left\langle \left[h(x_0) - \bar{h}(x_0)\right]\left[h(x_0+x) - \bar{h}(x_0+x)\right]\right\rangle_{x_0,t}. \tag{7.19}$$

Clearly, the greater the number of frames used for the calculation of the average interface, the smoother it will be. This will substantially change the correlation function as fluctuations relative to the average interface will increase in size with the number of frames used to determine $\bar{h}(x)$. To determine how many frames should be used for the calculation of $\bar{h}(x)$ the ratio

$$Q(N) = \frac{\left\langle \bar{h}_N^2 \right\rangle_x}{\left\langle \bar{h}_1^2 \right\rangle_x} \tag{7.20}$$

is computed, where $\left\langle \bar{h}_N^2 \right\rangle_x$ and $\left\langle \bar{h}_1^2 \right\rangle_x$ are the mean squared widths of the average interface

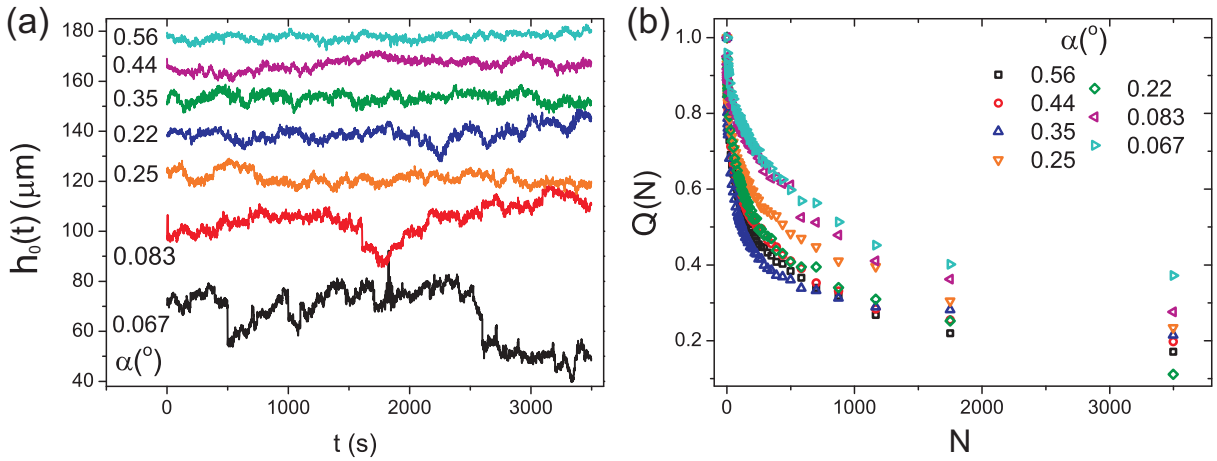

Figure 7.4: (a) The average interface height, $h_0(t)$, as a function of time for the seven values of α considered. Note that the values for interfaces at $\alpha = 0.083°$ and $\alpha = 0.067°$ have been vertically shifted for clarity. (b) The variation in the mean squared width of the averaged interface as a function of the number of frames, N, used for the average, quantified by the parameter Q (see Equation (7.20)) for systems at all values of α.

calculated over N frames and a single frame, respectively.

The variation of $Q(N)$ with the number of frames used for the average, $\langle \bar{h}_N^2 \rangle_x$, is shown in Figure 7.4b for all values of α. The value of Q drops significantly as the number of frames increases, but appears to tend towards a plateau value at the maximum number of frames considered, $N = 3500$. As such, the averaged interface subtracted from the data is that calculated from the full 3500 frames in order to prevent an artificial suppression of fluctuations.

7.4 Results and discussion

In Figure 7.5, typical microscopy images of the monolayer at two different tilt angles, $\alpha = 0.35°$ and $\alpha = 0.083°$ are shown. For all values of α, the images clearly show a gradient in ϕ with height, z. This results in a colloidal monolayer that varies in structure from that of a dilute liquid to a dense ordered phase. Simulations of hard disks suggest that the system should display a transition from liquid to crystal via an intermediate hexatic phase [88, 89], but this cannot be distinguished by eye. Nevertheless, the width of the regions over which these transitions occur clearly increases with decreasing tilt angle, although the precise location of the transition from dense fluid to hexatic to crystal can again not be determined by eye.

Next, the behaviour of the system with varying values of the tilt angle, α, is probed using

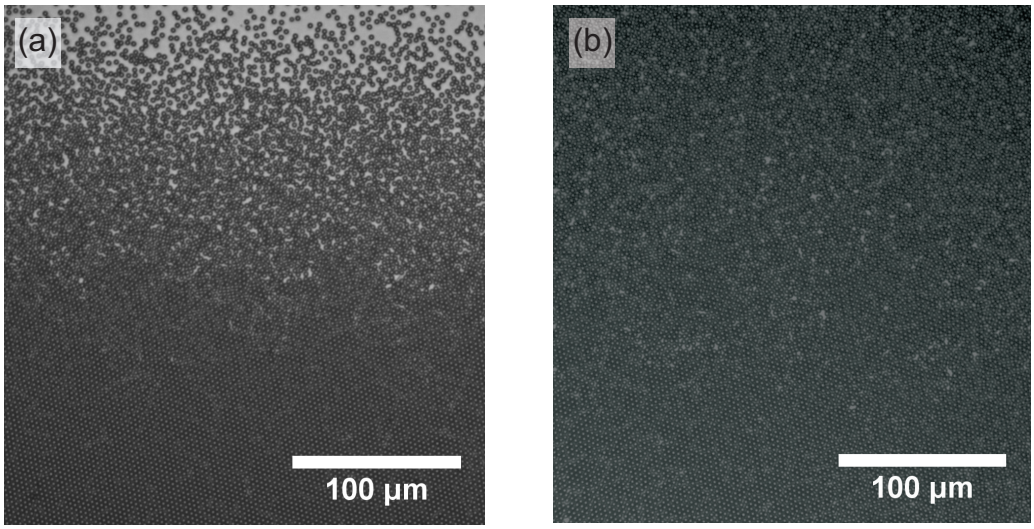

Figure 7.5: Typical experimental images for the system at (a) $\alpha = 0.35°$ and (b) $\alpha = 0.083°$. Note that in (b), only a small part of the full density range is shown.

the density profile, $\phi(z)$, which is calculated for the systems at all seven tilt angles. An example of the density profile for the system with $\alpha = 0.083°$ is shown in Figure 7.6a. Qualitatively, $\phi(z)$ decreases slowly at small z from a value of approximately $\phi(z) = 0.74$, before decreasing sharply to a value of $\phi(z) = 0$ for large z. Here, for this particular tilt angle, the full density profile is stretched out over a distance equivalent to nearly 360 particle diameters.

The equation of state may now be obtained according to Equation (7.9) if the in-plane gravitational height, $h_{g\|}$, is known. This depends upon the tilt angle, α, and as discussed in Section 7.3.1, the error on this value is relatively large as the tilt angle is measured only approximately using a digital spirit level. However, as the equation of state from scaled particle theory describes our experimental system well in the liquid range of ϕ, the tilt angle can be found from Equation (7.9). In particular Equation (7.9) is considered in the form

$$\frac{\Pi}{\rho k_{\mathrm{B}} T} \cdot h_{g\|} = \frac{h_{g\|}}{(1-\phi(z))^2} = \frac{1}{\phi(z)} \int_z^\infty \phi(z')\mathrm{d}z', \tag{7.21}$$

where the right hand side is directly determined from the experimental density profiles, and the left hand side is used as a fit, with $h_{g\|}$ the only fitting parameter. In Figure 7.6b an example of such a fit is shown for the density profile in Figure 7.6a. Qualitatively, the equation of state (multiplied by $h_{g\|}$) shows complimentary behaviour to that of $\phi(z)$, exhibiting a monotonic increase with ϕ, and the fit from scaled particle theory (Equation (7.21)) is clearly a good description of the data for $0 < \phi < 0.68$. Importantly, this allows for the tilt angle to be

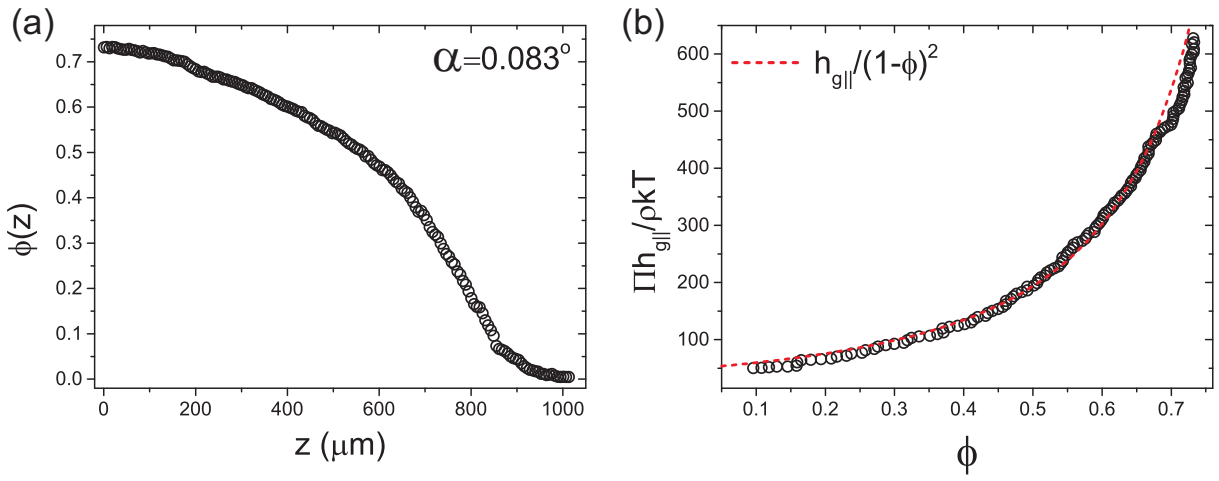

Figure 7.6: (a) The density profile, $\phi(z)$, and (b) the equation of state multiplied by $h_{g\|}$for the system with $\alpha = 0.083°$. The red line in (b) shows the fit according to Equation (7.21).

determined directly from the experimental data via

$$h_{g\|} = \frac{k_{\mathrm{B}}T}{m^* g \sin\alpha}, \tag{7.22}$$

which thus acts as a very sensitive internal calibration mechanism. The tilt angles obtained for all datasets are reported with the effective in-plane gravitational height in Table 7.1. Also evident in Figure 7.6b, is a discontinuity in the equation of state at $\phi \approx 0.68$. This is a signature of a first order transition, where the coexistence between two phases over a certain range of area fractions leads to a jump in the density profile. While the range of area fractions over which the jump is seen to occur is small, the agreement between Equation (7.21) and the data below the jump highlights this discontinuity.

This procedure is performed for all datasets, and thus the equation of state and the density profiles for all values of α may be rescaled by $h_{g\|}$ to fall onto one curve. This is shown in Figure 7.7. Here, for all systems the fit is seen to be a very good description of the data over values of ϕ characteristic of fluids. Strikingly, a discontinuity is now more clearly seen in both the density profile and the equation of state at $\phi \approx 0.70$, which thus corroborates the possibility of a first order phase transition. To estimate the width of the coexistence region, an empirical equation of state of the form $\Pi(\phi)/(\rho k_{\mathrm{B}}T) = a/(\phi_{cp} - \phi)$ is used to describe the behaviour at high ϕ [238]. Here, a is a constant and ϕ_{cp} is the area fraction at close packing. The fit is seen to be a reasonable description of the behaviour at higher area fractions and this clearly highlights the existence of a density gap as shown in the inset. Using the two expressions for the equation

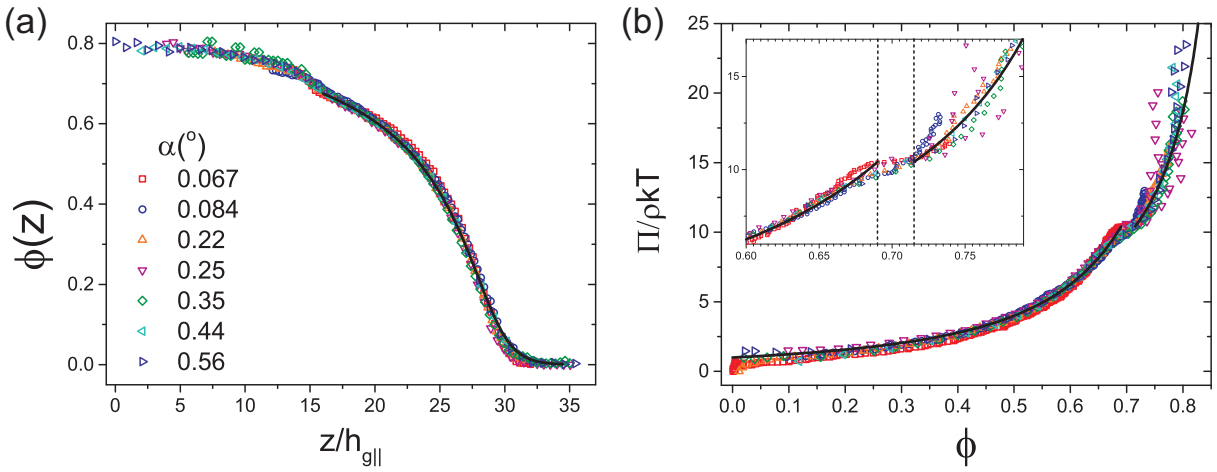

Figure 7.7: (a) The density profile, $\phi(z)$, for systems at a variety of tilt angles, α. The black line shows the prediction of scaled particle theory for the density profile, Equation (7.9). (b) The equation of state for systems at a variety of tilt angles, α, calculated by Equation (7.8). The black line for $\phi < 0.69$ shows the prediction of scaled particle theory (Equation (7.9)) and the line for $\phi > 0.715$ an empirical fit $\Pi/(\rho k_{\mathrm{B}}T) = a/(\phi_{cp} - \phi)$. The inset shows more clearly the behaviour of the equation of state in the region of the discontinuity. Here, the approximate range of area fractions of the discontinuity is indicated by dotted lines.

of state, an approximate density gap, $\Delta\phi \approx 0.025$ is found. Results from simulations suggest that the first order transition seen for hard disks is between the hexatic and liquid phases, with a density gap $\Delta\phi = 0.016$ [89]. This is remarkably similar to the approximation of the density gap found in our experiments. However, it should be noted that the error in the determination of the area fraction from microscopy can be relatively large, with small polydispersities or uncertainty in the particle radius leading to variations in ϕ comparable in size to our density gap [246]. Thus, another method by which the density gap may be determined, which is not based upon directly measuring ϕ, is highly desirable.

The jump in the density suggests that there is a well defined interface between the disordered and ordered phases of the system. This interface will display capillary fluctuations, which directly provide access to $\Delta\phi$ via Equations (7.12) and (7.15) without requiring an explicit measurement of ϕ. Thus, in order to localise the interface, properties of single particles are now considered. First, the local area fraction, ϕ_i, is calculated from the size of the corresponding Voronoi cell, and the modulus of $\psi_{6,i}$ for each particle, i, calculated from Equation (7.17). In Figure 7.8, a typical example of the Voronoi construction for the system at $\alpha = 0.56°$ is shown, where in panel (a) the cells have been coloured by local area fraction, ϕ_i, and in panel (b), by the modulus of $\psi_{6,i}$. A small section of the experimental image is also shown for comparison. In both

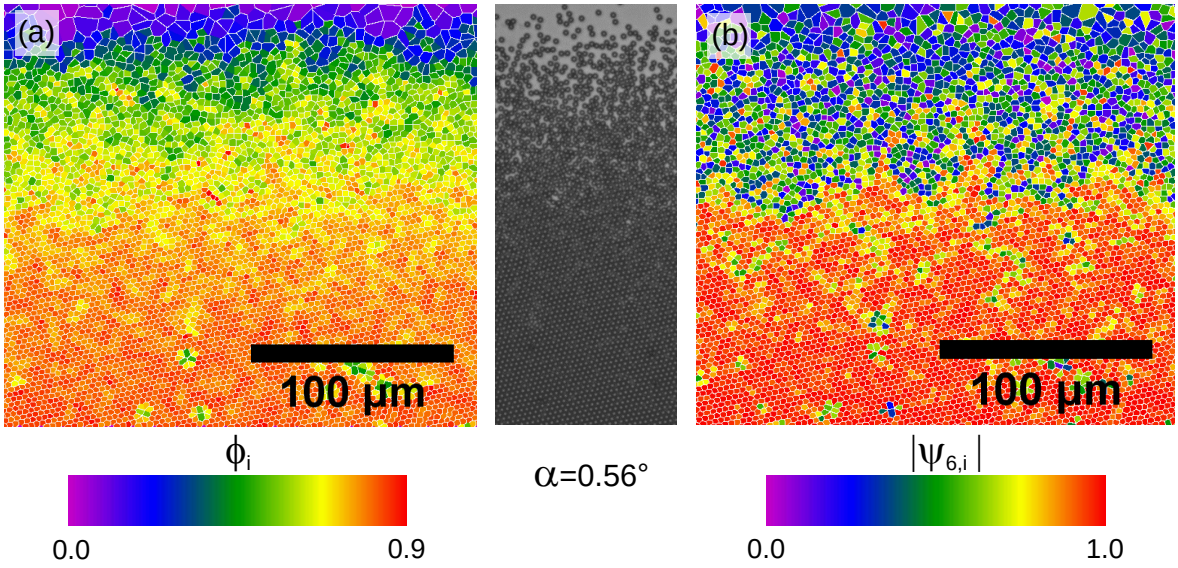

Figure 7.8: Typical Voronoi plots coloured with respect to (a) the local area fraction, ϕ_i, and (b) the modulus of $\psi_{6,i}$ as indicated in the colour scale. Also shown is a small section of the corresponding experimental image.

cases, the images show the expected general behaviour of both increasing ϕ_i and $|\psi_{6,i}|$ as the system changes from a disordered to ordered phase. Despite this, no clear interface is seen when the local area fraction is considered for a single image despite the clear jump in the density profile calculated from an average over many frames. While $|\psi_{6,i}|$ indicates more clearly the presence of an interface, the precise transition point is also not clear. This is perhaps unsurprising, as simulations suggest that it is the bond-orientational order, as quantified by $\theta_i = \arg(\psi_{6,i})/6$, that is the important parameter to distinguish between liquid and hexatic [219], and this information is not found in $|\psi_{6,i}|$ as the orientation is lost by taking the modulus.

In contrast to this, if the Voronoi cells are instead coloured with respect to θ_i, a clear interface between an ordered and disordered phase is seen for systems at all tilt angles, as illustrated in Figure 7.9. Here, the position of the interface as a function of x and t, determined as described in Section 7.3.3 is also shown. Interestingly, as α decreases, the width of the interface seen in Figure 7.9 clearly increases. While the disordered region clearly corresponds to the liquid phase, plots of θ_i do not distinguish between the hexatic and crystalline phases that comprise the ordered region. Simulation results [88, 89], however, suggest that the first order transition is between the liquid and the hexatic state.

To analyse the interface fluctuations quantitatively, the height-height correlation function,

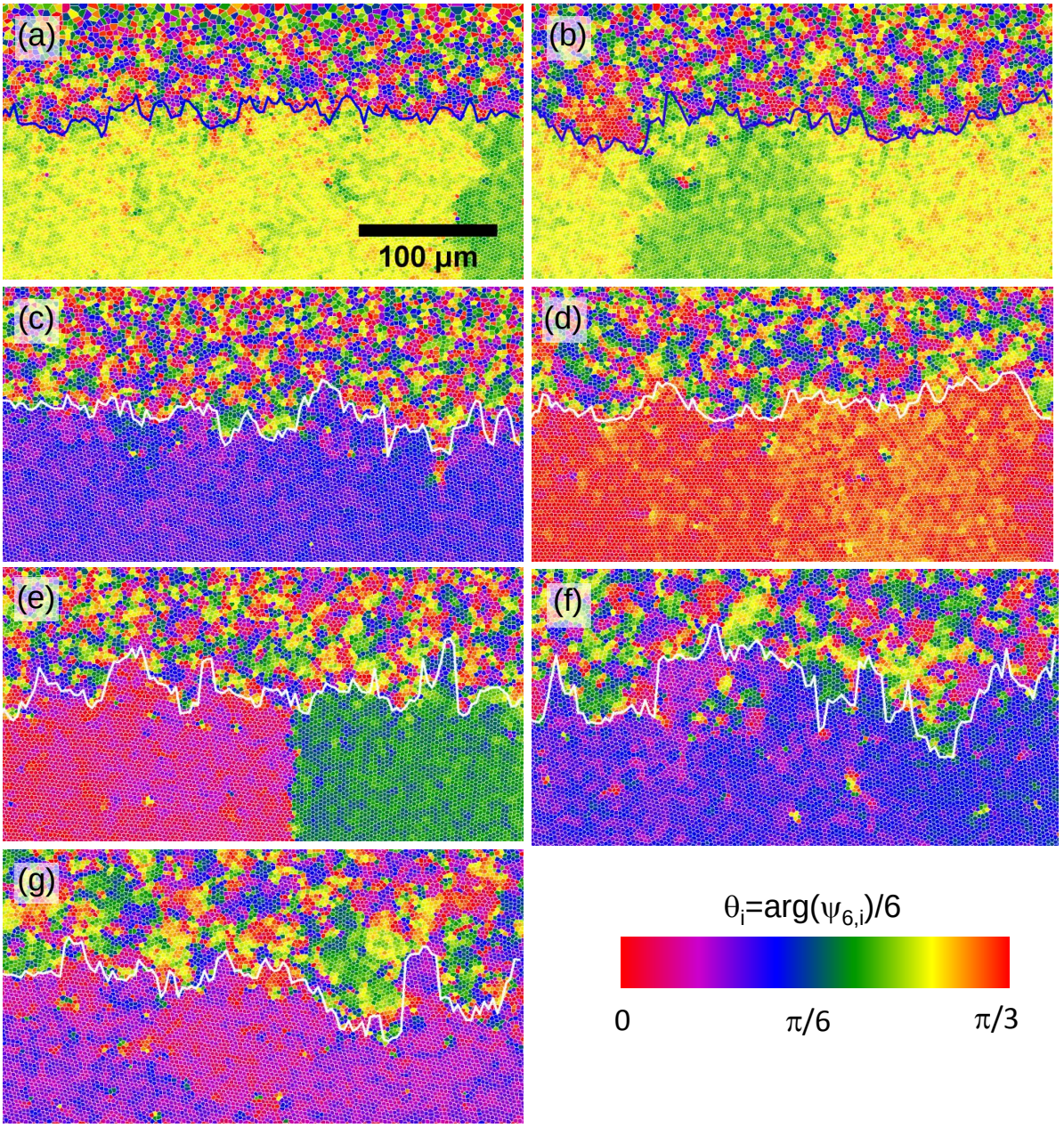

Figure 7.9: Typical Voronoi plots showing the variation of θ_i for systems with properties: (a) $\alpha = 0.56°$, $\theta = 46.2°$; (b) $\alpha = 0.44°$, $\theta = 45.5°$; (c) $\alpha = 0.35°$, $\theta = 30.0°$; (d) $\alpha = 0.25°$, $\theta = 58.7°$; (e) $\alpha = 0.22°$, $\theta = 6.6°$ and $\theta = 33.5°$ (due to the presence of a grain boundary); (f) $\alpha = 0.083°$, $\theta = 20.9°$; and (g) $\alpha = 0.067°$, $\theta = 14.2°$.

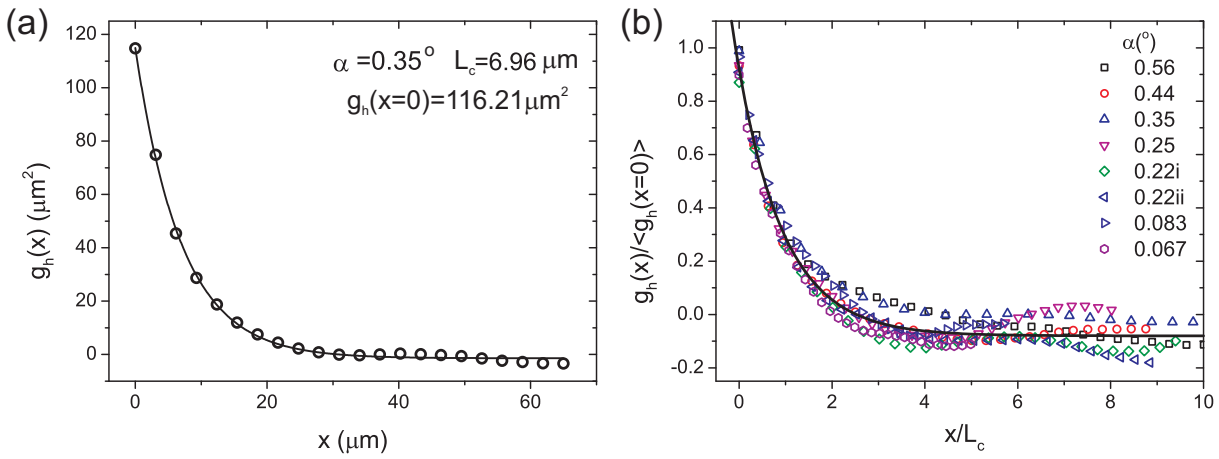

Figure 7.10: (a) The height-height correlation function for the system, $g_h(x)$, with $\alpha = 0.35°$ compared with a fit based upon Equation (7.23). (b) The rescaled height-height correlation functions for systems at all seven tilt angles. Here, the black line shows a fit to all data.

$g_h(x)$, is now computed according to Equation (7.19) as described in Section 7.3.4. In Figure 7.10a, $g_h(x)$ for the system at $\alpha = 0.35°$ is shown, which exhibits a monotonic decay and approaches zero at $x \approx 25$ μm. From capillary wave theory (Section 7.2.3), the height-height correlation function is given by

$$g_h(x) = \frac{k_B T}{2\Gamma} L_c \exp\left(-\frac{x}{L_c}\right), \tag{7.23}$$

which is fitted to the experimental data with

$$g_h(x=0) = \frac{k_B T}{2\Gamma} L_c = \frac{k_B T}{2\sqrt{\Gamma \Delta\tilde{\rho} g \sin\alpha}} \qquad \text{and} \qquad L_c = \sqrt{\frac{\Gamma}{\Delta\tilde{\rho} g \sin\alpha}} \tag{7.24}$$

as fitting parameters. This is shown in Figure 7.10a for the system at $\alpha = 0.35°$, where Equation (7.23) is seen to be a very good description of the experimental data. The same fit is then applied to the data at all values of α, and by rescaling as x/L_c and $g_h(x)/g_h(x=0)$, the data all fall onto a single master curve as shown in Figure 7.10b. Here, the fit to all data is also shown, which is seen to be a good description of all the measured correlation functions. The baseline of the fit deviates slightly from zero, which is an artefact of the subtraction of the averaged interface. This effect is somewhat larger for lower tilt angles, but importantly this has a very small effect upon the values for $g_h(x=0)$ and L_c as obtained from the fit.

The fitting parameters $g_h(x=0)$ and L_c are clearly related to the two unknown parameters; the interfacial stiffness, Γ, and the mass density difference, $\Delta\tilde{\rho}$ (see Equation (7.24)). While,

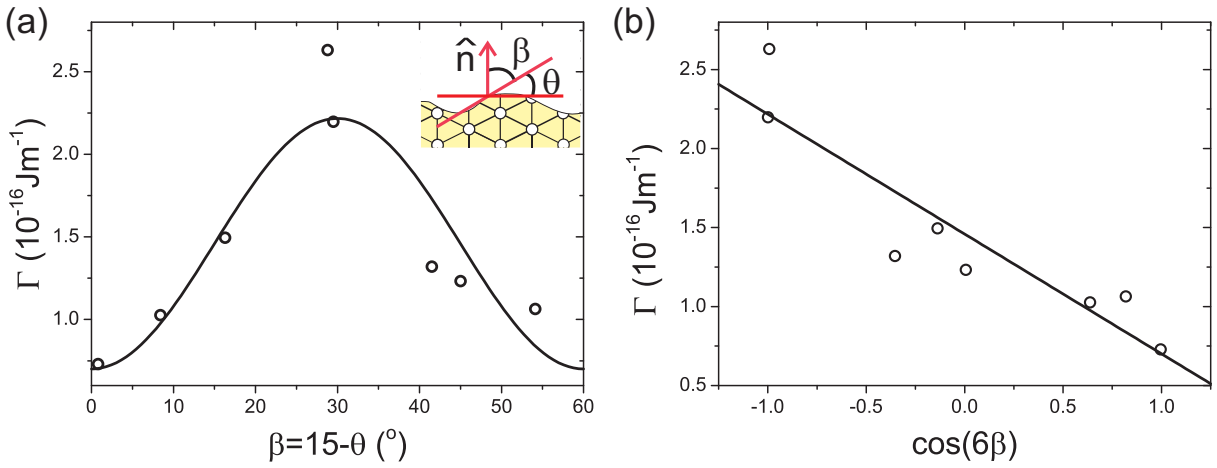

Figure 7.11: (a) Γ as a function of θ shown with a cosine fit. (b) The same values of Γ now as a linear plot against $\cos(6\beta)$. The inset in panel (a) shows the definition of β, θ and $\hat{n}$.

$\Delta\tilde{\rho}$ is expected to be strictly constant for all values of α due to the fact that it is related to the phase behaviour, Γ depends on the orientation of the ordered phase, θ, which is different for the datasets at different values of α (see Table 7.1 and Figure 7.9). Hence, to determine $\Delta\phi$ via $\Delta\tilde{\rho}$ it is first necessary to determine the anisotropy in the value of Γ. This can be extracted from the fitting parameters as $\Gamma = k_{\mathrm{B}}TL_c/(2g_h(x=0))$ and these values are shown in Figure 7.11a. The data is compared to an expression for the variation of Γ with the orientation of the ordered phase as [244, 245]

$$\Gamma = \gamma_0[1 - \epsilon\cos(6\beta)], \tag{7.25}$$

where γ_0 is the average value of the interfacial tension, β the orientation of the ordered phase with respect to $\hat{n}$ and ϵ a constant to account for the small anisotropy. Note that here, β, differs from our angle θ by 90° due to the definition of these angles with respect to different axes (see inset Figure 7.11a). Hence, when the angles are reduced to account for the six-fold symmetry of the ordered phase, they are related as $\beta = 15° - \theta$ and thus a straight line is obtained from a plot of Γ as a function of $\cos(6\beta)$. Note that the same fit is also shown in Figure 7.11a. Fitting to Equation (7.25) leads to values of $\epsilon = 0.52$ and $\gamma_0 = 1.46 \times 10^{-16}$ J m^{-1}. Here, Γ is approximately ten times smaller than the value found for grain boundaries in the same system [59] and the value of ϵ is similar to the value found for a 3D crystal-fluid interface [244].

Having established the anisotropy in Γ, it is finally possible to determine $\Delta\tilde{\rho}$ by plotting the fitting parameters, $g_h(x=0)$ and L_c against $\sqrt{1/\Gamma\sin\alpha}$ and $\sqrt{\Gamma/\sin\alpha}$, respectively, as shown

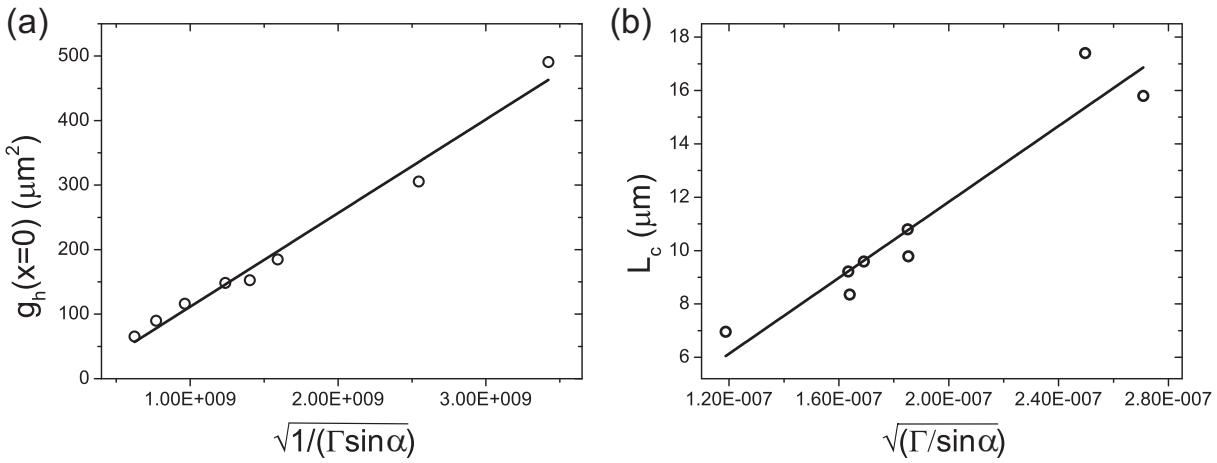

Figure 7.12: Plots used to determine $\Delta\tilde{\rho}$, exhibiting the linear dependence of (a) $g_h(x=0)$ with $\sqrt{1/\Gamma \sin\alpha}$ and (b) L_c with $\sqrt{\Gamma/\sin\alpha}$.

in Figure 7.12. In both cases a linear fit is a good description of the data and the slope is directly related to $\Delta\tilde{\rho}$ (Equation (7.24)). Importantly, the fact that the plots in Figure 7.12 are linear confirms that $g_h(x=0)$ and L_c scale with the tilt angle, α, consistent with Equation (7.24), which implies that $\Delta\tilde{\rho}$ is non-zero, and thus that there is a coexistence gap, $\Delta\phi$, indicating a first order transition between the liquid and ordered phase. The values of $\Delta\tilde{\rho}$ obtained from the slopes are converted to values of $\Delta\phi$ via Equation (7.15), with $\Delta\phi = 0.0204$ and $\Delta\phi = 0.0201$ found from the two plots. This is in remarkable agreement with both the approximate value found from the equations of state in Figure 7.7b, and with simulations of hard disks that predict a coexistence gap of $\Delta\phi = 0.016$ for the liquid-hexatic transition [88, 89].

The analysis considered here does not distinguish between the hexatic and crystal phases that form the ordered phase. As such, in future work the presence of both the hexatic and crystalline phases should be confirmed using suitable order parameters, for example $g_6(t)$ and the Lindemann parameter.

7.5 Conclusions

The melting of quasi-two-dimensional colloidal hard spheres has been studied by considering a monolayer of particles tilted by a small and variable angle with respect to the horizontal. This results in a density gradient over which the phase of the system changes from that of a disordered fluid to a dense ordered phase. A jump in the density profiles and equations of state for the

system indicates that the transition between the disordered and ordered phases occurs via a first-order phase transition with a coexistence gap, and hence that there is a clearly defined interface. The interface is localised by considering the variation of the argument of the bond-orientational order parameter. The fluctuations of the interface are subsequently analysed in terms of height-height correlation functions. The anisotropic interfacial stiffness and the coexistence gap in the density are both directly determined from the correlation functions, confirming the first-order nature of the transition between the liquid and ordered phase. It is yet to be determined whether a hexatic phase is involved.

Acknowledgements

This work was performed in collaboration with Joshua Abbott and Dirk Aarts. Jürgen Horbach, Lia Verhoeff, François Lavergne, Arran Curran and Michael Juniper are thanked for useful discussions.

Bibliography

[1] G. van Meer, D. R. Voelker, and G. W. Feigenson. Membrane lipids: where they are and how they behave. *Nat. Rev. Mol. Cell Biol.*, 9:112, 2008.

[2] A. K. Geim and K. S. Novoselov. The rise of graphene. *Nat. Mater.*, 6:183, 2007.

[3] S. Z. Butler, S. M. Hollen, L. Cao, and Y. Cui. Progress, challenges, and opportunities in two-dimensional materials beyond graphene. *ACS Nano*, 7:2898, 2013.

[4] G. A. Somorjai and Y. Li. *Introduction to surface chemistry and catalysis.* Wiley, 2010.

[5] J. M. Howe. *Interfaces in materials.* Wiley, 1997.

[6] D. E. Moncton and R. Pindak. Long-range order in two-and three-dimensional smectic-B liquid-crystal films. *Phys. Rev. Lett.*, 43:701, 1979.

[7] C. Harrison, Z. Cheng, S. Sethuraman, D. Huse, P. Chaikin, D. Vega, J. Sebastian, R. Register, and D. Adamson. Dynamics of pattern coarsening in a two-dimensional smectic system. *Phys. Rev. E*, 66:011706, 2002.

[8] T. Salditt, I. Koltover, J. O. Rädler, and C. R. Safinya. Two-dimensional smectic ordering of linear DNA chains in self-assembled DNA-cationic liposome mixtures. *Phys. Rev. Lett.*, 79:2582, 1997.

[9] L. Golubović and M. Golubović. Fluctuations of quasi-two-dimensional smectics intercalated between membranes in multilamellar phases of DNA-cationic lipid complexes. *Phys. Rev. Lett.*, 80:1, 1998.

[10] P. S. Dittrich and A. Manz. Lab-on-a-chip: microfluidics in drug discovery. *Nat. Rev. Drug Discov.*, 5:210, 2006.

[11] C. Simonnet and A. Groisman. Two-dimensional hydrodynamic focusing in a simple microfluidic device. *Appl. Phys. Lett.*, 87:114104, 2005.

[12] I. Shani, T. Beatus, R. H. Bar-Ziv, and T. Tlusty. Long-range orientational order in two-dimensional microfluidic dipoles. *Nat. Phys.*, 10:140, 2014.

[13] N. D. Mermin and H. Wagner. Absence of ferromagnetism or antiferromagnetism in one-or two-dimensional isotropic Heisenberg models. *Phys. Rev. Lett.*, 17:1133, 1966.

[14] B. J. Alder and T. E. Wainwright. Decay of the velocity autocorrelation function. *Phys. Rev. A*, 1:18, 1970.

[15] J. M. Kosterlitz and D. J. Thouless. Ordering, metastability and phase transitions in two-dimensional systems. *J. Phys. C*, 6:1181, 1973.

[16] D. R. Nelson and B. I. Halperin. Dislocation-mediated melting in two dimensions. *Phys. Rev. B*, 19:2457, 1979.

[17] A. P. Young. Melting and the vector Coulomb gas in two dimensions. *Phys. Rev. B*, 19:1855, 1979.

[18] A. Cacciuto, S. Auer, and D. Frenkel. Onset of heterogeneous crystal nucleation in colloidal suspensions. *Nature*, 428:404, 2004.

[19] S. Auer and D. Frenkel. Line tension controls wall-induced crystal nucleation in hard-sphere colloids. *Phys. Rev. Lett.*, 91:015703, 2003.

[20] J. P. Hoogenboom, P. Vergeer, and A. van Blaaderen. A real-space analysis of colloidal crystallization in a gravitational field at a flat bottom wall. *J. Chem. Phys.*, 119:3371, 2003.

[21] J. S. Rowlinson and B. Widom. *Molecular theory of capillarity*. Dover Publications Inc, 1982.

[22] D. H. Van Winkle and C. A. Murray. Layering in colloidal fluids near a smooth repulsive wall. *J. Chem. Phys.*, 89:3885, 1988.

[23] P. Tarazona and R. Evans. A simple density functional theory for inhomogeneous liquids. *Mol. Phys.*, 52:847, 2006.

[24] P. N. Pusey and W. Van Megen. Phase behaviour of concentrated suspensions of nearly hard colloidal spheres. *Nature*, 320:340, 1986.

[25] W. C. K. Poon. Colloids as big atoms. *Science*, 304:830, 2004.

[26] D. J. Kraft and J. Hilhorst. Patchy polymer colloids with tunable anisotropy dimensions. *J. Phys. Chem. B*, 115:7175, 2011.

[27] L. Rossi, S. Sacanna, W. T. M Irvine, and P. M. Chaikin. Cubic crystals from cubic colloids. *Soft Matter*, 7:4139, 2011.

[28] P. M. Johnson, C. M. van Kats, and A. Van Blaaderen. Synthesis of colloidal silica dumbbells. *Langmuir*, 21:11510, 2005.

[29] S. Sacanna, W. T. M. Irvine, P. M. Chaikin, and D. J. Pine. Lock and key colloids. *Nature*, 464:575, 2010.

[30] N. Chaturvedi, B. K.a Juluri, Q. Hao, Tony J. Huang, and D. Velegol. Simple fabrication of snowman-like colloids. *J. Colloid Interface Sci.*, 371:28, 2012.

[31] Y. Wu, Y. Li, L. Qin, F. Yang, and D. Wu. Narrow-dispersed melamineformaldehyde resin polymer colloidal spheres: preparation, size-control, modification, bioconjugation and particle formation mechanism. *J. Mater. Chem. B*, 1:204, 2013.

[32] B. Peng, E. Van Der Wee, A. Imhof, and A. Van Blaaderen. Synthesis of monodisperse, highly cross-linked, fluorescent PMMA particles by dispersion polymerization. *Langmuir*, 28:6776, 2012.

[33] W. Stöber, A. Fink, and E. Bohn. Controlled growth of monodisperse silica spheres in the micron size range. *J. Colloid Interface Sci.*, 69:62, 1968.

[34] T. Sugimoto, M. M. Khan, and A. Muramatsu. Preparation of monodisperse peanut-type a-Fe2O3 particles from condensed ferric hydroxide gel. *Colloids Surf., A*, 70:167, 1993.

[35] Y. Wang, Y. Wang, D. R. Breed, V. N. Manoharan, L. Feng, A. D. Hollingsworth, M. Weck, and D. J. Pine. Colloids with valence and specific directional bonding. *Nature*, 491:51, 2012.

[36] C. P. Royall, M. E. Leunissen, and A. van Blaaderen. A new colloidal model system to study long-range interactions quantitatively in real space. *J. Phys.: Condens. Matter*, 15:S3581, 2003.

[37] M. E. Leunissen, C. G. Christova, A-P. Hynninen, C. P. Royall, A. I. Campbell, A. Imhof, M. Dijkstra, R. van Roij, and A. van Blaaderen. Ionic colloidal crystals of oppositely charged particles. *Nature*, 437:235, 2005.

[38] A. Yethiraj and A. Van Blaaderen. A colloidal model system with an interaction tunable from hard sphere to soft and dipolar. *Nature*, 421:513, 2003.

[39] A. V. Straube and P. Tierno. Tunable interactions between paramagnetic colloidal particles driven in a modulated ratchet potential. *Soft Matter*, 10:3915, 2014.

[40] R. D. L. Hanes, C. Dalle-Ferrier, M. Schmiedeberg, M. C. Jenkins, and S. U. Egelhaaf. Colloids in one dimensional random energy landscapes. *Soft Matter*, 8:2714, 2012.

[41] M. P. N. Juniper, R. Besseling, D. G. A. L. Aarts, and R. P. A. Dullens. Acousto-optically generated potential energy landscapes: Potential mapping using colloids under flow. *Opt. Express*, 20:46, 2012.

[42] A. Snezhko and I. S. Aranson. Magnetic manipulation of self-assembled colloidal asters. *Nat. Mater.*, 10:698, 2011.

[43] L. Assoud, F. Ebert, P. Keim, R. Messina, G. Maret, and H. Löwen. Ultrafast quenching of binary colloidal suspensions in an external magnetic field. *Phys. Rev. Lett.*, 102:1, 2009.

[44] Y. Wu and D. Derks. Melting and crystallization of colloidal hard-sphere suspensions under shear. *Proc. Natl. Acad. Sci. U.S.A.*, 106:10564, 2009.

[45] D. Semwogerere and E. R. Weeks. Shear-induced particle migration in binary colloidal suspensions. *Phys. Fluids*, 20:043306, 2008.

[46] S. Sacanna, M. Korpics, K. Rodriguez, L. Colón-Meléndez, S-H. Kim, D. J. Pine, and G-R. Yi. Shaping colloids for self-assembly. *Nat. Commun.*, 4:1688, 2013.

[47] A. Bricard, J.-B. Caussin, N. Desreumaux, O. Dauchot, and D. Bartolo. Emergence of macroscopic directed motion in populations of motile colloids. *Nature*, 503:95, 2013.

[48] I. Theurkauff, C. Cottin-Bizonne, J. Palacci, C. Ybert, and L. Bocquet. Dynamic clustering in active colloidal suspensions with chemical signaling. *Phys. Rev. Lett.*, 108:268303, 2012.

[49] A. Imhof and J. K. G. Dhont. Phase behaviour and long-time self-diffusion in a binary hard sphere dispersion. *Colloids Surf., A*, 122:53, 1997.

[50] U. Gasser, E. R. Weeks, A. Schofield, P. N. Pusey, and D. A. Weitz. Real-space imaging of nucleation and growth in colloidal crystallization. *Science*, 292:258, 2001.

[51] E. R. Weeks. Three-dimensional direct imaging of structural relaxation near the colloidal glass transition. *Science*, 287:627, 2000.

[52] A. H. Marcus, J. Schofield, and S. A. Rice. Experimental observations of non-Gaussian behavior and stringlike cooperative dynamics in concentrated quasi-two-dimensional colloidal liquids. *Phys. Rev. E.*, 60:5725, 1999.

[53] B. Cui, B. Lin, and S. A. Rice. Dynamical heterogeneity in a dense quasi-two-dimensional colloidal liquid. *J. Chem. Phys.*, 114:9142, 2001.

[54] B. Cui, H. Diamant, B. Lin, and S. A. Rice. Anomalous hydrodynamic interaction in a quasi-two-dimensional suspension. *Phys. Rev. Lett.*, 92:258301, 2004.

[55] J. Santana-Solano and J. Arauz-Lara. Short-time dynamics of colloidal particles confined between two walls. *Phys. Rev. E*, 65:021406, 2002.

[56] M. Carbajal-Tinoco, G. Cruz de León, and J. Arauz-Lara. Brownian motion in quasibidimensional colloidal suspensions. *Phys. Rev. E*, 56(6):6962–6969, 1997.

[57] A. Ramírez-Saito, J. Santana-Solano, B. Bonilla-Capilla, and J. L. Arauz-Lara. Hydrodynamic interactions in quasi-two-dimensional colloidal suspensions. *J. Nonnewton. Fluid Mech.*, 165:941, 2010.

[58] M. Brunner and C. Bechinger. Measuring the equation of state of a hard-disc fluid. *Europhys. Lett.*, 63(6):791, 2003.

[59] T. O. E. Skinner, D. G. A. L. Aarts, and R. P. A. Dullens. Grain-boundary fluctuations in two-dimensional colloidal crystals. *Phys. Rev. Lett.*, 105:168301, 2010.

[60] T. O. E. Skinner, S. K. Schnyder, D. G. A. L. Aarts, J. Horbach, and R. P. A. Dullens. Localization dynamics of fluids in random confinement. *Phys. Rev. Lett.*, 111:128301, 2013.

[61] A. L. Thorneywork, R. Roth, D. G. A. L. Aarts, and R. P. A. Dullens. Communication: Radial distribution functions in a two-dimensional binary colloidal hard sphere system. *J. Chem. Phys.*, 140:161106, 2014.

[62] W. Chen and P. Tong. Short-time self-diffusion of weakly charged silica spheres at aqueous interfaces. *Europhys. Lett.*, 84:28003, 2008.

[63] Y. Peng, W. Chen, T. M. Fischer, D. A. Weitz, and P. Tong. Short-time self-diffusion of nearly hard spheres at an oilwater interface. *J. Fluid Mech.*, 618:243, 2008.

[64] K. Zahn, R. Lenke, and G. Maret. Two-stage melting of paramagnetic colloidal crystals in two dimensions. *Phys. Rev. Lett.*, 82:2721, 1999.

[65] K. Zahn, J. Méndez-Alcaraz, and G. Maret. Hydrodynamic interactions may enhance the self-diffusion of colloidal particles. *Phys. Rev. Lett.*, 79(1):175, July 1997.

[66] X. Ma, W. Chen, Z. Wang, Y. Peng, Y. Han, and P. Tong. Test of the universal scaling law of diffusion in colloidal monolayers. *Phys. Rev. Lett.*, 110:078302, 2013.

[67] H. König, R. Hund, K. Zahn, and G. Maret. Experimental realization of a model glass former in 2D. *Eur. Phys. J. E*, 18:287, 2005.

[68] P. P. Lele, J. W. Swan, J. F. Brady, N. J. Wagner, and E. M. Furst. Colloidal diffusion and hydrodynamic screening near boundaries. *Soft Matter*, 7:6844, 2011.

[69] P. Holmqvist, J. Dhont, and P. Lang. Anisotropy of Brownian motion caused only by hydrodynamic interaction with a wall. *Phys. Rev. E*, 74:021402, 2006.

[70] D. Frenkel. Entropy-driven phase transitions. *Physica A*, 263:26, 1999.

[71] L. Onsager. The effects of shape on the interaction of colloidal particles. *Proc. NY. Acad. Sci*, 51:627, 1949.

[72] W. W. Wood and J. D. Jacobson. Preliminary results from a recalculation of the Monte Carlo equation of state of hard spheres. *J. Chem. Phys.*, 27(5):1207, 1957.

[73] B. J. Alder and T. E. Wainwright. Phase transition for a hard sphere system. *J. Chem. Phys.*, 27:1208, 1957.

[74] W. G. Hoover and F. H. Ree. Melting transition and communal entropy for hard spheres. *J. Chem. Phys.*, 49:3609, 1968.

[75] J. D. Weeks, D. Chandler, and H. C. Andersen. Perturbation theory of the thermodynamic properties of simple liquids. *J. Chem. Phys.*, 55:5422, 1971.

[76] B. J. Alder and T. E. Wainwright. Velocity autocorrelations for hard spheres. *Phys. Rev. Lett.*, 18:988, 1967.

[77] A. Donev, F. H. Stillinger, and S. Torquato. Do binary hard disks exhibit an ideal glass transition? *Phys. Rev. Lett.*, 96:225502, 2006.

[78] R. Roth, K. Mecke, and M. Oettel. Communication: Fundamental measure theory for hard disks: fluid and solid. *J. Chem. Phys.*, 136(8):081101, 2012.

[79] B. Cichocki and K. Hinsen. Dynamic computer simulation of concentrated hard sphere suspensions. *Physica A*, 166:473, 1990.

[80] J. F Brady. Model hard-sphere dispersions: statistical mechanical theory, simulations, and experiments. *Curr. Opin. Colloid Interface Sci.*, 1(4):472, 1996.

[81] S. Sastry, T. M. Truskett, P. G. Debenedetti, S. Torquato, and F. H. Stillinger. Free volume in the hard sphere liquid. *Mol. Phys.*, 95:289, 1998.

[82] D. M. Gass. Enskog theory for a rigid disk fluid. *J. Chem. Phys.*, 54:1898, 1971.

[83] W.-S. Xu, Z.-Y. Sun, and L.-J. An. Structure, compressibility factor, and dynamics of highly size-asymmetric binary hard-disk liquids. *J. Chem. Phys.*, 137:104509, 2012.

[84] A. Van Blaaderen, J. Peetermans, G. Maret, and J. K. G. Dhont. Long-time self-diffusion of spherical colloidal particles measured with fluorescence recovery after photobleaching. *J. Chem. Phys.*, 96(6):4591, 1992.

[85] W. Van Megen and S. M. Underwood. Glass transition in colloidal hard spheres: Measurement and mode-coupling-theory analysis of the coherent intermediate scattering function. *Phys. Rev. E*, 49:4206, 1994.

[86] P. N. Pusey, E. Zaccarelli, C. Valeriani, E. Sanz, W. C. K. Poon, and M. E. Cates. Hard spheres: crystallization and glass formation. *Phil. Trans. R. Soc. A*, 367:4993, 2009.

[87] J.L. Barrat, W. Gotze, and A. Latz. The liquid-glass transition of the hard-sphere system. *J. Phys. Condens. Matter*, 1:7163, 1989.

[88] W. Qi, A. P. Gantapara, and M. Dijkstra. Two-stage melting induced by dislocations and grain boundaries in monolayers of hard spheres. *Soft Matter*, 10:5449, 2014.

[89] E. P. Bernard and W. Krauth. Two-step melting in two dimensions: first-order liquid-hexatic transition. *Phys. Rev. Lett.*, 107(15):155704, 2011.

[90] B. Widom. Intermolecular forces and the nature of the liquid. *Science*, 157:375, 1967.

[91] H. C. Longuet-Higgins and B. Widom. A rigid sphere model for the melting of argon. *Mol. Phys.*, 8:549, 1964.

[92] J. D. Weeks, D. Chandler, and H. C. Andersen. Role of repulsive forces in determining the equilibrium structure of simple liquids. *J. Chem. Phys.*, 54:5237, 1971.

[93] S. Amore, J. Horbach, and I. Egry. Is there a relation between excess volume and miscibility in binary liquid mixtures? *J. Chem. Phys.*, 134:044515, 2011.

[94] J. D. Bernal and J. Mason. Packing of spheres: co-ordination of randomly packed spheres. *Nature*, 188:910, 1960.

[95] G. D'anna, P. Mayor, A. Barrat, V. Loreto, and F. Nori. Observing Brownian motion in vibration-fluidized granular matter. *Nature*, 424:909, 2003.

[96] P. Richard, M. Nicodemi, R. Delannay, P. Ribière, and D. Bideau. Slow relaxation and compaction of granular systems. *Nat. mater.*, 4:121, 2005.

[97] E. J. Banigan, M. K. Illich, D. J. Stace-Naughton, and D. A. Egolf. The chaotic dynamics of jamming. *Nat. Phys.*, 9:288, 2013.

[98] C. P. Royall, W. C. K. Poon, and E. R. Weeks. In search of colloidal hard spheres. *Soft Matter*, 9:17, 2013.

[99] J. P. Hansen and I. R. Macdonald. *Theory of Simple Liquids*. Academic Press, 3rd edition edition, 2006.

[100] D. A. Mcquarrie. *Statistical Mechanics*. University Science Books, 1st edition edition, 2000.

[101] M. J. van der Huijben and W. Lugt. X-ray and neutron diffraction from liquid alkali metals. *Acta Cryst. A*, 35:431, 1979.

[102] T. Bodensteiner, C. Morkel, W. Glaser, and B. Dorner. Collective dynamics in liquid cesium near the melting point. *Phys. Rev. A*, 45, 1992.

[103] W. Van Megen and I. Snook. Equilibrium properties of suspensions. *Adv. Colloid Interface Sci.*, 21:119, 1984.

[104] C. G. De Kruif, W. J. Briels, R. P. May, and A. Vrij. Hard-sphere colloidal silica dispersions. The structure factor determined with SANS. *Langmuir*, 4:668, 1988.

[105] I. S. Khattab, F. Bandarkar, M. A. A. Fakhree, and A. Jouyban. Density, viscosity, and surface tension of water+ethanol mixtures from 293 to 323K. *Korean J. Chem. Eng.*, 29:812, 2012.

[106] J. C. Crocker and D. G. Grier. Methods of digital video microscopy for colloidal studies. *J. Colloid Interface Sci.*, 179:298, 1996.

[107] T. Kawasaki and H. Tanaka. Structural signature of slow dynamics and dynamic heterogeneity in two-dimensional colloidal liquids: glassy structural order. *J. Phys. Condens. Matter*, 23:194121, 2011.

[108] S. P. Das. Mode-coupling theory and the glass transition in supercooled liquids. *Rev. Mod. Phys.*, 76:785, 2004.

[109] J. L. Lebowitz. Exact solution of generalized Percus-Yevick equation for a mixture of hard spheres. *Phys. Rev.*, 116:A895, 1964.

[110] M. S. Wertheim. Exact solution of the Percus-Yevick integral equation for hard spheres. *Phys. Rev. Lett.*, 10:321, 1963.

[111] F. Lado. Equation of state of the hard-disk fluid from approximate integral equations. *J. Chem. Phys.*, 49:3092, 1968.

[112] Y. Uehara, T. Ree, and F. H. Ree. Radial distribution function for hard disks from the BGY2 theory). *J. Chem. Phys.*, 70:1876, 1979.

[113] L. Verlet and D. Levesque. Integral equations for classical fluids. *Mol. Phys.*, 46:969, 1982.

[114] D. G. Chae, F. H. Ree, and T. Ree. Radial distribution functions and equation of state of the hard-disk fluid. *J. Chem. Phys.*, 50(4):1581, 1969.

[115] W. W. Wood. NpT-ensemble Monte Carlo calculations for the hard-disk fluid. *J. Chem. Phys.*, 52:729, 1970.

[116] J. G. Kirkwood, E. K. Maun, and B. J. Alder. Radial distribution functions and the equation of state of a fluid composed of rigid spherical molecules. *J. Chem. Phys.*, 18:1040, 1950.

[117] A. Van Blaaderen and P. Wiltzius. Real-space structure of colloidal hard-sphere glasses. *Science*, 270:1177, 1995.

[118] R. P. A. Dullens, D. G. A. L. Aarts, and W. K. Kegel. Direct measurement of the free energy by optical microscopy. *Proc. Natl. Acad. Sci. U.S.A.*, 103:529, 2006.

[119] C. P. Royall, A. A. Louis, and H. Tanaka. Measuring colloidal interactions with confocal microscopy. *J. Chem. Phys.*, 127:044507, 2007.

[120] C. A. Murray and D. H. Van Winkle. Experimental observation of two-stage melting in a classical two-dimensional screened Coulomb system. *Phys. Rev. Lett.*, 58:1200, 1987.

[121] V. Michailidou, G. Petekidis, J. Swan, and J. Brady. Dynamics of Concentrated Hard-Sphere Colloids Near a Wall. *Phys. Rev. Lett.*, 102:068302, 2009.

[122] M. Brunner, C. Bechinger, W. Strepp, V. Lobaskin, and H. H. von Grunberg. Density-dependent pair interactions in 2D colloidal suspensions. *Europhys. Lett.*, 58(6):926, 2002.

[123] S. Behrens and D. Grier. Pair interaction of charged colloidal spheres near a charged wall. *Phys. Rev. E*, 64(5):050401(R), 2001.

[124] M. Quesada-Perez, A. Moncho-Jorda, F. Martnez-Lopez, and R. Hidalgo-Alvarez. Probing interaction forces in colloidal monolayers: Inversion of structural data. *J. Chem. Phys.*, 115:10897, 2001.

[125] G. M. Kepler and S. Fraden. Attractive potential between confined colloids at low ionic strength. *Phys. Rev. Lett.*, 73:356, 1994.

[126] A. H. Marcus and S. A. Rice. Observations of first-order liquid-to-hexatic and hexatic-to-solid phase transitions in a confined colloid suspension. *Phys. Rev. Lett.*, 77:2577, 1996.

[127] B. Cui, B. Lin, and S. A. Rice. Structure and phase transitions in confined binary colloid mixtures. *J. Chem. Phys.*, 119:2386, 2003.

[128] A. S. Keys, L. O. Hedges, J. P. Garrahan, S. C. Glotzer, and D. Chandler. Excitations are localized and relaxation is hierarchical in glass-forming liquids. *Phys. Rev. X*, 1:021013, 2011.

[129] R. Kurita and E. R. Weeks. Glass transition of two-dimensional binary soft-disk mixtures with large size ratios. *Phys. Rev. E*, 82:041402, 2010.

[130] S. Gokhale, K. H. Nagamanasa, R. Ganapathy, and A. K. Sood. Growing dynamical facilitation on approaching the random pinning colloidal glass transition. *Nat. Commun.*, 5:1, 2014.

[131] M. Rovere, D. Heermann, and K. Binder. The gas-liquid transition of the two-dimensional Lennard-Jones fluid. *J. Phys. Condens. Matter*, 2:7009, 1990.

[132] M. Rovere, D. W. Hermann, and K. Binder. Block density distribution function analysis of two-dimensional Lennard-Jones fluids. *Europhys. Lett.*, 6:585, 1988.

[133] A. B. Bhatia and D. E. Thornton. Structural aspects of the electrical resistivity of binary alloys. *Phys. Rev. B*, 2:3004, 1970.

[134] T. M. Truskett, S. Torquato, S. Sastry, P. G. Debenedetti, and F. H. Stillinger. Structural precursor to freezing in the hard-disk and hard-sphere systems. *Phys. Rev. E*, 58:3083, 1998.

[135] Y. Rosenfeld. Free-energy model for the inhomogeneous hard-sphere fluid mixture and density-functional theory of freezing. *Phys. Rev. Lett.*, 63:980, 1989.

[136] R. Roth. Fundamental measure theory for hard-sphere mixtures: a review. *J. Phys. Condens. matter*, 22:063102, 2010.

[137] R. Evans. The nature of the liquid-vapour interface and other topics in the statistical mechanics of non-uniform, classical fluids. *Adv. Phys.*, 28:143, 1979.

[138] D Frenkel and B Smit. *Understanding Molecular Simulation.* Academic Press, San Diego, 2002.

[139] Stefan Luding and Oliver Strauß. *Granular Gases*. Springer, 2001.

[140] M. Barošová, M. Malijevský, S. Labik, and W.R. Smith. Computer simulation of the chemical potentials of binary hard-sphere mixtures. *Mol. Phys.*, 87:423, 1996.

[141] M. Gonzalez-Melchor, J. Alejandre, and M. Loppez de Haro. Equation of state and structure of binary mixtures of hard d-dimensional hyperspheres. *J. Chem. Phys.*, 114:4905, 2001.

[142] D. Cao, K. Y. Chan, D. Henderson, and W. Wang. Monte Carlo data of dilute solutions of large spheres in binary hard sphere mixtures. *Mol. Phys.*, 98(9):619, 2000.

[143] J. Tobochnik and P. M. Chapin. Monte Carlo simulation of hard spheres near random closest packing using spherical boundary conditions. *J. Chem. Phys.*, 88:5824, 1988.

[144] E. Helfand, H. L. Frisch, and J. L. Lebowitz. Theory of the two- and one-dimensional rigid sphere fluids. *J. Chem. Phys.*, 34:1037, 1961.

[145] C. Grodon, M. Dijkstra, R. Evans, and R. Roth. Decay of correlation functions in hard-sphere mixtures: structural crossover. *J. Chem. Phys.*, 121(16):7869, 2004.

[146] C. Grodon , M. Dijkstra, R. Evans, and R. Roth. Homogeneous and inhomogeneous hard-sphere mixtures: manifestations of structural crossover. *Mol. Phys.*, 103:3009, 2005.

[147] J. Baumgartl, R. P. A. Dullens, M. Dijkstra, R. Roth, and C. Bechinger. Experimental observation of structural crossover in binary mixtures of colloidal hard spheres. *Phys. Rev. Lett.*, 98:198303, 2007.

[148] C. Barrio and J. R. Solana. Contact pair correlation functions and equation of state for additive hard disk fluid mixtures. *J. Chem. Phys.*, 115:7123, 2001.

[149] S. Luding and A. Santos. Molecular dynamics and theory for the contact values of the radial distribution functions of hard-disk fluid mixtures. *J. Chem. Phys.*, 121:8458, 2004.

[150] J. L. Lebowitz, E. Helfand, and E. Praestgaard. Scaled particle theory of fluid mixtures. *J. Chem. Phys.*, 43:774, 1965.

[151] A. Santos, S. B. Yuste, and M. Lopez de Haro. Contact values of the radial distribution functions of additive hard-sphere mixtures in d dimensions: A new proposal. *J. Chem. Phys.*, 117:5785, 2002.

[152] J. Horbach, S. Das, a. Griesche, M. P. Macht, G. Frohberg, and A. Meyer. Self-diffusion and interdiffusion in Al80Ni20 melts: Simulation and experiment. *Phys. Rev. B*, 75:174304, 2007.

[153] G. T. Evans and C. P. James. A calculation of the self-diffusion coefficient for a dilute solution of Brownian particles. *J. Chem. Phys.*, 79:5553, 1983.

[154] J. F. Brady. The long-time self-diffusivity in concentrated colloidal dispersions. *J. Fluid Mech.*, 272:109, 1994.

[155] J. M. Rallison. Brownian diffusion in concentrated suspensions of interacting particles. *J. Fluid Mech.*, page 471, 1988.

[156] A. J. Banchio, G. Nägele, and J. Bergenholtz. Collective diffusion, self-diffusion and freezing criteria of colloidal suspensions. *J. Chem. Phys.*, 113:3381, 2000.

[157] B. Cichocki and B. U. Felderhof. Long-time self-diffusion coefficient and zero-frequency viscosity of dilute suspensions of spherical Brownian particles. *J. Chem. Phys.*, 89:3705, 1988.

[158] G. K. Batchelor. Brownian diffusion of particles with hydrodynamic interaction. *J. Fluid Mech.*, 74:1, 1976.

[159] C. W. J Beenakker and P. Mazur. Diffusion of spheres in a concentrated suspension II. *Physica A*, page 349, 1984.

[160] M. Medina-Noyola. Long-time self-diffusion in concentrated colloidal dispersions. *Phys. Rev. Lett.*, 60(26):2705, 1988.

[161] H. N. W. Lekkerkerker and J. K. G. Dhont. On the calculation of the self-diffusion coefficient of interacting Brownian particles. *J. Chem. Phys.*, 80:5790, 1984.

[162] J. A. Leegwater and G. Szamel. Dynamical properties of hard-sphere suspensions. *Phys. Rev. A*, 46, 1992.

[163] R. O. Sokolovskii, M. Thachuk, and G. N. Patey. Tracer diffusion in hard sphere fluids from molecular to hydrodynamic regimes. *J. Chem. Phys.*, 125:204502, 2006.

[164] R. García-Rojo, S. Luding, and J. Brey. Transport coefficients for dense hard-disk systems. *Phys. Rev. E*, 74:061305, 2006.

[165] K. Binder and W. Kob. *Glassy materials and disordered solids.* World Scientific Pub Co Pte Ltd, 2011.

[166] L. Berthier, G. Biroli, J.-P. Bouchaud, L. Cipelletti, and W. van Sarloos. *Dynamical heterogeneities in glasses, colloids and granular media.* Oxford University Press, 2011.

[167] A. Imhof and J. K. G. Dhont. Long-time self-diffusion in binary colloidal hard-sphere dispersions. *Phys. Rev. E*, 52:6344, 1995.

[168] W. van Megen and S. M. Underwood. Tracer diffusion in concentrated colloidal dispersions. III. Mean squared displacements and self-diffusion coefficients. *J. Chem. Phys.*, 91(1):552, 1989.

[169] R. H. Ottewill and N. S. J. Williams. Study of particle motion in concentrated dispersions by tracer diffusion. *Nature*, 325, 1987.

[170] A. H. Marcus, B. Lin, and S. A. Rice. Self-diffusion in dilute quasi-two-dimensional hard sphere suspensions: Evanescent wave light scattering and video microscopy studies. *Phys. Rev. E*, 53:1765, 1996.

[171] J. K. G. Dhont. *An introduction to dynamics of colloids.* Elsevier, 1996.

[172] Rallison, J. M. and Hinch, E. J. The effect of particle interactions on dynamic light scattering from a dilute suspension. *J. Fluid Mech.*, 167:131, 1986.

[173] W. van Megen, S. M. Underwood, and I. Snook. Tracer diffusion in concentrated colloidal dispersions. *J. Chem. Phys.*, 85(7):4065, 1986.

[174] X. Qiu, X. L. Wu, J. Z. Xue, D.J. Pine, D. A. Weitz, and P. M. Chaikin. Hydrodynamic interactions in concentrated suspensions. *Phys. Rev. Lett.*, 65:516, 1990.

[175] P. Holmqvist and G. Nägele. Long-time dynamics of concentrated charge-stabilized colloids. *Phys. Rev. Lett.*, 104:058301, 2010.

[176] G. D. J. Phillies. Measurement of the (quasi)-self-diffusion coefficient of solutions of Brownian macroparticles. *J. Chem. Phys.*, 81:1487, 1984.

[177] R. Krause, G. Nägele, J. L. Arauz-Lara, and R. Weber. Brownian motion in binary colloidal suspensions. *J. Colloid Interface Sci.*, 148:231, 1992.

[178] P. D. Kaplan, A. G. Yodh, and D. J. Pine. Diffusion and structure in dense binary suspensions. *Phys. Rev. Lett.*, 68:393, 1992.

[179] S. Williams and W. van Megen. Motions in binary mixtures of hard colloidal spheres: Melting of the glass. *Phys. Rev. E*, 64:041502, 2001.

[180] A. J. Moreno and J. Colmenero. Relaxation scenarios in a mixture of large and small spheres: dependence on the size disparity. *J. Chem. Phys.*, 125:164507, 2006.

[181] A. Moreno and J. Colmenero. Anomalous dynamic arrest in a mixture of large and small particles. *Phys. Rev. E*, 74:021409, 2006.

[182] J. Santana-Solano, A. Ramírez-Saito, and J. Arauz-Lara. Short-time dynamics in quasi-two-dimensional colloidal suspensions. *Phys. Rev. Lett.*, 95:198301, 2005.

[183] W. K. Kegel and van Blaaderen A. Direct observation of dynamical heterogeneities in colloidal hard-sphere suspensions. *Science*, 287:290, 2000.

[184] J. Leach, H. Mushfique, S. Keen, R. Di Leonardo, G. Ruocco, J. Cooper, and M. Padgett. Comparison of Faxéns correction for a microsphere translating or rotating near a surface. *Phys. Rev. E*, 79:026301, 2009.

[185] E. Sanz and D. Marenduzzo. Dynamic Monte Carlo versus Brownian dynamics: A comparison for self-diffusion and crystallization in colloidal fluids. *J. Chem. Phys.*, 132:194102, 2010.

[186] G. K. Batchelor. Diffusion in a dilute polydisperse system of interacting spheres. *J. Fluid Mech.*, 131:155, 1982.

[187] M. M. Kops-Werkhoven and H. M. Fijnaut. Dynamic light scattering and sedimentation experiments on silica dispersions at finite concentrations. *J. Chem. Phys.*, 74:1618, 1981.

[188] G. Batôt, V. Dahirel, G. Mériguet, A. A. Louis, and M. Jardat. Dynamics of solutes with hydrodynamic interactions: Comparison between Brownian dynamics and stochastic rotation dynamics simulations. *Phys. Rev. E*, 88:043304, 2013.

[189] A. Tomilov, A. Videcoq, T. Chartier, T. Ala-Nissilä, and I. Vattulainen. Tracer diffusion in colloidal suspensions under dilute and crowded conditions with hydrodynamic interactions. *J. Chem. Phys.*, 137:014503, 2012.

[190] B. J. Ackerson. Correlations for dilute hard core suspensions. *J. Chem. Phys.*, 76:2675, 1982.

[191] J. Schofield, A. H. Marcus, and Stuart A. Rice. Dynamics of quasi two-dimensional colloidal systems. *J. Chem. Phys.*, 3654:18950, 1996.

[192] W. Götze and T. Voigtmann. Effect of composition changes on the structural relaxation of a binary mixture. *Phys. Rev. E*, 67:021502, 2003.

[193] W. van Megen, T. Mortensen, S. Williams, and J. Müller. Measurement of the self-intermediate scattering function of suspensions of hard spherical particles near the glass transition. *Phys. Rev. E*, 58:6073, 1998.

[194] W. van Megen, T. Mortensen, and G. Bryant. Change in relaxation scenario at the order-disorder transition of a colloidal fluid of hard spheres seen from the Gaussian limit of the self-intermediate scattering function. *Phys. Rev. E*, 72:031402, 2005.

[195] J. W. Swan and J. F. Brady. Anisotropic diffusion in confined colloidal dispersions: the evanescent diffusivity. *J. Chem. Phys.*, 135:014701, 2011.

[196] J. C. Brown, P. N. Pusey, J. W. Goodwin, and R. H. Ottewill. Light scattering study of dynamic and time-averaged correlations in dispersions of charged particles. *J. Phys. A*, 8(5):664, 1975.

[197] C. A. Murray and D. G. Grier. Video microscopy of monodisperse colloidal systems. *Annu. Rev. Phys. Chem.*, 47:421, 1996.

[198] V. Prasad, D. Semwogerere, and E. R. Weeks. Confocal microscopy of colloids. *J. Phys. Condens. Matter*, 19:113102, 2007.

[199] B. R. A. Nijboer and A. Rahman. Time expansion of correlation functions and the theory of slow neutron scattering. *Physica*, 32:415, 1966.

[200] A. Rahman. Correlations in the motion of atoms in liquid argon. *Phys.Rev.*, 136:A 405, 1964.

[201] T. Vicsek and A. A Zafeiris. Collective motion. *Phys. Rep.*, 517:71–140, 2012.

[202] H. P. Zhang, A. Be'er, E.-L. Florin, and H. L. Swinney. Collective motion and density fluctuations in bacterial colonies. *Proc. Natl. Acad. Sci. U. S. A.*, 107:13626, 2010.

[203] W. Bialek and A. A Cavagna. Statistical mechanics for natural flocks of birds. *Proc. Natl. Acad. Sci. U.S.A.*, 109:4786, 2012.

[204] I. Aranson and L. Tsimring. Patterns and collective behavior in granular media: Theoretical concepts. *Rev. Mod. Phys.*, 78:641, 2006.

[205] G. Adam and J. H. Gibbs. On the temperature dependence of cooperative relaxation properties in glass-forming liquids. *J. Chem. Phys.*, 43:139, 1965.

[206] E. Falck, J. M. Lahtinen, I. Vattulainen, and T. Ala-Nissila. Influence of hydrodynamics on many-particle diffusion in 2D colloidal suspensions. *Eur. Phys. J. E Soft Matter*, 13:267, 2004.

[207] A. Griesche, M.-P. Macht, and G. Frohberg. First results from diffusion measurements in liquid multicomponent Al-based alloys. *J. Non-Cryst. Solids*, 353:3305, 2007.

[208] F. Kargl, E. Sondermann, H Weis, and A. Meyer. Impact of convective flow on long-capillary chemical diffusion studies of liquid binary alloys. *High Temp. High Press.*, 42:3, 2013.

[209] P. Kuhn, J. Horbach, F. Kargl, A. Meyer, and T. Voigtmann. Diffusion and interdiffusion in binary metallic melts. *Phys. Rev.B*, 90:024309, 2014.

[210] S. K. Das, J. Horbach, K. Binder, M. E. Fisher, and J. V. Sengers. Static and dynamic critical behavior of a symmetrical binary fluid: a computer simulation. *J. Chem. Phys.*, 125:24506, 2006.

[211] L. S. Darken. Diffusion, mobility and their interrelation through free energy in binary metallic systems. *Trans. AIME*, 171:130, 1947.

[212] T. Voigtmann, A. Meyer, D. Holland-Moritz, S. Stüber, T. Hansen, and T. Unruh. Atomic diffusion mechanisms in a binary metallic melt. *Europhys. Lett.*, 82:66001, 2008.

[213] J. Zausch, P. Virnau, K. Binder, J. Horbach, and R. L. Vink. Statics and dynamics of colloid-polymer mixtures near their critical point of phase separation: A computer simulation study of a continuous Asakura-Oosawa model. *J. Chem. Phys.*, 130(6):064906, 2009.

[214] Q. H. Wei, C. Bechinger, and P. Leiderer. Single-file diffusion of colloids in one-dimensional channels. *Science*, 287:625, 2000.

[215] R. Di Leonardo, S. Keen, F. Ianni, J. Leach, M. Padgett, and G. Ruocco. Hydrodynamic interactions in two dimensions. *Phys. Rev. E*, 78:031406, 2008.

[216] Z. Kutnjak and C.W. Garland. Generalized smectic-hexatic phase diagram. *Phys. Rev. E*, 57:3015, 1998.

[217] A. V. Petukhov, D. van der Beek, R. P. A. Dullens, I. P. Dolbnya, G. J. Vroege, and H. N. W. Lekkerkerker. Observation of a hexatic columnar liquid crystal of polydisperse colloidal disks. *Phys. Rev. Lett.*, 95:077801, 2005.

[218] K. Binder, S. Sengupta, and P. Nielaba. The liquid-solid transition of hard discs: first-order transition or Kosterlitz-Thouless-Halperin-Nelson-Young scenario? *J. Phys.: Condens. Matter*, 2323, 2002.

[219] S. C. Kapfer and W. Krauth. Two-dimensional melting: From liquid-hexatic coexistence to continuous transitions. *Phys. Rev. Lett.*, 114:035702, 2015.

[220] P. Bladon and D. Frenkel. Dislocation unbinding in dense two-dimensional crystals. *Phys. Rev. Lett.*, 74:2519, 1995.

[221] W. Qi and M. Dijkstra. Destabilisation of the hexatic phase in systems of hard disks by quenched disorder due to pinning on a lattice. *Soft Matter*, 11:2852, 2015.

[222] S. Deutschländer, T. Horn, H. Löwen, G. Maret, and P. Keim. Two-dimensional melting under quenched disorder. *Phys. Rev. Lett.*, 111:098301, 2013.

[223] M. A. Bates and D. Frenkel. Influence of vacancies on the melting transition of hard disks in two dimensions. *Phys.Rev. E*, 61:5223, 2000.

[224] K. Zahn and G. Maret. Dynamic criteria for melting in two dimensions. *Phys. Rev. Lett.*, 85:3656, 2000.

[225] P. Keim, G. Maret, and H. H. von Grünberg. Franks constant in the hexatic phase. *Phys. Rev. E*, 75:031402, 2007.

[226] Y. Han, N. Y. Ha, A. M. Alsayed, and A. G. Yodh. Melting of two-dimensional tunable-diameter colloidal crystals. *Phys. Rev. E*, 77:041406, 2008.

[227] Y. Peng, Z. Wang, A. M. Alsayed, A. G. Yodh, and Y. Han. Melting of colloidal crystal films. *Phys. Rev. Lett.*, 104:205703, 2010.

[228] P. Karnchanaphanurach, B. Lin, and S. A. Rice. Melting transition in a quasi-two-dimensional colloid suspension: Influence of the colloid-colloid interaction. *Phys. Rev. E.*, 61:4036, 2000.

[229] B. J. Alder and T. E. Wainwright. Phase transition in elastic disks. *Phys. Rev.*, 127:359, 1962.

[230] A. Jaster. Computer simulations of the two-dimensional melting transition using hard disks. *Phys. Rev. E.*, 59:2594, 1999.

[231] J. Lee and K. J. Strandburg. First-order melting transition of the hard-disk system. *Phys.Rev. B*, 46:190, 1992.

[232] J. A. Zollweg and G. V. Chester. Melting in two dimensions. *Phys. Rev. B*, 46:11186, 1992.

[233] J. F. Fernández, J. J. Alonso, and J. Stankiewicz. One-stage continuous melting transition in two dimensions. *Phys. Rev. Lett.*, 75, 1995.

[234] M. Engel, J. A. Anderson, S. C. Glotzer, M. Isobe, E. P. Bernard, and W. Krauth. Hard-disk equation of state: First-order liquid-hexatic transition in two dimensions with three simulation methods. *Phys. Rev. E*, 87:042134, 2013.

[235] D. R. Nelson. *Defects and geometry in condensed matter physics.* Cambridge University Press, 2002.

[236] U. Gasser, C. Eisenmann, G. Maret, and P. Keim. Melting of crystals in two dimensions. *Chemphyschem*, 11:963, 2010.

[237] V. M. Bedanov, G. V. Gadiyak, and Y. E. Lozovik. On a modified Lindemann-like criterion for 2D melting. *Phys. Lett. A*, 109A:289, 1985.

[238] M. A. Rutgers, J. H. Dunsmuir, J.Z. Xue, W. B. Russel, and P. M. Chaikin. Measurement of the hard-sphere equation of state using screened charged polystyrene colloids. *Phys. Rev. B*, 53:5043, 1996.

[239] D. Bedeaux and J. D. Weeks. Correlation functions in the capillary wave model of the liquidvapor interface. *J. Chem. Phys.*, 82:972, 1985.

[240] M. P. A. Fisher, D. S. Fisher, and J. D. Weeks. Agreement of capillary-wave theory with exact results for the interface profile of the two-dimensional Ising model. *Phys. Rev. Lett.*, 48(5):1982, 1982.

[241] A. A. Verhoeff, F. Lavergne, D. Bartolo, D. G. A. L. Aarts, and R. P. A. Dullens. Optical trapping of interfaces at ultra-low interfacial tension. *Soft Matter*, 11, 2015.

[242] Z. T. Trautt and M. Upmanyu. Direct two-dimensional calculations of grain boundary stiffness. *Scr. Mater.*, 52:1175, 2005.

[243] D. G. A. L. Aarts, M. Schmidt, and H. N. W. Lekkerkerker. Direct visual observation of thermal capillary waves. *Science*, 304:847, 2004.

[244] Van D. Nguyen, Z. Hu, and P. Schall. Single crystal growth and anisotropic crystal-fluid interfacial free energy in soft colloidal systems. *Phys. Rev. E*, 84:011607, 2011.

[245] J. J. Hoyt, Z. T. Trautt, and M. Upmanyu. Fluctuations in molecular dynamics simulations. *Math. Comput. Simul.*, 80:1382, 2010.

[246] W. C. K Poon, E. R. Weeks, and C. P. Royall. On measuring colloidal volume fractions. *Soft Matter*, 8:21, 2012.

List of publications

To date the following publications based upon work in this thesis have been submitted or are in preparation:

Alice L. Thorneywork, Roland Roth, Dirk G. A. L. Aarts, Roland Roth and Roel P. A. Dullens, *Radial distribution functions in a two-dimensional binary colloidal hard sphere system*, J. Chem. Phys. 140, 161106, (2014), (Chapter 3)

Alice L. Thorneywork, Dirk G. A. L. Aarts, Jürgen Horbach and Roel P. A. Dullens, *Fluctuations in quasi-two-dimensional hard sphere fluids*, In preparation, (Chapter 3)

Alice L. Thorneywork, Roberto E. Rozas, Jürgen Horbach and Roel P. A. Dullens, *Hydrodynamic interactions and long-time self-diffusion in quasi-two-dimensional colloidal hard sphere fluids*, submitted, (Chapter 4)

Alice L. Thorneywork, Dirk G. A. L. Aarts, Jürgen Horbach and Roel P. A. Dullens, *Self-diffusion in quasi-two-dimensional binary colloidal hard sphere fluids*, In preparation, (Chapter 4)

Alice L. Thorneywork, Dirk G. A. L. Aarts, Jürgen Horbach and Roel P. A. Dullens, *The Self-Intermediate scattering function and the Gaussian approximation in a model hard disk system*, In preparation, (Chapter 5)

Alice L. Thorneywork, Dirk G. A. L. Aarts, Jürgen Horbach and Roel P. A. Dullens, *Interdiffusion in quasi-two-dimensional binary colloidal fluids*, In preparation, (Chapter 6)

Alice L. Thorneywork, Joshua L. Abbott, Dirk G. A. L. Aarts and Roel P. A. Dullens, *Melting of quasi-two-dimensional colloidal hard spheres*, In preparation, (Chapter 7)

Acknowledgements

First of all I would like to say thank you to Roel for being a fantastic DPhil supervisor. Your wisdom-about and enthusiasm-for all things colloidal has made the last 3.5 years both very rewarding and a lot of fun. Perhaps more importantly, however, your encouragement, belief in my 'straightforward' work and ability to deal with an Alice panic has kept me going when things haven't been working. On a side note, you have also taught me to be a little more 'Dutch', which I believe to be a very useful transferable life skill.

I would also like to thank Dirk for pointing me in the right direction right at the very start, Roland Roth for the DFT that helped us see hard disks, Jürgen Horbach for his help understanding them (and [99]) and Simon Schnyder for entertaining us during our trips to Düsseldorf.

Members of the Aarts/Dullens group have made the last few years extremely enjoyable but particular mentions go to Sam for sharing important cake-baking duties, to Josh for writing an excellent Part II thesis, to Lia for patiently listening to (and answering) my many, many questions, and to Julia, Raam, Madeleine and Tom for sharing 13-07 with me. Special thanks go to Mike, my experimentally-exceptional, KitKat eating, editor and accomplice. We *have* made Science Work (at least a little bit) and I hope we shall continue to do so for many more years.

Finally, outside the PTCL thanks go to: Emma, for being there to remind me that there is more to life than chemistry, and that when there isn't, chemists don't have to be dull; Melvyn, for all his good advice on filling 'the rucksack'; and to Kerrith, for all of the dinners spent listening to talk of radial distribution functions and for making me smile when they haven't been behaving. Last of all, I would like to thank Marmee and 'Vati' for the first copy of 'Alice' and for supporting me so completely in all of my endeavours since the shoelaces.